Development of a flexible Doppler reflectometry system and its application to turbulence characterization in the ASDEX Upgrade tokamak

Der Fakultät für Physik
der Ludwig-Maximilians-Universität München
zur Erlangung des akademischen Grades eines
Doktors der Naturwissenschaften (Dr. rer. nat.)
vorgelegte Dissertation

von

Carolin Helma Tröster

aus Weiden i. d. Oberpfalz

München, April 2008

Erstgutachter: Prof. Dr. Hartmut Zohm

Zweitgutachter: Prof. Dr. Harald Lesch

Tag der mündlichen Prüfung: 05.08.2008

Zusammenfassung

Eine wesentliche Aufgabe aktueller Fusionsforschung ist die Untersuchung der in magnetisch eingeschlossenen Plasmen auftretenden Turbulenzen. Am ASDEX Upgrade Tokamak wird das Verhalten der Plasmaturbulenz mittels Doppler-Reflektometrie experimentell untersucht. Diese Messmethode basiert auf der räumlich begrenzten, von Dichtefluktuationen verursachten Bragg-Rückstreuung eines ausgesendeten Mikrowellenstrahls mit Wellenzahl k_0 an einer sogenannten Plasma-"Cutoff"- Schicht. Die Diagnostik reagiert dabei auf Fluktuationen mit einer bestimmten Wellenzahl $k_\perp$, welche durch den Einfallswinkel θ über die Bragg-Bedingung $k_\perp \approx 2k_0 sin\theta$ bestimmt wird. Anhand des gemessenen dopperverschobenen Frequenzspektrums kann die senkrechte Rotationsgeschwindigkeit der Dichtefluktuationen, $u_\perp = v_{E\times B} + v_{turb}$, direkt aus der Frequenzverschiebung ($f_D = u_\perp k_\perp / 2\pi$), und die Turbulenzamplitude aus der Höhe der rückgestreuten Leistung bestimmt werden. In dieser Doktorarbeit werden Messungen radialer $u_\perp$-Profile und ortsaufgelöster $k_\perp$-Spektren vorgestellt, welche unter verschiedenen Plasmabedingungen und durch Variation des Einstrahlwinkels durchgefuhrt wurden. Ermöglicht wurden diese Messungen erst durch die Erweiterung des bestehenden Doppler-Reflektometriesystems (V-Band, $50 - 75\,\mathrm{GHz}$) durch ein neues W-Band-System ($75 - 110\,\mathrm{GHz}$), welches speziell zur Messung des $k_\perp$-Spektrums entwickelt wurde und zudem den radialen Messbereich zum Plasmazentrum hin erweitert. Es besteht aus einer steuerbaren Antenne, deren verstellbare Sichtlinie es ermöglicht, Wellenzahlen bis zu $25\,\mathrm{cm}^{-1}$ dynamisch auszuwählen, und einem Reflektometer, dessen phasenstarr stabilisierter Sender die präzise Bestimmung des Ansprechverhaltens erlaubt. Laborüberprüfungen und Vergleichstests mit dem V-Band-System demonstrieren die einwandfreie Funktion der neuen Diagnostik. Die Rotationsgeschwindigkeitsmessungen zeigen eine Wellenzahlabhangigkeit von $u_\perp$. Die Ergebnisse deuten darauf hin, dass die Form des $k_\perp$-Spektrums der vorherrschenden Turbulenz ein wichtiger Faktor bei der Messung von $u_\perp$ ist. Zudem lassen die Daten vermuten, dass der Beitrag der intrinsischen Turbulenzphasengeschwindigkeit v_{turb} zur gemessenen Geschwindigkeit $u_\perp$ in manchen Fällen nicht vernachlässigbar ist. Die erhaltenen Wellenzahlspektren zeigen einen erwarteten monotonen Abfall der Fluktuationsstärke gemäß $S(k_\perp) \propto k_\perp^{-\alpha}$. Für das "ungünstige" Plasmaeinschlussregime (sogenannte L-Mode) werden, in sehr guter Übereinstimmung mit bisherigen Ergebnissen aus anderen Tokamakexperimenten, Spektralindizes von $\alpha \sim 4$ ermittelt. Aus den Messungen geht hervor, dass der Übergang von L-Mode zum Plasmaregime mit verbessertem Einschluss (sogenannte H-Mode) mit einer Abnahme der Turbulenzstärke verbunden ist. Für die H-Mode

wird ein Anstieg der Spektralindizes zum Plasmazentrum hin beobachtet, sodass vergleichsweise hohe Werte von $\alpha \sim 6 - 9$ erreicht werden. Eine Modifikation der Zusatzheizung durch den Einsatz von Elektronenzyklotronresonanzheizung bedingt eine Veränderung der $k_\perp$-Spektren, was auf einen Zusammenhang zwischen der Art der vorherrschenden Plasmaturbulenz und dem verwendeten Heizszenario hindeutet.

Danksagung

Die vorliegende Doktorarbeit wäre ohne die Arbeit und Unterstützung des gesamten ASDEX Upgrade Teams, dem ich hiermit meinen Dank ausspreche, nicht möglich gewesen.
Allen voran danke ich meinem Doktorvater, Prof. Hartmut Zohm, für die Aufnahme in dieses Forschungsteam und die Möglichkeit, am Max-Plack-Institut für Plasmaphysik an einem lehrreichen Projekt mitarbeiten zu dürfen. Ich bedanke mich bei ihm für die sehr interessante Aufgabe, die mir viel Spaß gemacht hat, und für seine stetige Unterstützung in allen Belangen.
Besonderer Dank gilt natürlich auch meinem fachlichen Betreuer Dr. Garrard Conway, der ausgesprochen viel Zeit aufgewendet hat, um mich bei dieser Arbeit zu unterstützen. Ich habe sehr von seinem Wissen über Mikrowellentechnik und Plasmaphysik profitiert, und vor allem von der Tatsache, dass er sich immer Zeit für mich genommen hat. Thank you, Garrard, for being such a dedicated supervisor.
Meiner Vorgängerin Dr. Jasmine Schirmer danke ich für ihre freundliche Hilfestellung in der Einarbeitungszeit.
Die Entwicklung und der Aufbau des neuen W-Band Doppler Systems wäre ohne die Hilfe und Beiträge einiger Kollegen sicherlich nicht denkbar gewesen. Insbesondere danke ich in diesem Zusammenhang Dr. Wolfgang Suttrop und Horst Eixenberger für ihre unentbehrliche Unterstützung. Desweiteren gebührt unserem Diagnostiktechniker Ewald Schmid besonderer Dank, sowie Gerold Schramm und den Mitgliedern seiner Elektonikabteilung, insbesondere Ludwig Kammerloher und Sven Klink.
Prof. Frank Jenko und seiner Arbeitsgruppe, ganz besonders Tobias Görler, danke ich für sehr hilfreiche Diskussionen rund um das Thema Plasmaturbulenz, die sehr zu meinem Verständnis auf diesem Gebiet beigetragen haben, sowie für die Durchführung individueller Turbulenzsimulationen.
Besonderer Dank richtet sich an meinen Promotionskollegen Andreas Schmid, der sich diesen durch unermüdliche Hilfestellung bei allerlei Problemchen während der letzten drei Jahre verdient hat.
Meinem Gruppenleiter Dr. Francois Ryter danke ich dafür, dass er mir stets das für mich so wichtige Feedback gegeben hat. Seine Wertschätzung meiner Leistungen hat mich immer sehr aufgebaut und motiviert, wofür ich ihm eigentlich gar nicht genug danken kann.

Diese Doktorarbeit widme ich meinen Eltern, Christa und Rudolf Tröster.

Abstract

An essential challenge in present fusion plasma research is the study of plasma turbulence. The turbulence behavior is investigated experimentally on the ASDEX Upgrade tokamak using Doppler reflectometry, a diagnostic technique sensitive to density fluctuations at a specific wavenumber $k_\perp$. This microwave radar diagnostic utilizes localized Bragg backscattering of the launched beam (k_0) by the density fluctuations at the plasma cutoff layer. The incident angle θ selects the probed $k_\perp$ via the Bragg condition $k_\perp \approx 2k_0 sin\theta$. The measured Doppler shifted frequency spectrum allows the determination of the perpendicular plasma rotation velocity, $u_\perp = v_{E\times B} + v_{turb}$, directly from the Doppler frequency shift ($f_D = u_\perp k_\perp / 2\pi$), and the turbulence amplitude from the backscattered power level. This thesis work presents a survey of $u_\perp$ radial profiles and $k_\perp$ spectrum measurements for a variety of plasma conditions obtained by scanning the antenna tilt angle. This was achieved by extending the existing V-band Doppler reflectometry system ($50 - 75\,\mathrm{GHz}$) with a new W-band system ($75 - 110\,\mathrm{GHz}$), which was especially designed for measuring the $k_\perp$ spectrum and additionally expands the radial coverage into the plasma core region. It consists of a remote steerable antenna with an adjustable line of sight allowing for dynamic wavenumber selection up to $25\,\mathrm{cm}^{-1}$ and a reflectometer with a 'phase locked loop' stabilized transmitter allowing for the precise determination of the instrument response function. The proper system functionality was demonstrated by laboratory testing and benchmarking against the V-band system. The new profile measurements obtained show a dependence of $u_\perp$ on the probed $k_\perp$. The observations indicate that the shape of the turbulence $k_\perp$ spectrum is a significant factor in the $u_\perp$ measurement. The results also suggest that the contribution of the intrinsic turbulence phase velocity v_{turb} to the measured $u_\perp$ may not be negligible in some cases. The measured turbulence $k_\perp$ spectra exhibit the expected monotonic power falloff with $S(k_\perp) \propto k_\perp^{-\alpha}$. For the low (L) confinement mode the spectral index is found to agree very well with previous results from other tokamak experiments with $\alpha \sim 4$. The measurements show that the transition from L-mode to high (H) confinement mode is accompanied by a reduction of the turbulence level. In H-mode the spectral index is observed to increase towards the core reaching comparatively high values with $\alpha \sim 6 - 9$. Altering the heating scenario by applying additional electron cyclotron resonance heating effects the $k_\perp$ spectra indicating a link between the plasma turbulence and the heating scheme.

Contents

Chapter 1

Introduction

The steadily increasing world's energy consumption [1] requires alternative energy resources for the future. One option could be controlled nuclear fusion. By fusing light nuclei to a heavier one, energy is released. This energy yield corresponds to the mass difference of the nucleus with respect to the source nuclei according to Einstein's energy-mass relation $E = \Delta m \cdot c^2$. In particular the fusion of hydrogen isotopes into stable helium offers the highest energy release per mass unit. Here, the most accessible fusion process is the deuterium-tritium reaction:

$$\mathrm{D} + \mathrm{T} \rightarrow {}^4\mathrm{He}\ (3.5\,\mathrm{MeV}) + \mathrm{n}\ (14.1\,\mathrm{MeV}) \tag{1.1}$$

A fusion process occurs only if the reacting nuclei can overcome the repulsive Coulomb forces. This requires very high particle energies, but there is also the possibility for tunneling through the Coulomb barrier at lower energies. The tunneling probability strongly depends on the relative velocity of the particles and consequently increases with thermal energy. However, the chance for a fusion reaction to occur is much smaller than for elastic Coulomb scattering. Hence, the particle interactions are dominated by Coulomb collisions and not by fusion reactions. As a consequence, confined particles will reach a thermal equilibrium resulting from many Coulomb scattering processes.
The fusion rate for the thermonuclear D-T fusion reaches a maximum at temperatures of about $15\,\mathrm{keV}$ ($1\,\mathrm{eV} \approx 11600K$). At these thermal energies the hydrogen atoms are ionized and form a plasma of ions and electrons. In order to serve as an energy producing system the thermalized D-T plasma needs to satisfy the Lawson criterion

$$n\tau T > 3 \times 10^{21}\ \mathrm{m}^{-3}\mathrm{keVs} \tag{1.2}$$

where n is the plasma density, τ is the energy confinement time and $T \approx 10 - 20\,\mathrm{keV}$ is the temperature. This ignition condition is deduced from a positive energy balance and has not been reached yet in present fusion plasmas. Nevertheless, D-T fusion has already been demonstrated successfully [2, 3]. Since an ignited plasma is heated almost entirely by the fusion-born ^{4}He particles via collisions, external energy supply is required only for plasma start-up and control but not for sustaining the plasma.

The charged plasma particles can be confined by an external magnetic field, forcing the particles to follow the field lines. Generally, a toroidal magnetic field geometry is used for confining the plasma to avoid the large end losses of a linear configuration. Unfortunately, a simple toroidal system with a purely toroidal magnetic field (B_{tor}) is an unstable configuration, since the gradient and the curvature of the field cause vertical particle drifts that are in opposite directions for ions and electrons. The resulting charge separation generates a vertical electric field, which leads in combination with the toroidal magnetic field to a radial outward $E \times B$ drift of the plasma, strongly reducing the confinement. The charge separation can be minimized by adding a poloidal magnetic field component (B_{pol}) to the toroidal field. The field lines then wind helically around the torus and form a set of nested magnetic flux surfaces. The necessary poloidal field can be generated either externally by coils (stellarator principle) or by a toroidal plasma current (tokamak principle). For the tokamak this current is produced by induction, where the plasma acts as the secondary winding of a transformer. The geometry of the field lines in a tokamak is described by the safety factor q, which is defined as the ratio of toroidal (m) to poloidal (n) circulations of a magnetic field line, completed when it closes: $q = \lim_{l\to\infty} m/n$ (l is the path length along the field line). The plasma tries to extend radially due to expansive forces that are caused by the kinetic plasma pressure plus the repulsive effect of opposite directed currents in a loop (torus). To compensate for that, a vertical magnetic field (B_z) is required to stabilize the plasma. In addition to position control, this field is also used for plasma shaping. The basic tokamak concept is shown in figure 1.1.

In a magnetically confined plasma the particles can flow along the field lines freely, but their motion perpendicular to the field is governed by the Lorentz force, which forces them to gyrate around the field lines. The resulting particle trajectories are helices following the magnetic field. However, the confinement of the particles is not perfect. Indeed there is particle flow perpendicular to the field. The so-called classical radial transport has two components. Convective transport due to the $E \times B$ drift of the particles can be controlled as already mentioned above. Gradient-driven diffusive transport is caused by particle collisions and cannot be prevented as easily. Per collision, the typical radial displacement of a particle is one gyro radius. In toroidal confinement devices the trapped particles also contribute to the radial transport. The magnetic field configuration of a tokamak is such that B is not constant along the field lines (B_{tor} decreases with one over major radius). Along the field line, the particle's parallel velocity $v_{||}$ decreases as the magnetic field increases as a consequence of the invariance of the magnetic moment $\mu = mv_{\perp}^2/2B$ ($v_{\perp}$ is the particle's velocity perpendicular to B). If the particle's kinetic energy is not sufficient to allow for $v_{||} > 0$ along the field line, the particle gets reflected (magnetic mirror principle). These trapped particles follow so-called banana orbits. Since their radial excursions are much larger than a gyro radius, the diffusion rate caused by collisions involving trapped particles exceeds the classical diffusion rate. The corresponding transport is called neoclassical. A characteristic of this transport is the strong dependence on the collisionality ($\nu^* \propto n/T^2$) of

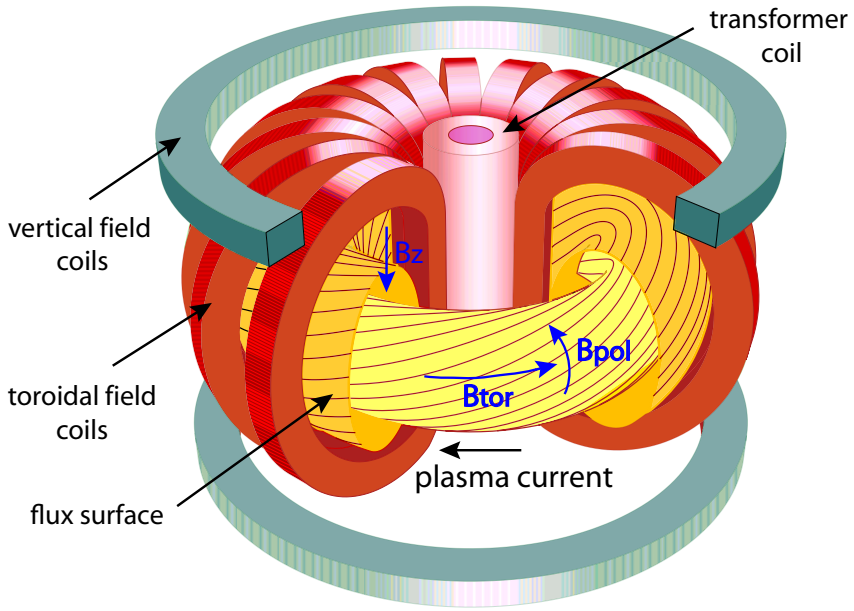

Figure 1.1: Tokamak concept. The plasma is confined using a combination of three different magnetic fields generated by field coils (B_{tor}, B_z) and the plasma current (B_{pol}), which is induced by a transformer coil. The ratios of the fields are roughly $B_{tor} : B_{pol} : B_z \cong 100 : 10 : 1$.

the plasma. The radial transport measured in fusion experiments however is in general considerably larger than predicted by neoclassical theory. The difference between experimentally observed and neoclassical transport is called anomalous transport and is attributed to plasma turbulence. In general, convective transport dominates the diffusive transport and hence determines the quality of confinement in a magnetized plasma. In fact, the ignition condition (equation 1.2) has not been reached yet in present fusion devices, because anomalous transport reduces the confinement time substantially. Hence, progress in understanding turbulent transport is a very important issue on the route to a fusion reactor.

Understanding the plasma turbulence behavior requires spatial and temporal measurements of its properties, such as amplitude, frequency spectrum $S(\omega)$, wavenumber spectrum $S(k)$ and dispersion relation. In general, fluctuations in various plasma parameters, such as density $\tilde{n}$, temperature $\tilde{T}$ and associated potential $\tilde{\Phi}$ and magnetic field $\tilde{B}$, can contribute to the anomalous transport. A powerful diagnostic technique for measuring the spatial turbulence characteristics is microwave Doppler reflectometry. The technique is based on Bragg scattering of electromagnetic waves by turbulent density fluctuations $\tilde{n}$, due to its sensitivity to a specific turbulence wavenumber. Thus, the scaling of fluctuation levels with the wavenumber (k spectrum) can be measured, which provides information on the nonlinear turbulence dynamics.

The study of the turbulence wavenumber spectrum is the central subject of this thesis. For this purpose, the Doppler reflectometry system of the ASDEX Upgrade tokamak has been extended with a new diagnostic channel consisting of a steerable antenna with a variable line of sight and a W-band reflectometer ($75-110\,\mathrm{GHz}$). The new antenna configuration allows for dynamic wavenumber selection up to $25\,\mathrm{cm}^{-1}$ and the W-band reflectometer extends the radial coverage into the core compared to the existing V-band system ($50-75\,\mathrm{GHz}$). The reflectometer hardware has been developed and implemented in the course of this thesis project. Using the new system, first measurements on ASDEX Upgrade of the wavenumber spectrum were performed for a variety of plasma conditions. This thesis work presents a comparison of wavenumber spectra obtained for low and high plasma confinement (L- and H-mode) and for different heating scenarios. Especially, the H-mode measurements are of interest, since they contribute to reduce the lack of observations in this area of turbulence studies. Using Doppler reflectometry as a diagnostic technique allows for a better spatial resolution compared to forward microwave or laser scattering usually utilized for wavenumber spectrum measurements. In addition, a survey of radial profiles of the perpendicular plasma rotation velocity is presented. Here, the new measurements contribute to the characterization of the diagnostic technique.

The content of this thesis is organized as follows. Chapter 2 reviews the basics of fluid turbulence and introduces the different types of turbulence relevant in tokamak plasmas. In chapter 3 a description of the ASDEX Upgrade tokamak is given. The principle of Doppler reflectometry is introduced in chapter 4 and the multichannel Doppler system is described in detail with emphasis on the hardware of the new W-band reflectometer system. Chapter 4 also includes a description of the measurement technique and the data analysis methods used. The diagnostic capabilities and the cross-validation of the W-band system are presented in chapter 5 as well as the dedicated discharge scenarios used to obtain the measurements presented in chapters 6 and 7. The measured perpendicular rotation velocity profiles are described and discussed in chapter 6. In chapter 7 the measured turbulence wavenumber spectra are presented and discussed. A more comprehensive discussion of the experimental results is given in chapter 8. The last chapter is a summary plus outlook.

Chapter 2

Turbulence

The quality of particle and energy confinement in magnetized fusion plasmas is to a large extent determined by anomalous transport, which dominates over the neoclassical diffusive transport. This large convective transport observed in fusion experiments is attributed to plasma turbulence. Hence, progress in understanding turbulence behavior is an important issue of modern plasma physics.
In the next section the basics of general fluid turbulence are outlined as an introduction to the topic. Then, a basic survey of turbulence in magnetized fluids is given in the subsequent section.

2.1 Turbulence basics

Fluid flows are caused by pressure or temperature gradients or by shearing or stirring of the fluid. For moderate drive the flow is laminar, but for strong drive it becomes turbulent. The transition from laminar to turbulent flow occurs when the Reynolds number exceeds a critical value $Re > Re_{crit}$. The Reynolds number is the ratio of the inertial forces to the viscous forces.

$$Re = \frac{vL}{\nu} = \frac{\text{inertial forces}}{\text{viscous forces}} \tag{2.1}$$

where v is the characteristic flow velocity, L is the characteristic geometric dimension, and ν is the kinematic viscosity of the fluid. For low Reynolds numbers the viscous forces are dominant and the flow is laminar, i.e. characterized by smooth, constant fluid motion, while for high Reynolds numbers the inertial forces are dominant and the flow is turbulent. Within a certain range around Re_{crit} there is gradual transition between the different flow regimes, where the flow is neither fully laminar nor fully turbulent. Figure 2.1 shows an example for the transition from laminar to turbulent flow [4]. In fact, laminar flows are the exceptions; generally the dynamic behavior of fluids is turbulent. The characteristic properties of turbulence can be described as follows:
i) Turbulent flows are disordered, random and chaotic. They are characterized by strong irregularities both in space and time.
ii) However, turbulent flows can exhibit a kind of organization. The formation of

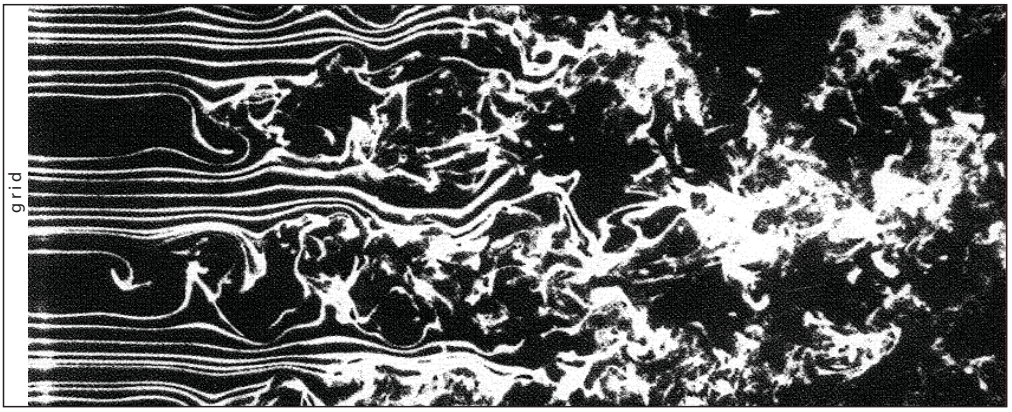

Figure 2.1: Transition from laminar to turbulent flow visualized by smoke lines passing through a grid [4].

coherent structures is a characteristic feature of turbulence.
iii) In a turbulent system, many length and time scales exist simultaneously, which often span 3-4 orders of magnitude.
iv) Turbulence is a self similar phenomenon. Structure and spectral functions depend on length scales or the wavenumber according to power laws.
v) Strong turbulent activities concentrate in alternating spatial-temporal regions. The occurrence of temporal breaks and spatial holes in the turbulent activity is called intermittency.
In all, these properties show that turbulent flows are complex nonlinear dynamic systems with many spatial and temporal degrees of freedom. Hence, a deterministic description of a turbulent system is not possible. The irregular dynamics require a statistical description based on averaging over regions of space or intervals of time. Fully developed turbulence is characterized by saturation which is a quasi stationary state of the turbulent flow. This statistical equilibrium is regarded as independent of its initial conditions. Another important characteristic of turbulent flows is that the convective cross transport is significantly faster than the diffusive transport.

A turbulent flow is composed of eddies of many different sizes. Turbulence requires continuous energy supply, otherwise it decays and the system relaxes to equilibrium. At a certain range of spatial scales, energy is introduced into the fluid motions. In general, the energy input is at the large turbulence scales, where viscosity is insignificant and Re is large. For three-dimensional fluid turbulence these large eddies experience a shearing motion tearing them apart at roughly the same rate at which they are formed, so that there is a statistical equilibrium. While breaking up into smaller eddies, they transfer their kinetic energy to the next smallest scale. This nonlinear process conserves energy, so the energy taken out of the source range is passed to other scales. At each scale below the source range, there is a statistical balance mostly between energy passed in from the next larger scale, and energy passed

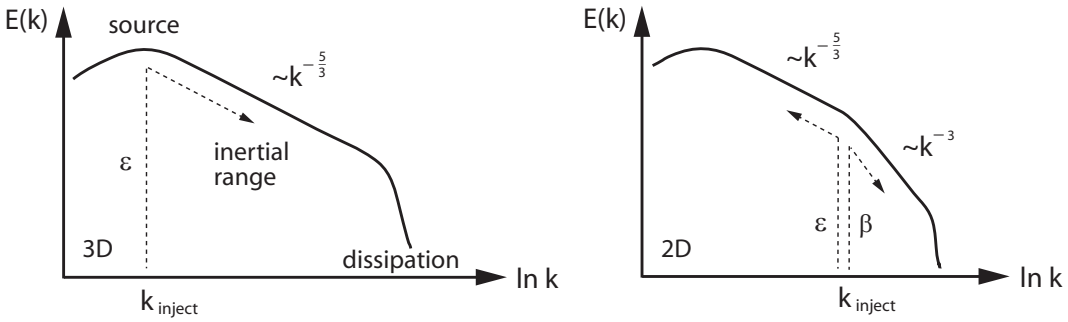

Figure 2.2: (Left) Spectrum for three-dimensional fluid turbulence. Three regions can be classified: source range, inertial range, and dissipation range. In the inertial range the kinetic energy depends on the wavenumber according to a power law. (Right) Spectrum for two-dimensional fluid turbulence, characterized by a dual energy ϵ-enstrophy β cascade. For both cases the turbulence is assumed to be isotropic and homogeneous.

further to the next smaller scale. The energy transfer process between scales, called energy cascade, continues until the scale is small enough for viscosity to become important (i.e. the viscous forces become comparable to the inertial forces). The shearing rate tearing the eddies apart at each scale is proportional to the vorticity $w = \nabla \times v$ of the flow at that scale and increases towards smaller scales. Hence the fluid enstrophy ($\sim \frac{1}{2}w^2$) must grow during this direct cascade. At the smallest scales the energy is dissipated by viscous action. Thus, a turbulent flow is an open system with continuous energy flow through the system. Energy that is injected at large scales is redistributed by nonlinear interactions and finally dissipated. The energy cascade in the range between source scales and dissipation scales is described by Kolmogorov's spectral law:

$$E(k) \sim \epsilon^{\frac{2}{3}} k^{-\frac{5}{3}} \tag{2.2}$$

where k is the wavenumber, $E(k)$ is the kinetic energy at the scale $1/k$, and ϵ is the energy transport rate per time and mass. Within this so-called inertial range the energy transfer is local and independent of the scale, thus the dynamics is self similar. Figure 2.2 shows the corresponding wave number spectrum for a homogeneous and isotropic 3D turbulence.

The situation is different in isotropic two-dimensional fluid turbulence (e.g. flowing soap films), because in addition to energy, enstrophy is also conserved [5]. For the energy cascade to be direct (towards smaller scale) the enstrophy must grow. So, with enstrophy conserved we cannot have the cascade of energy to smaller scales. The energy cascade is in that case directed towards larger scales, with the same spectral dependence $E(k) \sim \epsilon^{2/3} k^{-5/3}$, leading to the formation of large turbulence structures. This process is called inverse energy cascade. The enstrophy is redistributed towards smaller scales. Hence, the enstrophy cascade is direct and follows a power law $E(k) \sim \beta^{2/3} k^{-3}$ down to the dissipation scale. Here, β is the enstrophy

transfer rate. The overall process is called a dual cascade, since the two quantities are transferred in opposite directions in the spectrum (figure 2.2). Thus, the spectrum has two inertial ranges on either side of some intermediate length scale k_{inject} at which energy/enstrophy is injected continuously.
The formation of coherent structures can play an important role in this context, since these structures alter the cascading behavior and hence modify the energy spectrum.

2.2 Turbulence in magnetized plasmas

In a fusion plasma transport along the field lines is fast. Hence, no density or temperature gradients can form on a magnetic flux surface, since parallel flows are equalizing any differences. Consequently, in addition to pressure, temperature and density are also constant on the flux surface. Perpendicular to the magnetic surfaces the particle motion is strongly restricted by gyration resulting in comparatively small radial flow. Therefore, gradients of pressure, density and temperature can form in the direction perpendicular to the magnetic surfaces. Because of the strong anisotropy of flow dynamics induced by the magnetic field, fluctuations of various plasma parameters have an extreme anisotropic structure: small scale perpendicular to the field and large scale parallel to the field. In other words, the perpendicular and parallel wavenumbers of the fluctuations are very different with $k_\perp \gg k_\parallel$. Hence, in planes locally perpendicular to the magnetic field turbulent flows in tokamak plasmas are very similar to flows in two-dimensional fluid systems. However, plasma turbulence may depart from this simplified 2D picture, since 3D effects cannot be ignored [5].

In the presence of fluctuating electric and magnetic fields the plasma particles deviate from their unperturbed trajectories. The radial variation of an electron in terms of its velocity is given by

$$\tilde{v}_r = \tilde{v}_{Er} + v_\parallel \tilde{B}_r / B_0. \tag{2.3}$$

Here, $\tilde{v}_{Er}$ is the radial component of the $E \times B$ velocity and the second term corresponds to the radial projection of particles following the perturbed magnetic field line. The tilde denotes the disturbances on the equilibrium. The resulting radial particle transport is

$$\Gamma \equiv \int \tilde{v}_r \tilde{f}_e \; d^3v, \tag{2.4}$$

where $\tilde{f}_e$ is a small disturbance of the Maxwellian distribution function of the electrons. The spatial-temporal average of this fluctuation induced transport is

$$\langle \Gamma \rangle = \langle \tilde{n}_e \tilde{v}_{Er} \rangle + n_{e0} \langle \tilde{u}_{e\parallel} \tilde{B}_r \rangle / B_0, \tag{2.5}$$

with $\langle \tilde{n}_e \rangle = \langle \tilde{u}_{e\parallel} \rangle = \langle \tilde{v}_{Er} \rangle = \langle \tilde{B}_r \rangle = 0$. Here, n_e is the electron density and u_e is the average velocity. According to equation 2.5 the particle transport is directly linked to the correlation functions $\langle \tilde{n}_e \tilde{v}_{Er} \rangle$ and $\langle \tilde{u}_{e\parallel} \tilde{B}_r \rangle$. In fact, the radial transport can

be small even for relatively high fluctuation levels, if these terms are small.
The radial electron heat flux is defined analog to equation 2.4:

$$Q_e \equiv \int (\frac{1}{2} m_e v^2) \tilde{v}_r \tilde{f}_e \; d^3v \tag{2.6}$$

The average heat transport perpendicular to the magnetic field is

$$\langle Q_e \rangle = \frac{3}{2} \langle \tilde{p}_e \tilde{v}_{Er} \rangle + \langle \tilde{q}_{e\|} \tilde{B}_r \rangle / B_0 + \frac{5}{2} p_{e0} \langle \tilde{u}_{e\|} \tilde{B}_r \rangle / B_0, \tag{2.7}$$

where p_e is the plasma pressure and $q_{e\|}$ is the parallel heat flux.
It is evident from equations 2.5 and 2.7 that turbulent fluctuations can lead to radial transport of mass and energy. The terms of these equations involving magnetic field fluctuations are called electromagnetic, the other terms electrostatic.

Electrostatic turbulence
This type of plasma turbulence is basically $E \times B$ fluid turbulence driven by the background gradients of various plasma parameters. While the associated mean profiles are almost constant in time, they are superposed with fast small scale fluctuations. Driven by the background gradients, these micro-instabilities grow exponentially in time until their amplitude reaches a value where nonlinear effects set in. The latter lead to saturation and a quasi stationary state away from thermodynamic equilibrium establishes. In this process free energy is extracted from the background plasma and redistributed via a direct cascade and finally dissipated. Note, that the basic properties of two-dimensional turbulence and associated cascade dynamics remain active. The transfer is a direct cascade in the fluid enstrophy and an inverse cascade in the $E \times B$ energy. Hence, for gradient driven turbulence both energy cascade tendencies are simultaneously present: inverse for the $E \times B$ turbulence and direct for the free energy.
An example is the turbulence driven by a radial density gradient. Small scale density fluctuations $\tilde{n}_e$ alter locally the mean density profile (n_{e0}), which is otherwise almost constant in time. Despite $\tilde{n}_e \ll n_{e0}$ the density gradient and with it the turbulence drive can vanish in a finite radial region. As a result the turbulent transport decreases and the density gradient builds up again. From this, the amplitude of the density fluctuations can be estimated. It is $|\nabla \tilde{n}_e| \sim |\nabla n_{e0}|$ with $|\nabla \tilde{n}_e| \sim k_\perp \tilde{n}_e$ and $|\nabla n_{e0}| \sim n_{e0}/L_n$, and hence

$$\frac{\tilde{n}_e}{n_{e0}} \sim \frac{1}{k_\perp L_n} \tag{2.8}$$

Here, $L_n \equiv n_e/|\nabla n_e|$ is the density scale length. The density fluctuation level in the plasma core is small but increases towards the edge.

The spectrum of electrostatic micro-instabilities in tokamak plasmas is quite rich. A large variety of modes can become unstable: Ion Temperature Gradient (ITG) modes [6, 7], Electron Temperature Gradient (ETG) modes [8, 9], Trapped Electron Modes (TEM) [10, 11], and Drift Waves (DW) [12, 13]. Depending on the plasma conditions, it is possible that more than one turbulence type may exist at

any particular place and time [14]. The different modes are characterized in particular by their typical length scale or equivalently the inverse of their wavenumber $1/k_\perp$.

Drift wave turbulence

In the edge region of a tokamak plasma drift waves are the dominating micro-instabilities. Here, the strong radial pressure gradient provides the drive for this kind of turbulence. In a simplified picture the gradient of the electron temperature ∇T_e is neglected such that the pressure gradient is $\nabla p_e = kT_e \nabla n_e$. ($T_e$ is the temperature of the isothermal electrons.) Periodic electron density fluctuations $\tilde{n}_e$ in the poloidal direction lead directly to fluctuations in the electrostatic potential $\tilde{\Phi}$ due to the fast parallel dynamics of the electrons. They obey the Boltzmann relation (adiabatic electrons):

$$\frac{\tilde{n}_e}{n_{e0}} = \frac{e\tilde{\Phi}}{kT_{e0}} \tag{2.9}$$

Figure 2.3 shows the formation of regions with enhanced and lowered density and the potential difference resulting from a perturbation of the density n_{e0} initially constant on a magnetic surface. As a consequence of locally varying potential, poloidal electric fields $\tilde{E} = -\nabla\tilde{\Phi}$ are induced. These fields lead in combination with the toroidal magnetic field to $E \times B$ drifts in the radial direction, such that the plasma moves radially back and forth. This oscillation of the plasma density is called a drift wave. While the drift velocity is oscillating radially, the drift wave propagates in the poloidal direction with the electron diamagnetic drift velocity

$$v_{De} = \frac{\nabla p_e \times B}{eB^2 n_{e0}} = \frac{kT_e}{eB}\frac{\nabla n_e}{n_{e0}}. \tag{2.10}$$

According to equation 2.5 the net radial transport is determined by the correlation function $\langle \tilde{n}_e \tilde{v}_{Er} \rangle$. If the phase difference between density and electric field is exactly $\pi/2$ then there is no net transport ($\langle \sin\omega t \ \cos\omega t \rangle = 0$). Hence, in the described case the drift wave causes a density modulation but no anomalous transport. However, due to dissipative effects (ion collisions, Landau resonances) the Boltzmann relation (equation 2.9) is not strictly valid (non-adiabatic electrons). The correlation function is then $\langle \tilde{n}_e \tilde{v}_{Er} \rangle \neq 0$ and a net transport in the radial direction occurs. Thus, in the plasma edge region anomalous transport is attributed to drift wave turbulence. The pressure gradient flattens towards the plasma core and hence the turbulence drive weakens there.

Ion temperature gradient turbulence

In the plasma core a radial ion temperature gradient ∇T_i is the drive for another type of instability: the toroidal ion temperature gradient instability. In a tokamak the gradient and the curvature of the magnetic field cause a vertical particle drift that is in opposite direction for ions and electrons

$$v_D = \frac{m_{e,i}}{q_{e,i}B^3}\left(v_\parallel^2 + \frac{1}{2}v_\perp^2\right) B \times \nabla B, \tag{2.11}$$

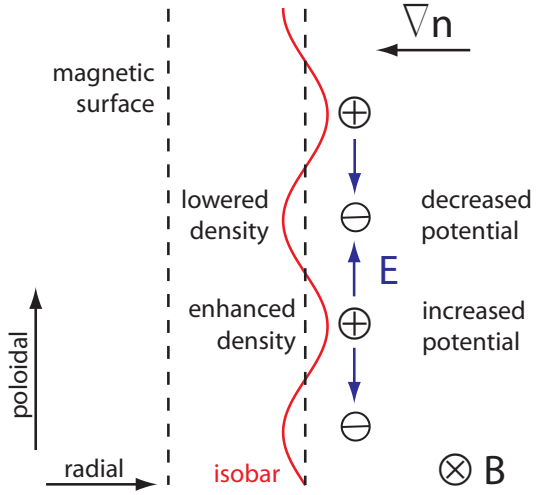

Figure 2.3: Mechanism of a drift wave. The wave propagates in the poloidal direction.

with electron/ion mass $m_{e,i}$ and charge $q_{e,i}$ [15]. The drift is approximately proportional to the kinetic energy of the particle. The magnetic field configuration in figure 2.4 is such that the ion drift is directed upwards. Starting with a periodical perturbation of the ion temperature on a magnetic surface, the ions from the locally hotter spot drift faster than those from a colder spot due to their higher energy. Hence, the ions accumulate above a hotter region and the ion density n_i increases there. By contrast, the density decreases below the hot spot due to the slower drift velocity of the colder ions. In this way an ion density perturbation $\tilde{n}_i$ is created from an ion temperature perturbation $\tilde{T}_i$. Quasi-neutrality involves $\tilde{n}_e = \tilde{n}_i$. Fluctuations in the electron density $\tilde{n}_e$ lead to fluctuations in the electrostatic potential $\tilde{\Phi} \sim \tilde{n}_e$ and hence to vertical electric fields $\tilde{E} \sim -\nabla\tilde{n}_e$. On the high field side of the tokamak the resulting $E \times B$ drift is directed such that hot plasma from more inner regions flows into the colder spots and cold plasma from more outer regions flows into the hotter spots. The initial temperature perturbation therefore decreases in time. On the low field side the drifts are in the same direction, but here that means that hot plasma from more inner regions flows into the hotter spots and cold plasma from more outer regions flows into the colder spots. This amplifies the initial temperature perturbation. Furthermore, hot plasma is transported radially outwards, which greatly reduces the confinement. An ITG mode usually rotates in the ion diamagnetic drift direction with a drift velocity

$$v_{Di} = \frac{\nabla p_i \times B}{q_i B^2 n_i}, \tag{2.12}$$

where $\nabla p_i = n_i k \nabla T_i + k T_i \nabla n_i$ is the ion pressure gradient.
An important property of this micro-instability is the existence of a turbulence threshold. The pure ITG mode is stable for an ion temperature gradient lower

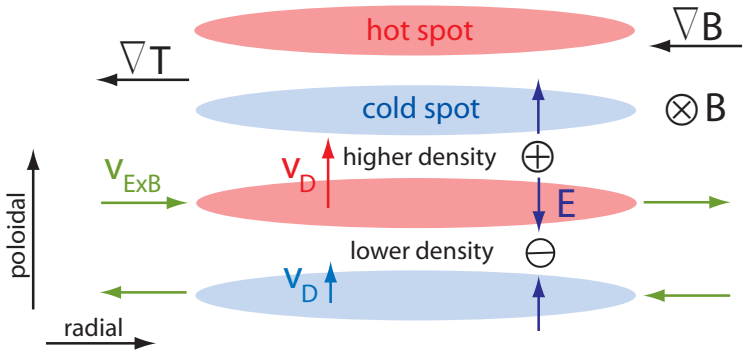

Figure 2.4: Mechanism of an ion temperature gradient instability for a situation at the low field side of a tokamak. The mode rotates poloidally.

than a critical normalized gradient

$$R\frac{|\nabla T_i|}{T_i} \equiv \frac{R}{L_{T_i}} < \frac{R}{L_{T_i,crit}}, \tag{2.13}$$

where R is the major plasma radius. Generally, $R/L_{T_i,crit}$ depends on the normalized density gradient $R|\nabla n_i|/n_i$ and on the ratio of electron to ion temperature T_e/T_i. When the ion temperature gradient crosses the stability threshold, the ITG mode grows exponentially and turbulent transport becomes very large. In this case, part of the temperature profile stays close to a marginal value and the gradients are stuck to their critical value. This is called profile stiffness.
The ITG mode has a typical scale longer than the ion gyro radius $\rho_i = \sqrt{m_i T_i}/q_i B$:

$$k_\perp \rho_i < 1 \tag{2.14}$$

Turbulence at this large scale is believed to be responsible for the major part of anomalous transport. This is consistent with fluctuations observed experimentally [16, 17], which are mainly distributed in the range $k_\perp \rho_i \simeq 0.1 - 0.5$ and strongly correlated with the high transport level. However, in high confinement regimes associated with the formation of a transport barrier, it is observed that the ion transport can be reduced down to neoclassical values, accompanied by a reduction of the large scale turbulence [18, 19, 20, 21].
ITG turbulence self-organizes through the formation of large scale structures, which back-react on the small scale fluctuations. Fluctuations in the electrostatic potential that depend on the radial coordinate only lead to $E \times B$ flow in the poloidal direction. These so-called zonal flows are generated by the turbulence itself and have a shearing effect on the turbulence eddies. This shearing process tears the eddies apart. Zonal flow spin-up thus may lead to a substantial reduction of the turbulence level and induced anomalous transport. Poloidal zonal flows are in that sense a self-regulation mechanism for ITG turbulence [22].

Electron temperature gradient turbulence

A further type of instability in the plasma core is driven by the electron temperature gradient ∇T_e. Linearly, the electron temperature gradient mode bears strong resemblance to the ITG mode, with the roles of electrons and ions inverted. ETG turbulence also exhibits a stability threshold and causes electron temperature profile stiffness. Toroidal ETG modes are unstable when the electron temperature gradient exceeds a critical normalized gradient $R/L_{T_e,crit}$. Among other parameters which characterize the magnetic field geometry, the threshold depends primarily on the ratio T_e/T_i and also on the normalized density gradient R/L_n [23]. The rotation direction of the mode is usually the electron diamagnetic drift direction. An ETG mode occurs at small scale with

$$k_\perp \rho_e \sim 1 \quad \text{or} \quad k_\perp \rho_i \gg 1. \tag{2.15}$$

However, nonlinear numerical studies have shown that ETG modes have a typical scale length larger than the electron gyro radius ($\rho_e = \sqrt{m_e T_e}/eB$) due to the formation of long scale structures elongated in the radial direction [8]. These so-called streamers lead to a large turbulent convection down the gradient greatly enhancing anomalous transport. Thus, these modes may contribute significantly to electron transport and could account for the different behavior of ion and electron thermal transport in high confinement regimes, where the ion transport can be reduced down to neoclassical values, while the electron transport remains at a high level. ETG streamers may also be involved in causing the stiffness of electron temperature profiles that is observed in experiments [24]. The role of ETG turbulence should be central for dominant electron heating. This will be the case in burning fusion plasmas since the alpha particles will heat mainly the electrons. Experimental observations in the high wavenumber range are challenging and require a sensitive technique due to the very low fluctuation level in this spectral range.

Trapped electron mode turbulence

This type of core turbulence is associated with electrons which are magnetically trapped in the low field outboard region of a tokamak. These non-adiabatic electrons introduce trapped electron modes (TEM). They are driven by electron pressure gradients ∇p_e in the presence of magnetic curvature. A separate treatment of ITG and TEM turbulence is usually an oversimplification. Nevertheless, there exists experimental situations where one turbulence type is dominant, for instance when one species is hotter than the other. In discharges with dominant central electron heating, the ions are relatively cold, and ITG modes are linearly stable, while TEMs are not. So, depending on the local plasma parameters, ITG modes and TEMs may either coexist or else be the only instability at ion gyro radius scales. The general case is however that TEMs and ITG modes coexist. In this context, the key parameters are the normalized gradients of the background density and electron and ion temperature. The instability threshold for TEMs appears at a critical value of R/L_{T_e} and also depends on the fraction of trapped electrons. Hence, the threshold is affected by the collisionality of the plasma. TEMs are driven by R/L_{T_e} and/or R/L_n, whereas ITG modes are driven by R/L_{T_i} and suppressed by R/L_n

[10]. Contrarily to ITG modes, TEMs usually rotate in the electron diamagnetic direction. TEM turbulence appears mostly in the long wavelength range with perpendicular wavenumbers in the order of

$$k_\perp \rho_i < 1 \quad \text{or} \quad k_\perp \rho_s < 1, \tag{2.16}$$

where the length scale ρ_s is the ion gyro radius evaluated with the electron temperature:

$$\rho_s = \frac{\sqrt{m_i T_e}}{eB} \tag{2.17}$$

Low wavenumber turbulence is believed to cause most of the experimentally observed anomalous transport. Particularly the contribution of TEM turbulence can be significant due to the formation of elongated vortices (streamers) with a radial extent of up to $60\rho_s$ [10]. Such spatial structures have also been observed in nonlinear simulations of ETG modes. However, the TEM streamers seem to be less pronounced than their ETG counterpart. The influence of zonal flow dynamics on the transport level of TEM turbulence seems to be small. This implies that TEM turbulence and ITG turbulence must be different with respect to their saturation mechanisms [25, 11].

Transport suppression

A fundamental issue for fusion plasmas is to reach situations where the turbulent transport is low, that is, with an improved confinement. Two generic key parameters are known to play a central role in stabilizing and suppressing turbulence [26, 19]: flow shear and magnetic shear. Turbulent transport reduction due to $E \times B$ shear flow results essentially from the shearing of turbulent convective cells. With increasing shear the eddies are deformed and finally torn apart into smaller ones. The reduction of the eddy size is accompanied by a decrease of the associated transport. An approximate criterion for shear flow stabilization is $\gamma_E > \gamma_{lin}$, where γ_{lin} is the maximum linear growth rate of the turbulence and γ_E is the flow shear rate defined as $\gamma_E = \nabla_r(E_r/B)$ [27]. The index r denotes the radial direction. Magnetic shear has a stabilizing effect on many micro-instabilities including TEM, ITG and ETG modes. Therefore, increasing magnetic shear $s \equiv (r/q)\nabla_r q$ leads to larger values of the critical gradients. (q is the safety factor.) Flow shear and/or magnetic shear play a central role in the formation and sustainment of transport barriers. Edge and internal transport barriers (ETBs and ITBs) are regions where turbulence is reduced or quenched. These regimes are usually reached above a critical value of the heating power and are now routinely produced and maintained in tokamaks.

Fluctuation measurements

Several diagnostics have been developed to measure fluctuations in tokamak plasmas. The most commonly used diagnostics are Langmuir probes [28], coherent laser scattering [29], standard reflectometry [30], Doppler reflectometry (microwave scattering) [31], heavy ion beam probe (HIBP) [28], and Beam Emission Spectroscopy [32]. They measure mostly fluctuations in the plasma density. The

scattering diagnostics are powerful techniques for the purpose of fine scale analysis, because they provide directly the space Fourier transform of the fluctuating density at a specified wavenumber. Langmuir probes and HIBPs are able to measure also fluctuations in the electrostatic potential. Unfortunately, probes are heat sensitive and thus can only be used at the plasma edge. The role of all these diagnostics has been crucial in the past to demonstrate that turbulence is responsible for anomalous transport in tokamaks. Since then, several studies have confirmed the close connection between micro-instabilities and transport. Several pending issues remain, however. For example, a challenge is still to prove the existence of large scale streamer activity.

Measurements of spatial fluctuation characteristics provide key elements for turbulent transport analysis. The distribution of fluctuation levels among the scales characterizes the nonlinear dynamics and the energy transfer processes between scales. Therefore, the scaling of the fluctuation magnitude with the wavenumber is of particular interest, since it provides information on the turbulence mechanisms. The fluctuation wavenumber spectrum $S(k_\perp)$ is measured mainly by scattering diagnostics for their high wavenumber resolution. Since a large variety of modes are potentially unstable, fluctuations on a wide range of scales should be measured. It is observed that the fluctuation energy is concentrated at lower wavenumbers, indicating a prominent role of the large scale fluctuations. Further, the wave number spectrum is found to fall off monotonically above its maximum, following a power law $S(k_\perp) \sim k^{-\alpha}$. The measured spectral index is $\alpha \approx 3.5 \pm 0.5$ for most experiments examining ohmic and L-mode plasmas typically with forward microwave or laser scattering techniques [17, 33, 34, 35]. Measurements of α in H-mode plasmas are however extremely sparse. The high wavenumber domain has raised new interest recently because of its possible implication in electron transport.

Chapter 3

ASDEX Upgrade tokamak

One of Europe's largest tokamak fusion experiments, ASDEX Upgrade, is in operation at the Max-Planck-Institut for Plasma Physics (IPP) in Garching near Munich. The tokamak was commissioned in 1990 and the first plasma was produced in March 1991 [36]. Figure 3.1 shows a poloidal cross section of the experiment. (The basic tokamak principle was introduced in chapter 1.) ASDEX Upgrade was configured as a tokamak with reactor relevant coil geometry. The design of ASDEX Upgrade is close to the design planned for the next step fusion device ITER [37]. In fact, ITER resembles the ASDEX Upgrade configuration, but scaled up by a factor of about 4. ASDEX Upgrade is the follow-up project of the ASDEX tokamak. The name 'ASDEX' stands for **A**xial **S**ymmetric **D**ivertor **EX**periment and indicates that the tokamak has a divertor configuration. This is a special magnetic field configuration that allows for a controlled limitation of the plasma by a magnetic boundary called the seperatrix. The field lines outside the separatrix intersect the walls at special vessel components - the divertor plates. These plates are located at some distance from the hot bulk plasma, so that the zone of intense plasma-surface interaction is kept away from the bulk plasma. This greatly diminishes contamination of the plasma by impurities from the vessel walls released mainly by sputtering. Even at high fusion temperatures atoms of high-Z elements are not fully ionized. They absorb (thermal) energy from the plasma and release the energy as UV or X-ray radiation (radiation losses), which leads to a cooling of the plasma. The divertor concept also facilitates the removal of impurities. The plasma outside the separatrix flows along the field lines onto the divertor plates where the plasma particles are neutralized. At ASDEX Upgrade the neutral gas at the divertor plates including the impurities is pumped by turbomolecular pumps and a cryopump. Whereas most parts of the vessel wall are protected from intense plasma contact, the divertor plates are exposed to strong heat loads, potentially leading to strong erosion of the plate material.

The magnetic divertor configuration is generated by a system of 6 poloidal field coils. These coils are also used for shaping the plasma. Additionally, a group of internal and external coils are used for controlling the basic radial and vertical plasma position. Hence, a variety of plasma configurations with different plasma cross sections can be generated with this set of coils. The main toroidal field is

produced by a set of 16 D-shaped copper coils. The total magnetic field strength is typically $2 - 2.5\,\mathrm{T}$ with a field ripple amplitude at the outer plasma edge of about 1% [36]. A central solenoid acts as the primary coil of a transformer. Ramping the current in this transformer coil induces a loop voltage inside the vacuum vessel that leads to plasma break down. The resulting plasma current is typically in the range of $0.8 - 1.2\,\mathrm{MA}$. The steel vacuum vessel is composed of 16 torus sectors. Various ports of different sizes provide radial and vertical access to the vacuum vessel interior. The electrical power for running the experiment (plasma operation) is provided by three flywheel generators. The generator EZ2 (150 MW) supplies the toroidal field coils, the generators EZ3 (140 MW) and EZ4 (220 MW) supply the vertical field coil system and the auxiliary heating systems (see below). The available generator power allows for a plasma pulse duration of up to 10 s followed by a 20 min interval to re-accelerate the flywheel generators and to cool down the magnetic field coils. Technical data of the tokamak and typical values of the plasma parameters are listed in table 3.1. (Note that in the 2007 campaign the operation of the experiment was somewhat restricted due to a failure of the EZ4 power supply.)
A conventional wall material for fusion devices is carbon. Although carbon has favorable properties like high heat resistance and low Z, its main disadvantage is that it will entrap tritium in deposit layers, thus enhancing rapidly the tritium inventory in the vessel above the permitted level of future fusion devices [38]. Testing of alternative wall materials, such as tungsten, is hence of interest. For this reason ASDEX Upgrade has entered a multi-step program towards a carbon free vessel by stepwise covering all plasma facing components with tungsten [39, 40]. From the 2007 campaign on the entire interior of the vessel is covered with tungsten. As a full-tungsten device ASDEX Upgrade is unique among all tokamaks. Usually, thin coatings of boron are applied to the walls by means of a glow discharge to getter oxygen and thus improving the discharge conditions. However, ASDEX Upgrade has successfully demonstrated the start up of a 100% tungsten tokamak without this boron layer.
In order to compensate the intrinsic heat losses of the plasma, external heating must be applied. Although the electrical current flowing in the plasma creates heat through resistivity, this ohmic heating becomes inefficient above temperatures of about 1.5 keV, since plasma resistivity is decreasing with increasing temperature ($\sim T_e^{-3/2}$). Fusion relevant temperatures can only be achieved by heating the plasma externally via different methods: Radio frequency heating is based on the absorption of energy from high power electromagnetic waves at the fundamental cyclotron resonance frequency of ions or electrons or at the harmonics. The energy absorbed from the wave field by the resonant particles is then distributed via collisions to other plasma particles. The ion cyclotron resonance heating (ICRH) system on ASDEX Upgrade operates with tunable radio frequencies in the ion cyclotron range ($30 - 120\,\mathrm{MHz}$) [41, 42]. Four in-vessel loop antennas, each supplied by its own generator, can couple up to 8 MW of ICRH power to the plasma. In addition to transferring the wave energy to the ions at the cyclotron frequency, it is also possible to heat the electrons directly when the phase velocity of the wave is near the thermal velocity of the electrons (Landau damping). Another method to

Total height	9 m
Total radius	5 m
Weight	800 t
Material of plasma facing components	100% tungsten
Magnetic field	2.0 - 2.5 T
Plasma current	0.8 - 1.2 MA
Pulse duration	$<$10 s
Time between pulses	15 - 20 min
Ohmic heating	1 MW
NBI heating	20 MW
ICR heating	8 MW (30 - 120 MHz)
ECR heating	2 MW (140 GHz) 1 MW (105 or 140 GHz)
Major plasma radius	1.65 m
Minor horizontal plasma radius a	0.5 m
Minor vertical plasma radius b	0.8 m
Elongation	1.7
Triangularity (upper/lower)	0.1 / 0.4
Plasma gas	D_2, (H_2, He)
Core density	2 - 10 $\times 10^{19}$ m^{-3}
Core temperature	5 - 20 keV

Table 3.1: Technical data and typical plasma parameters of ASDEX Upgrade

heat the electrons is electron cyclotron resonance heating (ECRH). Heating power in excess of 2 MW is provided by the ECRH system presently consisting of five gyrotrons [43]. They generate microwaves at 140 GHz, which are launched into the plasma via movable mirrors. This allows for very localized electron heating with variable power deposition positions. At present a new ECRH system is under construction. Currently one gyrotron out of four planned gyrotrons is operational. It is able to work at either of two frequencies, 140 and 105 GHz, with a heating power of up to 1 MW. A feature of the new system is a fast steerable launching mirror for feedback-controlled localized power deposition [36]. Another, very efficient way of plasma heating is the injection of a beam of energetic ($70 - 93$ keV) neutral particles into the plasma. These particles heat the plasma by transferring their energy to other particles via collisions. The fast neutrals are generated by a neutral beam injector (NBI). An ion source creates deuterium ions that are accelerated by electric fields and then neutralized through charge exchange reactions with neutral

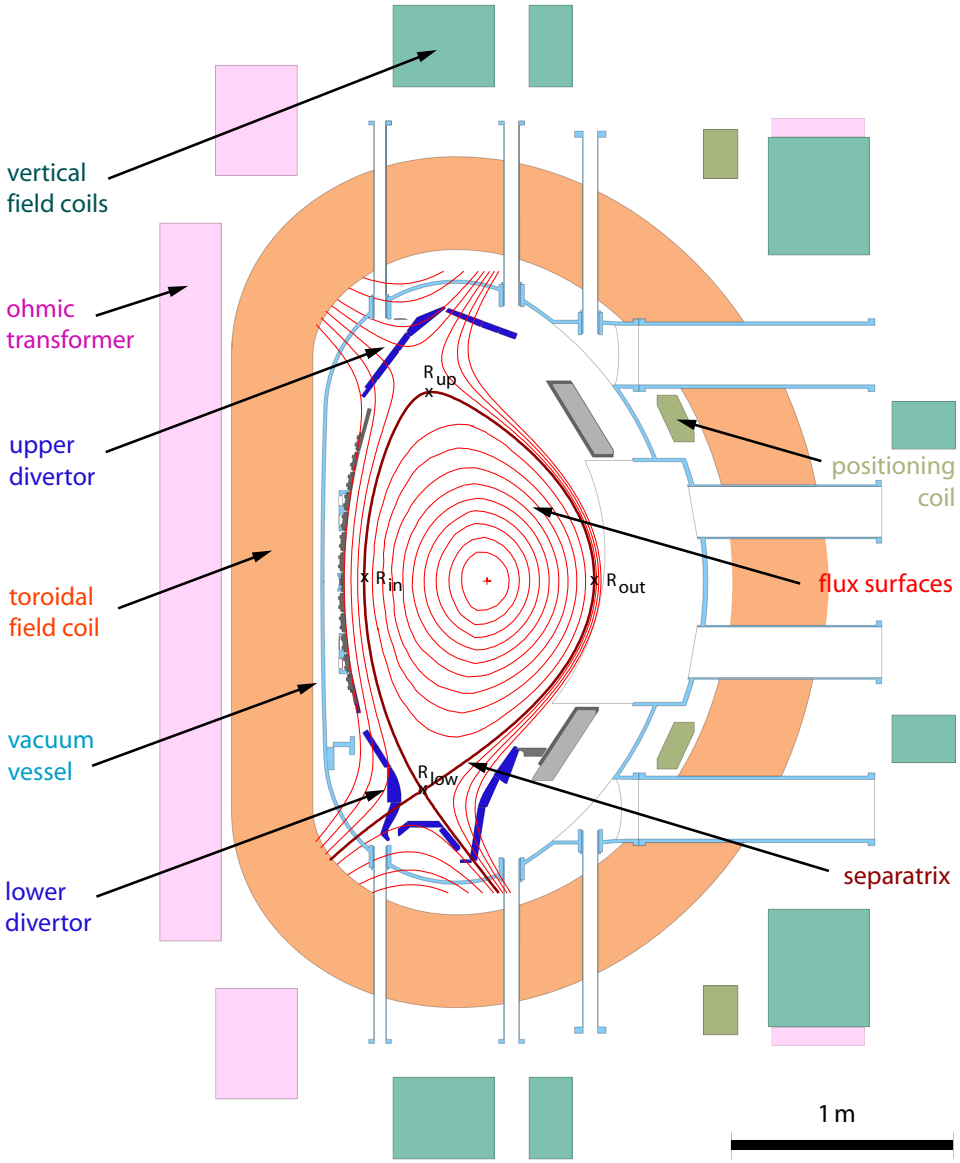

Figure 3.1: Poloidal cross section of the ASDEX Upgrade tokamak with usual LSN plasma configuration.

deuterium gas. Since the fast particles are neutral, they can cross the magnetic field lines and penetrate into the plasma. The NBI system of ASDEX Upgrade consists of two injectors each capable of injecting up to 10 MW (in deuterium) of heating power into the plasma [44, 45]. The neutral beam injection also provides toroidal momentum input that drives the toroidal plasma rotation.

A fusion plasma loses particles continuously, which are removed by the divertor pumping system. There are different methods for refueling the plasma: gas injection, neutral beam injection (NBI) or pellet injection. The gas feeding system comprises

20 valves at different locations in the midplane and the divertor region of the vessel. For pellet fueling solid pellets are produced from frozen deuterium and accelerated in a blower gun or a centrifuge and then injected into the plasma via a guiding system from the low or high field side of the torus.
The plasmas are usually deuterium plasmas with core densities ranging between $2 - 10 \times 10^{19}\,\mathrm{m}^{-3}$ and (ion) temperatures of $5 - 20\,\mathrm{keV}$. In addition to density and temperature a variety of plasma parameters are routinely measured by several diagnostics. ASDEX Upgrade is equipped with an extensive suite of diagnostic systems, which are continually upgraded. The new Doppler reflectometry channel - the basis of this PhD work - is just one example. In the course of this study the analysis of the Doppler reflectometer measurements requires contributions of other diagnostics. In particular the density profile diagnostics are essential. The line integrated electron density is measured by a DCN laser interferometer along five channels using a Mach-Zehnder interferometer [46]. The Thomson light scattering system measures the electron density and temperature profiles using a cluster of six Nd-YAG lasers aligned vertically in the poloidal plane [47]. A measurement of the electron density at the plasma edge is obtained via lithium impact excitation spectroscopy (Li-IXS) [48]. The Li-beam diagnostic also provides ion temperature profiles. Conventional reflectometry [30] gives electron density profiles measured with a $18 - 72\,\mathrm{GHz}$ fast swept O-mode microwave reflectometer [49]. The line emission of excited carbon ions, which originate from charge exchange processes with fast NBI neutrals, is detected by the charge exchange recombination spectroscopy (CXRS) diagnostic [50]. From this measurement toroidal rotation velocity and ion temperature profiles are deduced. The ECE diagnostic measures electron temperature profiles by radiometry of the electron cyclotron emission (ECE) of the plasma [51].

With the introduction of the divertor concept, the spontaneous formation of a transport barrier at the plasma edge was discovered on the ASDEX tokamak in 1982 [52], which is associated with a new plasma state with improved confinement. This plasma regime has been termed the high confinement mode (H-mode) and the plasma state present before the transition to H-mode is called low confinement mode (L-mode) since then. Although it is known that the transition to H-mode occurs when the energy flow across the separatrix exceeds a threshold that depends on the density and magnetic field [53], the exact process of transport barrier formation is not fully resolved yet. In H-mode the pressure gradient steepens at the plasma edge giving rise to the so-called pedestal. The formation of the edge transport barrier is accompanied by a reduction in the level of density fluctuations. Another characteristic of H-mode plasmas are edge localized modes (ELMs). ELMs are repetitive magneto-hydrodynamic (MHD) instabilities, which lead to a fast expulsion of energy and particles from the plasma edge due to a temporary collapse of the transport barrier [54, 55].
ASDEX Upgrade has divertor plates at the top and bottom of the vessel (figure 3.1) that allows for various plasma shapes to be created. The most employed plasma configuration in the experimental program is a lower single null (LSN) plasma with a magnetic X-point above the lower divertor at the bottom of the torus. It is also

possible to form the X-point at the upper divertor plates for an upper single null configuration (USN). Besides the single null shapes also a (near) double null shape may be created with two X-points at the top and bottom divertor respectively. In addition to the position of the X-point, the different plasma shapes are characterized by their upper and lower triangularity $\delta_{u,l} = [\frac{1}{2}(R_{out} + R_{in}) - R_{up,low}]/a$, and their elongation $\kappa = b/a$, where a and b are the minor plasma radii in the horizontal and vertical direction. (The respective major plasma radii (R) are marked in figure 3.1.) Typical values for these quantities are given in table 3.1 for a LSN plasma. The standard discharge configuration has a negative toroidal magnetic field ($-B_{tor}$) and a positive plasma current ($+I_p$), where positive is defined as toroidally counter-clockwise when viewed from above. The positive plasma current creates a poloidal magnetic field directed downwards on the outside of the tokamak. In combination with the negative toroidal field this gives a left-handed helicity of the total magnetic field. For this configuration the NBI induced toroidal plasma rotation is with the plasma current (NBI co-injection).

As the name implies the separatrix separates the bulk plasma from the so-called scrape-off layer (SOL) and forms the last closed flux surface with the x-point. In the plasma SOL the magnetic field lines are 'open' meaning that they are in contact with the vessel walls, whereas inside the seperatrix the field lines are closed in themselves and span the magnetic flux surfaces. The magnetic axis is the center of the nested flux surfaces. One defines a normalized flux surface coordinate, which is constant on a magnetic surface:

$$\rho_{pol} = \sqrt{\frac{\Psi - \Psi_{ma}}{\Psi_{sep} - \Psi_{ma}}} \tag{3.1}$$

where Ψ is the enclosed poloidal magnetic flux and the indexes ma and sep denote the magnetic axis and the separatrix. The poloidal flux radius ρ_{pol} is preferred as radial coordinate for plotting profiles of quantities that are constant on a magnetic surface, like density or temperature. By definition ρ_{pol} equals 0 on the magnetic axis and 1 at the separatrix.

Chapter 4

Doppler reflectometry

4.1 Principle

A Doppler reflectometer is a diagnostic system utilizing both scattering and reflectometry techniques. It combines the wavenumber sensitivity of coherent scattering with the radial localization of reflectometry. Hence, it is a valuable tool for measuring fluctuations at a specific wavenumber and their velocities in a relatively small volume with respect to machine dimensions and compared to traditional forward microwave or laser scattering.

A microwave beam launched into an inhomogeneous plasma will propagate until it reaches a cutoff and is then reflected. For normal incidence the cutoff condition is $N = 0$, where N is the refractive index of the plasma, which is defined as the ratio of the vacuum light speed to the phase velocity $v_{ph} = \frac{\omega}{k}$ of the microwave.

$$N = \frac{c}{v_{ph}} = \frac{ck}{\omega} \tag{4.1}$$

In a plasma the refractive index depends on the microwave frequency ω, the plasma density n_e and the external magnetic field B. For O-mode polarization of the microwaves only the density is relevant, since here the wave electric field vector is parallel to the external magnetic field, whereas for X-mode polarization also the magnetic field influences the wave propagation, since here the electric field vector is perpendicular to the external magnetic field. (The wave vector k is perpendicular to B in both cases). The corresponding cutoff conditions for normal incidence are

$$N^2 = 1 - \frac{\omega_p^2}{\omega^2} = 0 \tag{4.2}$$

for O-mode and

$$N^2 = 1 - \frac{\omega_p^2 \omega^{-2}}{1 \pm \omega_c \omega^{-1}} = 0 \tag{4.3}$$

for X-mode, where $\omega_p^2 = \frac{e^2 n_e}{\varepsilon_0 m_e}$ is the electron plasma frequency and $\omega_c^2 = \frac{eB}{m_e}$ the electron cyclotron frequency (with elementary charge e, electron mass m_e, and vacuum

permittivity ε_0). As N depends on the microwave frequency, various radial positions in the plasma can be probed by changing the frequency of the beam.
By launching the probing beam in oblique incidence with respect to the normal onto the cutoff layer, it is possible to detect the field backscattered off fluctuations along the beam path separately from the field reflected at the cutoff layer [56]. As the wave approaches the cutoff layer its wavelength increases and so does its amplitude as to satisfy energy conservation. This localized swelling of the incident field amplifies the backscattering and allows spatial localization of the scattering process close to the cutoff layer. For coherent microwave scattering on plasma fluctuations the momentum conservation law applies [29, 57].

$$k = k_s - k_i \tag{4.4}$$

k is the wave vector of the scattering fluctuation and $k_{s,i}$ the local scattered and incident wave vector. For a monostatic antenna configuration, where the scattered signal retraces its path back to the launching antenna, the equation reduces to

$$k = -2k_i \tag{4.5}$$

with $k_s = -k_i$.
In slab geometry the incident wavenumber is $k_i = k_0 sin\theta$ and the fluctuation wavenumber is then given by the Bragg condition

$$mk = -k = 2k_0 sin\theta \tag{4.6}$$

where θ is the tilt angle relative to the normal onto the cutoff layer, as shown schematically in figure 4.1. By using a monostatic antenna configuration mainly the scattering order $m = -1$ is detected by the Doppler system. The positive Bragg orders ($m = +1, +2, ...$) are scattered away from the antenna and are generally not seen. Also the strong $m = 0$ reflection used in conventional reflectometry is at least partially suppressed as it is shifted out of the antenna receive pattern as well.

The slab model is a good approximation for the plasma edge region, where the cutoff layers are almost flat. Figure 4.2 a) shows ray traces of microwave beams launched at different angles onto plane cutoff layers [58, 59]. For oblique incidence the reflection at the cutoff occurs at $N^2 = sin^2\theta_0 > 0$, where θ_0 is the incident angle at the plasma boundary, and the fluctuation wavenumber is given by equation 4.6 [60]. Note that the microwave beams experience (strong) refraction, since they do not propagate parallel to ∇N but with an angle. For curved cutoff layers the slab model breaks down and the reflection occurs at a position with $N^2 > sin^2\theta_0 > 0$, where N reaches a minimum. - figure 4.2 b). Hence, beam tracing computation is generally required to determine the radial position of the cutoff layer and the refractive index at the cutoff, particularly in the core region of the plasma, where the curvature of the cutoff layers is significant. The local fluctuation wavenumber k has to be calculated in this case from the refractive index at the cutoff. The microwave wavenumber within the plasma k_i is related to the vacuum wavenumber k_0 by

$$k_i = \frac{\omega}{c} N = k_0 N \tag{4.7}$$

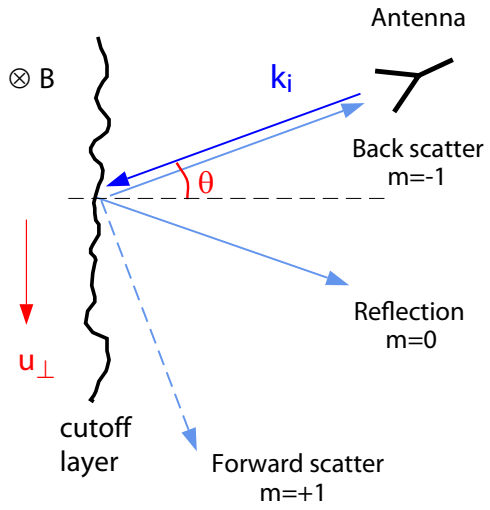

Figure 4.1: Principle of Doppler reflectometry illustrated by a monostatic reflectometer geometry. A microwave beam is launched into the plasma with oblique incidence to the cutoff layer normal. At the cutoff the beam is scattered by plasma fluctuations and gets reflected. The movement of the fluctuations perpendicular to the magnetic field with velocity $u_\perp$ induces a Doppler frequency shift in the backscattered component received by the antenna.

Equation 4.5 can then be written as

$$k = -2k_0 N \tag{4.8}$$

The motion of the fluctuating plasma produces a frequency shift of the backscattered signal due to the Doppler effect. The Doppler shift is given by

$$f_D = \frac{1}{2\pi}\vec{k}\cdot\vec{u} = \frac{1}{2\pi}(k_\perp u_\perp + k_{||}u_{||} + k_r u_r) \tag{4.9}$$

where u is the velocity of the fluctuations. In tokamak plasmas, the perpendicular and parallel wavenumbers of the turbulence are typically very different due to the strong anisotropy induced by the magnetic field. The fluctuations stretch out along the field lines: $k_{||} \ll k_\perp$. Further, $k_r u_r \approx 0$, as the radial wavenumber spectrum is normally centered around zero. That means, that whether the antenna is tilted poloidally and/or toroidally, the Doppler shift results only from the component perpendicular to the magnetic field [56].

$$f_D = \frac{1}{2\pi}k_\perp u_\perp \tag{4.10}$$

Using the Bragg equation, the Doppler shift is given by

$$f_D = \frac{1}{\pi}u_\perp k_0 N \tag{4.11}$$

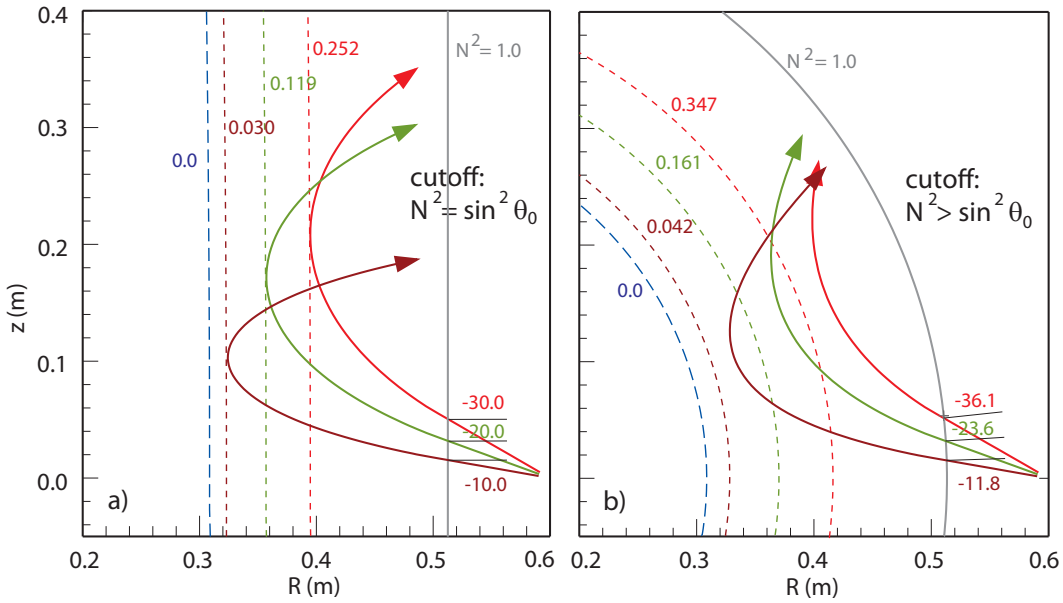

Figure 4.2: Ray traces of O-mode microwave beams launched onto plane (a) and circular (b) cutoff layers with oblique incidence [58]. The dashed lines display N^2 contours. In the slab model the cutoff occurs at $N^2 = sin^2\theta_0$, while for curved cutoff layers reflection occurs at $N^2 > sin^2\theta_0$.

and for slab geometry

$$f_D = \frac{1}{\pi} u_\perp k_0 sin\theta \tag{4.12}$$

The perpendicular velocity of the selected density fluctuations is the sum of two components

$$u_\perp = v_{E\times B} + v_{turb} \tag{4.13}$$

and can be calculated from the measured Doppler shift. v_{turb} is the intrinsic phase velocity of the turbulence riding on the background plasma, which propagates with $v_{E\times B} = v_\perp - v^*$. ($v_\perp$ is the perpendicular fluid velocity (center of mass velocity) and v^* is the diamagnetic drift velocity.) Note that the $E \times B$ velocity is the velocity of the gyrocenters relative to the laboratory frame ($E \neq 0$), whereas v_{turb} is calculated in the plasma frame ($E = 0$).
Generally, linear and nonlinear turbulence simulations show that v_{turb} is in the order of 1 km/s. Since plasma discharges with neutral beam heating typically show strong rotation, $v_{E\times B} \gg v_{turb}$ for the majority of plasma discharges. In this case the perpendicular velocity can be interpreted as the $E \times B$ velocity: $u_\perp \approx v_{E\times B}$. Thus, if v_{turb} is negligible compared to $v_{E\times B}$ (or is known), then the radial electric field can be obtained [31, 56].

$$E_r = -u_\perp B \tag{4.14}$$

Under conditions where v_{turb} is comparable or greater than the $E \times B$ velocity ($v_{E\times B} \leq v_{turb}$) the turbulence phase velocity behavior can be studied [61]. Since fluctuations of the radial electric field directly translate to fluctuations in the $E \times B$ velocity and hence to fluctuations in the measured Doppler shift, long wavelength E_r oscillations such as GAMs and zonal flows can be investigated using Doppler reflectometry [62]. The diagnostic technique can be extended by adding a second channel launching a slightly different frequency to measure instantaneous E_r shear rates and radial turbulence correlation lengths [63, 64]. Doppler reflectometry is sensitive to a specific fluctuation wavenumber $k_\perp$ that scatters the incident beam and is selected by the antenna tilt angle according to the Bragg condition. Since the backscattered signal intensity is determined by the fluctuation amplitude at the probed $k_\perp$, it is possible to measure the turbulence wavenumber spectrum by scanning the tilt angle [65, 35].

4.2 Hardware

The current Doppler reflectometry system installed on ASDEX Upgrade consists of three channels: two V-band ($50-75$ GHz) channels and a new W-band ($75-110$ GHz) channel. Both V-band systems are composed of identical reflectometer units and microwave antennas with fixed lines of sight. With these channels measurements are mostly restricted to the edge and scrape off layer. The core is only accessible for low density plasmas. In addition, the probed wavenumbers are set to a small range by the fixed antenna tilts. Therefore, a third channel consisting of a W-band reflectometer and a steerable antenna was added to upgrade the Doppler system. The new reflectometer unit extends the radial coverage into the core. Figure 4.3 shows the cutoff frequencies (normal incidence) for O- and X-mode polarization at the plasma midplane for a particular density and magnetic field and the corresponding radial access regions of the V and the W frequency band. The W-band reflectometer was built as part of this PhD work. The new antenna has a variable line of sight to allow for dynamic wavenumber selection.
Each of the three reflectometer units has two components: the actual reflectometer (section 4.2.1) and the control and data acquisition module (section 4.2.2). The antennas and transmission lines are described in section 4.2.3.

4.2.1 Reflectometer

Basic reflectometer circuit
The rotation of the plasma introduces a Doppler shift f_D of the backscattered microwave with respect to the transmitted wave (see section 3.1). In order to be able to measure the sign of the Doppler shift and hence the direction of the plasma rotation a heterodyne circuit with IQ detection is used - figure 4.4. To achieve heterodyne detection, the transmitter (RF) and the local oscillator (LO) are set to slightly different frequencies (f and $f + \Delta f$). The corresponding intermediate frequency (IF) signal (Δf) obtained by mixing the oscillator output frequencies can be used as a reference signal for the IQ detector circuit. The backscattered signal

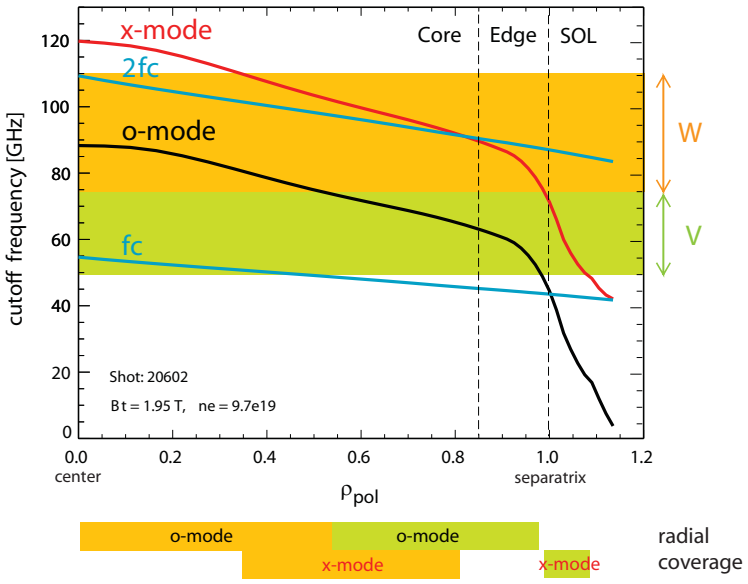

Figure 4.3: Radial access regions of the V and W frequency bands for particular density and magnetic field. Plotted are the cutoff frequencies (normal incidence) for O- and X-mode polarization at the plasma midplane.

from the plasma ($f + f_D$) is mixed with the local oscillator signal. As a result, the down-converted signal appears at a non-zero frequency ($\Delta f + f_D$) and is shifted out of the inherent 1/f noise of the mixer, thus improving the dynamic range of the receiver. The IQ detector mixes the IF signal with the stable reference signal to obtain the in-phase component $I = A \cdot \cos\phi$. Here, A is the amplitude and ϕ the phase of the IF signal. By shifting the reference signal by 90° and mixing it with the IF signal, also the quadrature component $Q = A \cdot \sin\phi$ is generated by the IQ detector.

A received signal without Doppler frequency shift appears after the mixer at the intermediate frequency Δf and after the IQ detector at zero frequency. An up-shifted (down-shifted) signal appears at frequencies above (below) Δf after the first mixing stage and at a finite frequency $\pm f_D$ after IQ detection. The phase of the Q signal is then leading (lagging behind) the I signal. As a consequence of plasma turbulence, a complicated amplitude and phase modulation appears on the received signal in addition to the underlying Doppler shift. Owing to IQ detection the system additionally provides amplitude $A = \sqrt{I^2 + Q^2}$ and phase $\phi = \arctan(Q/I)$ information.

W-band reflectometer

A schematic of the W-band reflectometer module is shown in figure 4.5. Here, microwave and waveguide components are displayed in blue, while radio frequency (RF) and electronic components are colored green and black respectively. Two voltage controlled 'hyper-abrupt varactor tuned oscillators' (HTOs) are used as

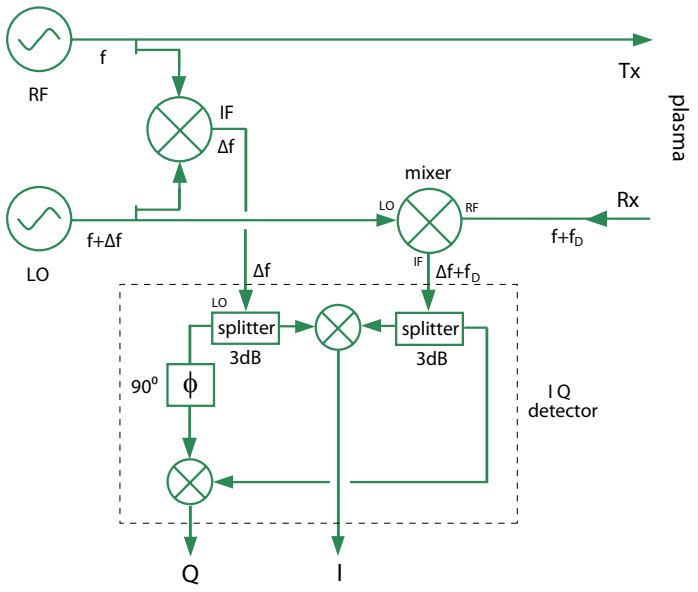

Figure 4.4: Basic heterodyne reflectometer circuit with IQ detection.

basis transmitter and local oscillator. The output frequency of the HTOs can be varied between 12 GHz and 18 GHz by applying a control voltage (V_1, V_2). The fixed frequency difference of 150 MHz between the two HTOs is maintained by a 'phase locked loop' (PLL). In contrast to the V-band reflectometers, where the transmitter source is a free running oscillator, the new W-band reflectometer has a PLL frequency synthesizer (for details see below). Whereas a free running HTO is subject to frequency drifts due to temperature changes, a phase locked synthesizer guarantees excellent frequency stability despite the intrinsic warming-up of the reflectometer after switch-on (up to 3 hours) plus the variations in the torus hall temperature during an operation day. The frequency stable transmitter is a requirement for the precise determination of the diagnostic frequency response needed for the analysis of the received scattered power. The synthesizer and local oscillator (LO) frequencies ($12 - 18$ GHz) are brought up to the W-band range ($72 - 108$ GHz) by active frequency multipliers ($\times 6$) and power amplifiers. In order to prevent damage of the device by spurious reflected power the synthesizer output is connected to the transmitter waveguide via a ferrite isolator, which is protected from stray magnetic fields by an iron sleeve. The launched microwave power after the isolator is typically 10.5 dBm = 11 mW across the band.

The received signal is down converted to an intermediate frequency of 900 MHz $\pm f_D$ by a fundamental waveguide mixer, which is driven by the hextupled local oscillator output. The power of the IF signal strongly depends on the launched microwave frequency. The measured instrument frequency response is shown in figure 4.6. The response function was obtained by connecting the transmitter straight to the receiver via fundamental waveguide and an attenuator. The power variation of the

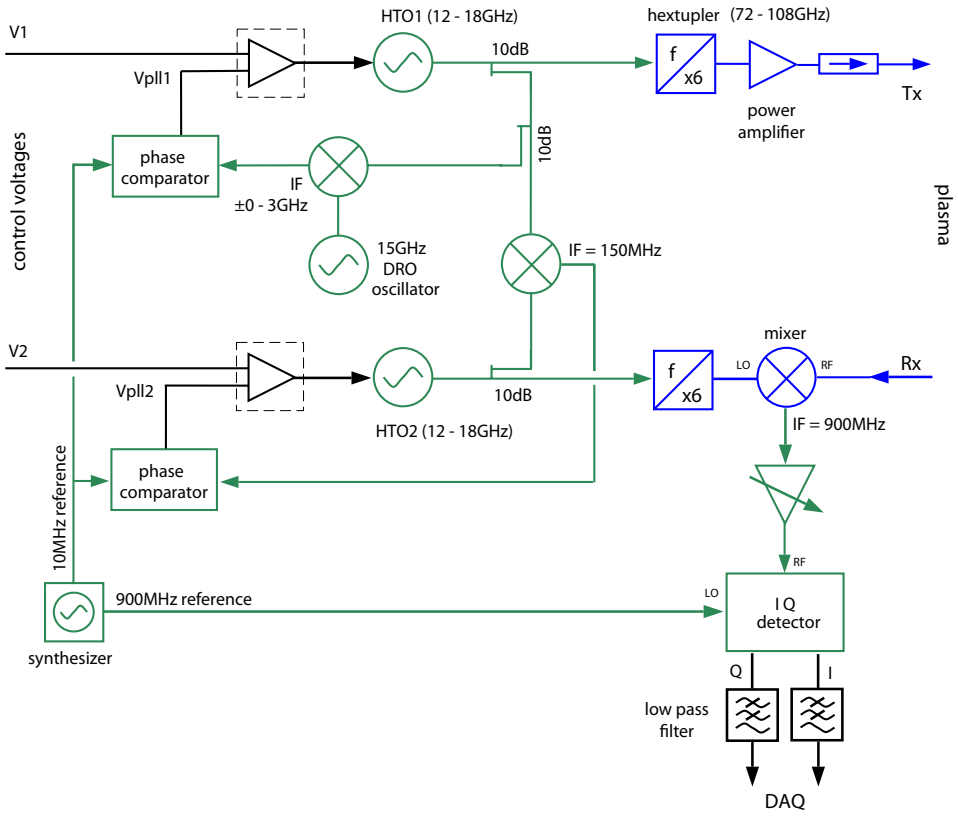

Figure 4.5: Basic circuit diagram of the heterodyne W-band (72 – 108 GHz) Doppler reflectometer.

IF signal across the band is about 30 dB, which is a combination of variations in the transmitter power and the receiver response. Here, the need for a synthesizer as transmitter source becomes evident, since a small frequency change due to temperature drift could result in a significant (unknown) change of the IF signal power. To compensate for the power variation, the IF signal is amplified (or attenuated if necessary) by a variable gain amplifier with a gain range of ±30 dB. In the second mixing stage the signal components in phase (I) and in quadrature (Q) to the carrier are determined. The reference frequency (LO) for the IQ detector is provided by a commercial 900 MHz-synthesizer. The I and Q video signals are analog filtered to prevent aliasing before they are digitized in the data acquisition unit. The cutoff frequency of the low-pass filter is 7 MHz, which is sufficiently above measured Doppler shifts (typically, $f_D < 5$ MHz).
Figure 4.7 shows a photograph of the reflectometer module. The reflectometer is housed in a RF-shielded 3 HE 19-inch rack-mount unit with partitions for microwave transmitter (bottom left), microwave receiver (top left), and electronic components (right).

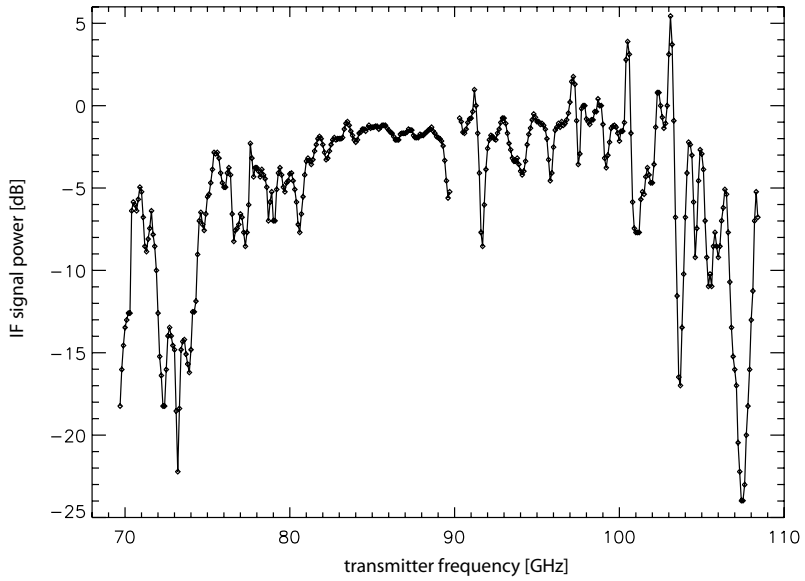

Figure 4.6: Instrument frequency response. The plot shows the 900 MHz IF signal power versus transmitter frequency.

Phase locked loop circuits

The W-band reflectometer employs a frequency synthesizer as transmitter source. Since the synthesizer was the most challenging reflectometer component and hence the most time consuming device in the development phase of the diagnostic, the circuit is described here in detail.

The transmitter frequency is stabilized by a 'phase locked loop' (PLL). A detailed schematic of the implemented synthesizer design is shown in figure 4.8. A PLL is a feedback system, where a 'phase/frequency detector' (PFD) compares the down converted oscillator output with a stable reference frequency. The PFD produces an output proportional to the phase and frequency difference between the two sources that is used to stabilize the output frequency of the oscillator.

Most commercial PLL frequency synthesizers are designed for wireless applications and are narrow band in nature. These applications include wireless standards like GSM (Global System for Mobile Communications), where the total tuning range for the oscillator is less than 100 MHz. There are also wideband applications for which the oscillator could have a tuning range as wide as an octave. For example, cable TV tuners have a total range of about 400 MHz [66]. Going from a narrow band to a wideband PLL is challenging since the stability of the loop strongly depends on various loop elements, whose properties/values change significantly with the oscillator frequency. Especially the non-linear tuning sensitivity of the HTO is highly problematic in this context. Consequently, designing a stable PLL with a ultra-wide tuning range results in degradation of other loop qualities.

Because of the commercial availability of frequency synthesizers for wireless standards a GSM900 PLL Synthesizer from Analog Devices [66] is used as a basic

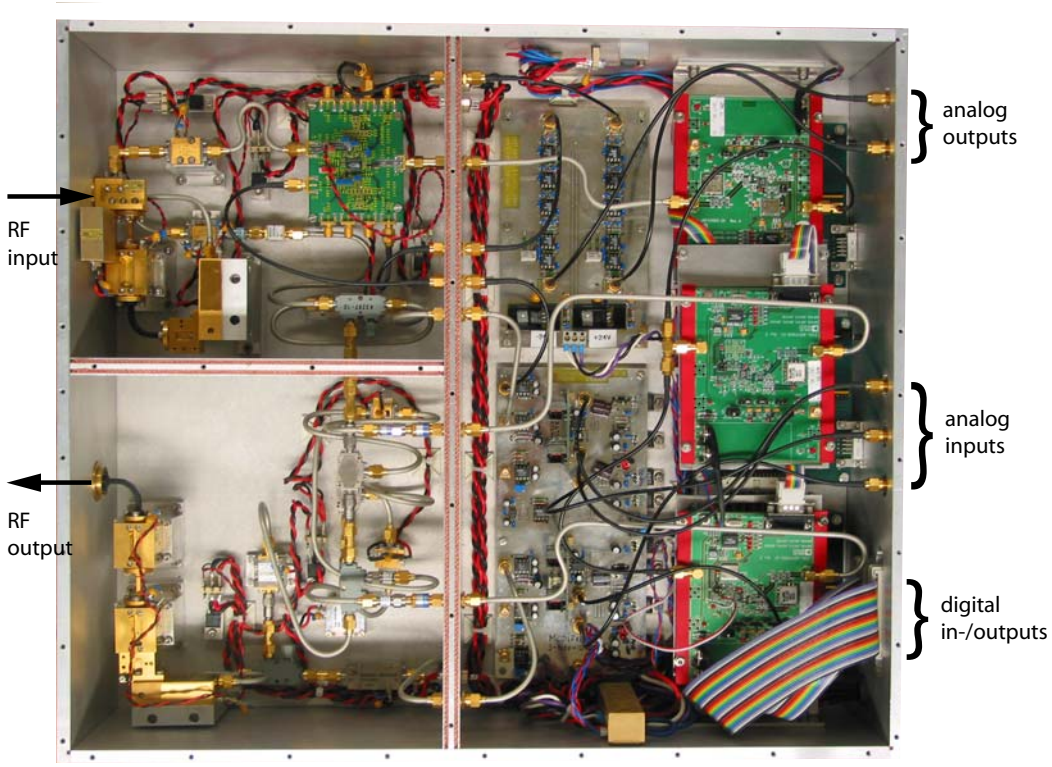

Figure 4.7: Top view of the W-band Doppler reflectometer (lid removed).

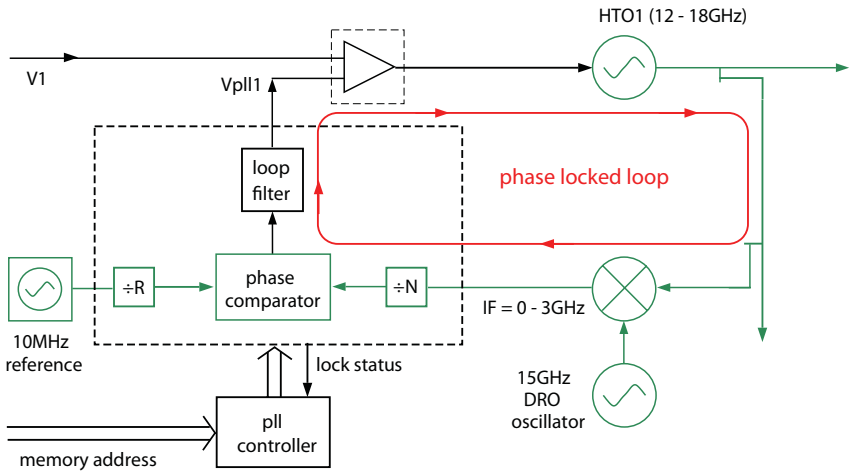

Figure 4.8: Schematic of the frequency synthesizer for the W-band Doppler reflectometer. A phase locked loop (PLL) circuit is used for frequency control.

circuit. The original tuning range of the synthesizer is $819 - 915\,\mathrm{MHz}$. However, for the desired microwave synthesizer this range needs to be extended to about $0 - 3000\,\mathrm{MHz}$. To achieve such a wideband loop, major changes to the original PLL architecture are necessary.
Using a 10 dB directional coupler in the transmission line of the $12 - 18\,\mathrm{GHz}$ HTO a fraction of the output signal is sampled. Mixing the signal with 15 GHz from a stable 'Dielectric Resonator Oscillator' (DRO) yields a down-converted signal with an intermediate frequency (IF) of $0 - 3\,\mathrm{GHz}$.
The PFD frequency (f_{PFD}) determines how frequently the phase/frequency detector compares the input signal with the reference signal. Thus, a high PFD frequency would be desirable to improve the PLL performance. The used PFD is able to work at PFD frequencies up to 55 MHz. Hence, the input signal ($0 - 3\,\mathrm{GHz}$) is divided down to f_{PFD} by a programmable feedback divider (N). For every frequency of the intermediate signal (f_{IF}) the division factor N is set such that $f_{IF}/\mathrm{N} = f_{PFD}$, with N being an integer. This means that stabilized intermediate frequencies are multiples of the PFD frequency: $f_{IF} = \mathrm{N} \cdot f_{PFD}$. As a consequence, the frequency gap between two adjacent stabilized frequencies is determined by f_{PFD} and therefore a low PFD frequency would be desirable. For this synthesizer a f_{PFD} of 2 MHz was chosen as the best compromise. The reference frequency (10 MHz) supplied by a stable quartz crystal oscillator is reduced in an analogous way by the reference divider (R) for comparison with the scaled feedback frequency at the digital phase/frequency detector. The output of the PFD are current pulses that are filtered and integrated (loop filter) to generate a voltage (V_{pll}) between 0 V and 5 V. This control voltage is not enough to drive the voltage-controlled oscillator, which needs a tune voltage ranging from 3 V (12 GHz) to 17 V (18 GHz). Therefore, an external tune voltage is applied that is a simple DC offset added to the control voltage of the PLL by a summing amplifier. The resulting voltage drives the HTO to increase or decrease its output frequency so as to push the average output of the PFD towards a constant value. The two frequencies are then equal and phase locked. In this way a stable HTO output frequency signal ($12 - 18\,\mathrm{GHz}$) is synthesized from a fixed low-frequency reference signal (10 MHz). The possible discrete synthesizer frequencies are $f_{HTO} = \pm(\mathrm{N} \cdot f_{PFD}) + 15\,\mathrm{GHz}$, with N being an integer.
Since f_{PFD} is a preset constant, a variation in the HTO output frequency requires a changing divider value. Accordingly, for frequency hopping the N divider needs to be reprogrammed for every new frequency step. Here, this is performed by a custom-made PLL controller board. The on-board memory chip has stored N divider settings for various synthesizer frequencies. In the data acquisition and control software of the diagnostic the desired frequencies are related to corresponding memory addresses, that are transfered to the PLL controller. Besides changing the N divider value, the controller is also programming PFD settings like current output and polarity. For HTO frequencies $12 - 15\,\mathrm{GHz}$ the polarity is positive and correspondingly negative for $15 - 18\,\mathrm{GHz}$. The PFD's current output is an important PLL setting and needs to be adjusted to ensure loop stability for the wide range of synthesizer frequencies. In addition to its programming function the controller receives information on the lock status of the PLL.

As mentioned earlier, the design of a wideband PLL is demanding and in order to have a very wide tuning range one has to tolerate degradation of other loop qualities. The major performance parameters to be considered in a PLL are: phase noise, reference spurs, and locking time. Reference spurs are artifacts at discrete offset frequencies from the carrier frequency (IF signal) that are generated by the operation of the PFD at f_{PFD}. In this synthesizer circuit the reference spurs are eliminated by a notch filter that follows the loop filter. The locking time of a PLL is the time it takes to jump from one specified frequency to another specified frequency. For frequency hopping experiments a typical pattern has about $15 - 25$ frequency steps in 100 ms. Therefore, a short locking time is essential. Here, the locking time is less than $100\,\mu$s. When optimizing the PLL for wide tuning range the trade-off is that the performance regarding phase noise and the capture range of the synthesizer are degraded. The capture range is the frequency range in which the PLL acquires lock. In this application the capture range is restricted a priori by using the PLL control voltage only as a correcting term to the externally applied tuning voltage and not as a direct voltage supply as is common practice for standard PLLs [67]. For low frequency IF signals the absolute capture range is about 4 MHz, increasing up to about 17.5 MHz for higher frequencies. However, the limited capture range is not a real drawback, since a pre-discharge calibration of the external tuning voltage ensures that the down-converted HTO frequency is in the capture range of the loop. Figure 4.9 a) shows the frequency spectra of the free running HTO (yellow signal) and the phase locked HTO (red signal) for comparison. Both spectra show the down converted HTO output - the IF signal. The phase noise of the free running oscillator (i.e. the spectral width of the peak) is substantial, whereas for the phase locked oscillator the phase noise is greatly reduced and the signal amplitude is increased by ≈ 15 dB. Generally, the side bands are down by at least 25 dBc for high intermediate frequencies. For small frequencies this value increases up to 35 dBc. Besides phase noise reduction, frequency stabilization is another important advantage of the synthesizer. The frequency of the free running HTO is not stable, but shifting with time. In contrast, the synthesizer output has a specific frequency that is kept fixed by the PLL action. In this example the PLL is programmed to give a IF-spectrum peaking at exactly 1.0 GHz. (Note that the red spectrum is shifted by -50 kHz for clarity.)
Figure 4.9 b) shows the frequency spectra of the 10 MHz reference signal from the quartz crystal oscillator. For both plots the ratio of frequency span to center frequency is fixed (0.0005) to allow a fair comparison of the spectra. The figure shows that the relative carrier width of the PLL spectra (red) corresponds to the carrier width of the reference spectra (brown).

In addition to the synthesizer PLL, a second PLL is used in the reflectometer circuit to maintain the fixed frequency difference (150 MHz) between the transmitter HTO and the local oscillator. This loop is working analog to the synthesizer PLL, but with the major difference that it is not a wideband but a fixed frequency PLL. The IF signal results from mixing the two oscillator outputs. Here, the synthesizer HTO serves as the stable reference for down-conversion. For this PLL the locking

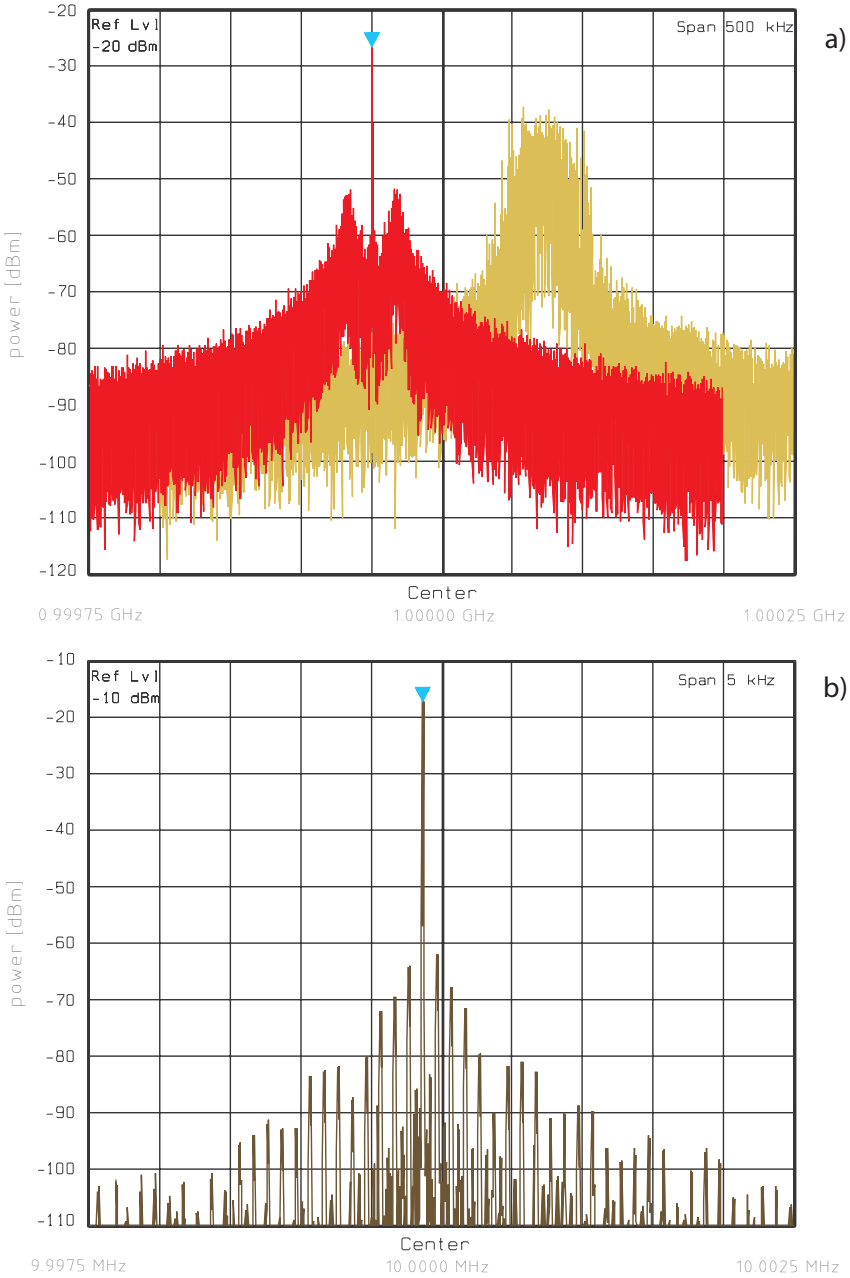

Figure 4.9: (a) Frequency spectra of the free running HTO (yellow) and the phase locked HTO (red). Both spectra show the down-converted HTO output. Note that the red spectrum is shifted by $-50\,\mathrm{kHz}$ for clarity. It peaks at exactly $1\,\mathrm{GHz}$ as expected and shows reduced phase noise compared to the spectra of the unstable free running oscillator. (b) Frequency spectra of the $10\,\mathrm{MHz}$ reference signal from a quartz crystal oscillator. Note the different scales.

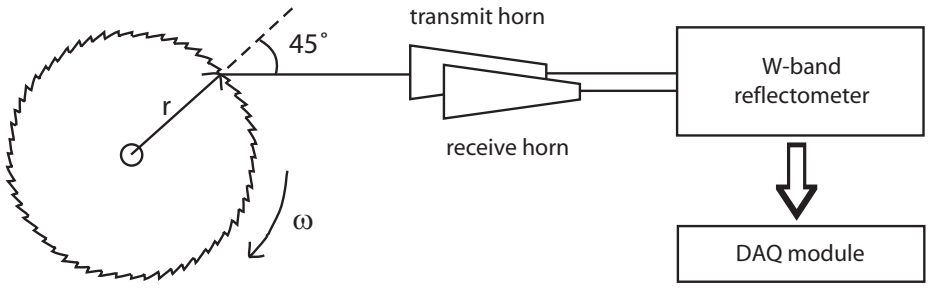

Figure 4.10: Schematic of experimental setup for testing the functionality of the new W-band reflectometer. The perturbed plasma cutoff is simulated by a rotating metal cylinder with a surface grating.

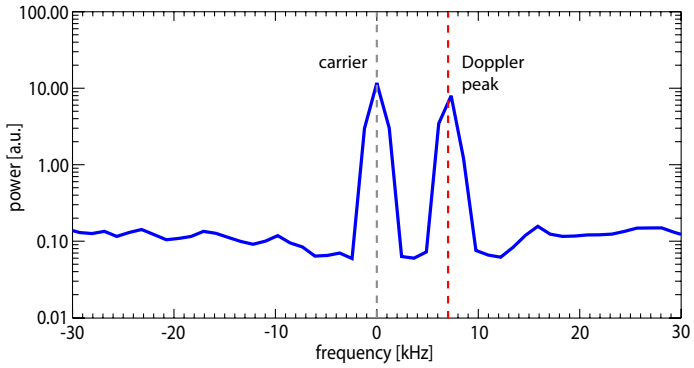

Figure 4.11: Frequency spectrum obtained by simulating the perturbed plasma with a rotating reflection grating. A clearly resolved Doppler peak is present at the expected frequency of 7 kHz.

time is less than 180 μs (locking time of synthesizer PLL + 80 μs) and the capture range is 25 MHz. The phase noise is greatly reduced - the remaining side bands are down by 40 dBc.

Functionality test

The performance of the reflectometer was tested in the laboratory using a rotating metal cylinder with a surface grating (from IPF Stuttgart) to simulate the movement of a perturbed plasma cutoff. The microwaves were launched onto the reflection grating with a tilt angle of $\theta \approx 45°$ (figure 4.10). The probing frequency was 82 GHz and the rotation speed of the cylinder was $v = \omega r \approx 17\,\mathrm{m/s}$. For these settings a Doppler shift of about 7 kHz is expected. The reflectometer was connected to the full control and data acquisition setup (see section 4.2.2). The measured frequency spectrum is shown in figure 4.11, where a clearly resolved Doppler shift is found at the expected frequency and the direct reflection peak at 0 kHz. This result confirms the proper functionality of the W-band reflectometer plus the ability to resolve Doppler shifts down to a few kHz.

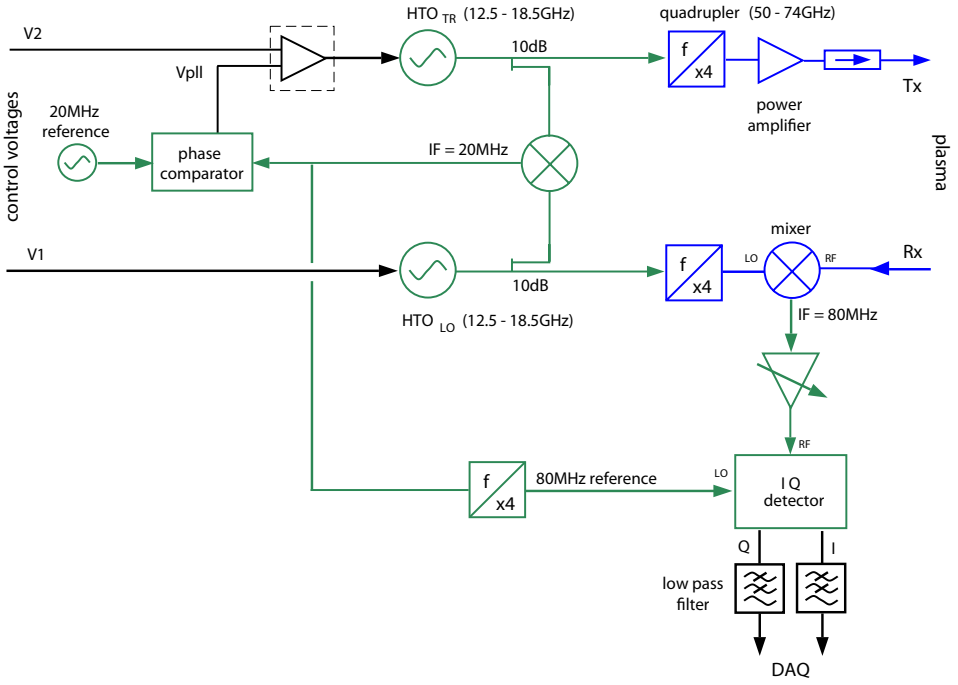

Figure 4.12: Circuit diagram of the heterodyne V-band ($50 - 74\,\mathrm{GHz}$) Doppler reflectometer.

V-band reflectometer

The reflectometer design of the two V-band units is slightly different from new W-band unit. A schematic of the V-band reflectometer is shown in figure 4.12.
The major difference to the new unit is the microwave transmitter. Instead of having a frequency synthesizer the source is a free running oscillator. The frequency difference of the two HTOs - here $20\,\mathrm{MHz}$ - is controlled by a PLL similar to the fixed frequency loop of the new reflectometer except that the transmitter is matched to the local oscillator and not vice versa. The performance of the PLLs is also comparable. For the V-band reflectometer the capture range of the PLL is $26\,\mathrm{MHz}$ and the loop acquires frequency lock in typically $1\,\mathrm{ms}$. Sidebands and spurious effects are down by $40\,\mathrm{dB}$. In order to bring the launch and local oscillator frequencies up to the V-band range ($50 - 74\,\mathrm{GHz}$), active frequency quadruplers are used. The inputs to the IQ detector are the quadrupled $20\,\mathrm{MHz}$ signal of the phase locked loop, which is the reference signal ($80\,\mathrm{MHz}$), and the amplified IF signal of the waveguide mixer, which is $80\,\mathrm{MHz} \pm f_D$. A more complete description of the V-band system is given by Klenge [68].

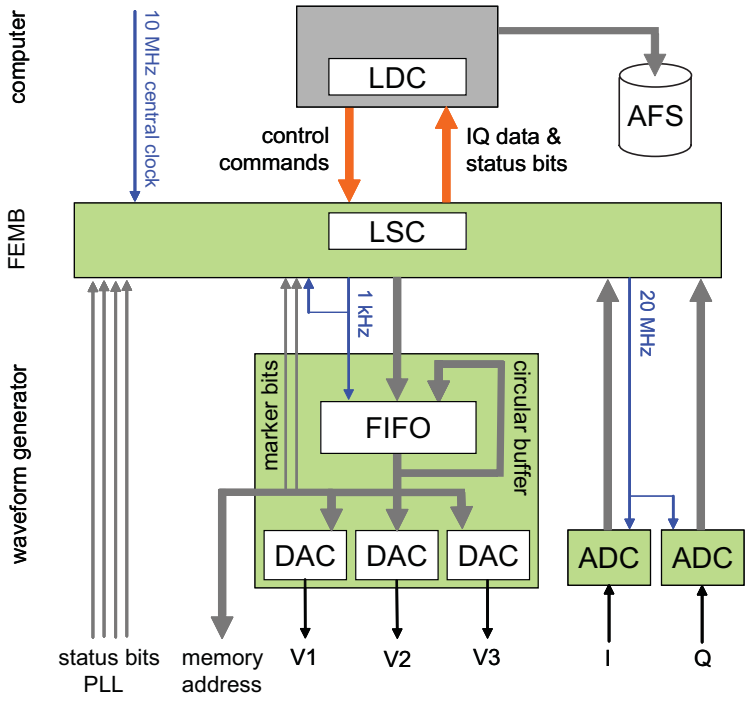

Figure 4.13: Block diagram of the control and data acquisition for the W-band Doppler reflectometer.

4.2.2 Control and data acquisition

Electrically isolated data transfer from the experiment to the control room and computer room is required for safety reasons due to the possible occurrence of overvoltage events in the torus hall. Hence, a data acquisition system based on the CERN S-Link ('smart link' [69]) is implemented allowing for fast data transfer via fiber-optic links. The S-link consist of a 'link source card' (LSC) and a corresponding 'link destination card' (LDC). The LDC is mounted on the 'read-out motherboard' (ROMB) of a Linux PC that acts as the diagnostic controller. Accordingly, the link counterpart to the LDC, the LSC, is mounted on a custom 'front-end motherboard' (FEMB) (see [70] for details) integrated in the control and data acquisition module of the reflectometer. The block diagram, figure 4.13, illustrates the operation of the module. As the name implies it is used for both, system control and data acquisition.

A waveform generator produces the control outputs needed to operate the reflectometer. It generates three different analog voltages (V_1, V_2, V_3) to control the frequency of the two oscillators and the variable gain of the amplifier. In addition, it provides an address code specifying the synthesizer frequency, that is accepted by the PLL controller board. For frequency hopping operation of the reflectometer a pattern is programmed containing the frequency steps and gain settings. Before a plasma pulse is started the pattern is sent by the control computer and loaded

into 'first in first out' (FIFO) buffers of the waveform generator via shift registers. The data acquisition is initiated by a trigger signal (TS06) from the central timer system of ASDEX Upgrade indicating the start of a pulse. During the pulse the FIFOs are read out cyclically using the 1 kHz clock signal generated on the FEMB. Hence, frequency steps can be programmed in 1 ms time intervals or any longer multiple time periods. Three 12-bit digital-to-analog converters (DACs) produce the three different analog control voltages. The remaining 12 bits of the 48-bit FIFO data-word represent the address code configuring the PLL settings for the synthesizer. The two least significant bits of the 12-bit word actually controlling the gain setting are used as markers for data analysis and are passed to the FEMB for data acquisition. One of these bits is indicating the beginning of a new frequency step and the other denotes the start of the whole (repetitive) frequency pattern.
The I and Q video signals are digitized with 12-bit resolution and a sampling rate of 20 MHz using pipelined analog-to-digital converters (ADCs). The acquisition clock is generated on the FEMB from the master clock, which is also generated on the board by a PLL frequency multiplier from either an external 10 MHz clock reference or on-board quartz oscillator. The external 10 MHz clock is provided by the central timing system of ASDEX Upgrade and should be used as reference for the data acquisition during plasma discharges. However, due to insufficient signal amplitude (minimum 3 V_{pp} required) of the external clock the internal reference source is used at present.
The ADC digital outputs are directly connected to the FEMB, which provides buffer memory for the data stream. The 32-bit data words send to the control computer via S-link contain 2× 12-bit digitized I and Q data and 8-bit status information on PLL lock states (2 bits), PLL feedback control voltage (2 bits), and timing (4 bits). The collected data result in typically 800 MB raw data per pulse corresponding to a pulse length of 7 s. The amount of raw data that can be stored is limited only by the size of allocated buffer in the control computer. While data acquisition is done during the plasma pulse, data archiving and processing is postponed until after the pulse. After reducing the data volume by lossless Huffmann compression [71], the raw data files are stored on the multiple resident AFS ('andrew file system' [72]) of ASDEX Upgrade. The Linux computer itself is controlled remotely by a network computer via an MDSplus [73] client/server architecture.

The hardware (waveform generator) and software for controlling the new reflectometer were extended from the previously existing V-band system to maintain a degree of compatibility and modularity. However, there are several major increments mainly in the software to handle the control of the frequency synthesizer. This includes creating and sending of the address code and collecting and processing the status bits of the synthesizer PLL. Altogether there are four PLL status bits - two for each PLL of the reflectometer. One bit is the lock bit, indicating the lock state of the loop, and the other bit indicates whether the feedback control voltage is above or below its optimal value. These status bits are used to perform a pre-pulse-calibration of the oscillator control voltages for each probing microwave frequency. This is done to ensure that both HTO frequencies lie in the capture range of the

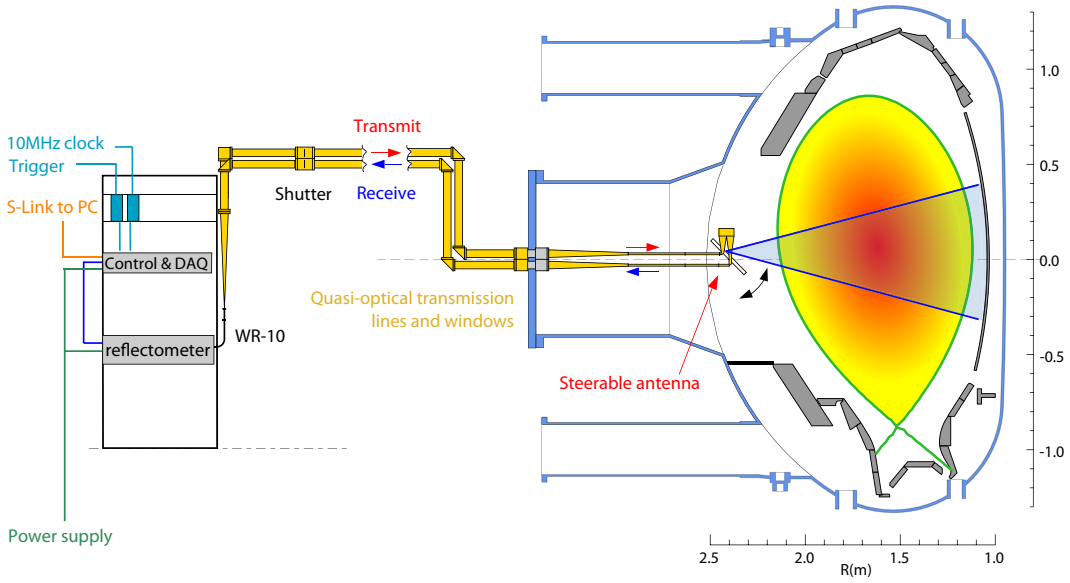

Figure 4.14: Schematic of the new Doppler diagnostic setup in sector 05 of ASDEX Upgrade. The W-band reflectometer is connected to the steerable in-vessel antenna via quasi-optical transmission lines.

respective PLL, in spite of possible frequency drifts due to temperature variations over the day.

4.2.3 Transmission lines and antennas

The reflectometers are located together with the control and data acquisition modules close to the ASDEX Upgrade vessel.

W-band system

The W-band system is located in torus sector 05 of the tokamak and is sketched in figure 4.14. The reflectometer is connected to the antenna via quasi optical transmission lines starting with fundamental rectangular waveguides (WR-10) connected to the output/input waveguide flanges of the reflectometer. The waveguide path is designed to allow for both O-mode and X-mode polarization using oversized circular and square waveguides. The polarization selection (O- or X-mode) is made with waveguide twists in the fundamental waveguide. The microwaves are launched in X-mode since this polarization yields good radial coverage for typical densities and magnetic fields of ASDEX Upgrade plasmas and W-band frequencies (figure 4.3). The transition from fundamental to 39 mm inner diameter circular waveguide is made by linear tapers which are 50 cm in length. Using oversized waveguides minimizes the power losses in the transmission lines. Since the waveguide system is required to transmit W-band and at a later stage also V-band frequencies, smooth bore waveguides are employed. Due to limitations in space several mitre bends in

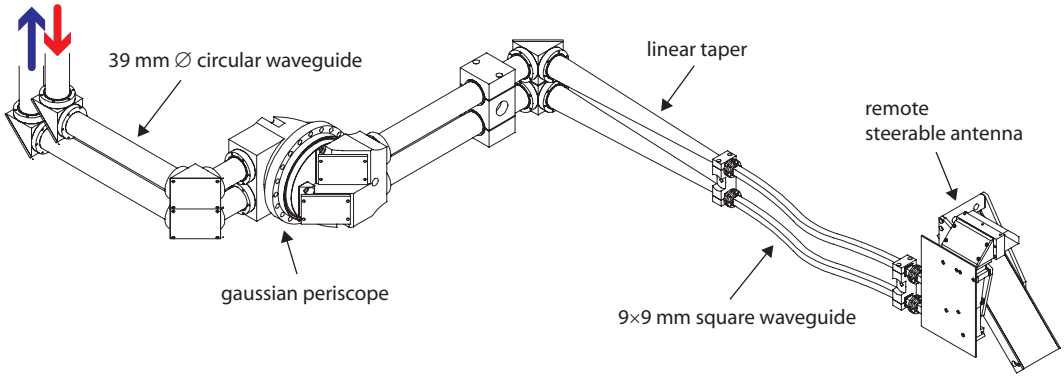

Figure 4.15: CAD drawing of waveguide route showing vacuum break, waveguide assembly and steerable antenna.

the waveguide path are needed to change the direction. However, they add to the signal loss. Each mitre bend degrades the power by about 0.5 dB. A section of the in-vessel waveguide assembly plus the Doppler antenna can be seen in figure 4.15. The figure also shows the vacuum feedthrough - a Gaussian periscope with tilted quartz windows. The periscope has elliptic focusing mirrors and macor (glass ceramics) inserts. The vacuum break causes about 3-4 dB power loss. Inside the vessel the circular waveguide is tapered down to 9×9 mm square waveguide in order to avoid collision with the ECRH launchers, that are positioned right next to the Doppler antenna. A symmetric waveguide bend is also necessary to pass the port edge. The linear tapers also contribute to the power loss. Each one causes about 0.5 dB loss. Overall, the single pass loss of the waveguide assembly in the W-band frequency range (75 GHz – 110 GHz) is less than 6 dB at 72 GHz and less than 8 dB at 105 GHz.

The new in-vessel antenna is positioned on the low field side close to the mid-plane. Its line of sight is variable, which allows for scanning the turbulence wavenumber at constant plasma conditions by changing the tilt angle. The separate launch and receive antennas sit right next to each other and are connected to the square waveguides (figure 4.15). Both are folded hog-horn antennas with parabolic focusing mirrors and an aperture of 30×30 mm. The horns are wire-etched from solid oxygen-free high conductivity (OFHC) copper and gold plated - like all other waveguide components. A common flat steerable mirror for the transmit and receive antenna can be controlled remotely between plasma discharges via a mechanical steering linkage. Figure 4.16 shows the antenna design in detail. The various lines of sight result from the orientation of the steering mirror. The achievable poloidal angles span the range of $-13.8°$ to $+15.5°$ relative to the horizontal depending on the inclination of the mirror. This is illustrated in figure 4.17 (left side). The poloidal lines of sights are not exactly aligned with the radial direction but have also a toroidal angle of $6.12°$, thus pointing slightly into the direction of sector 04. This small toroidal tilt is not intentional but resulted from installation constraints.

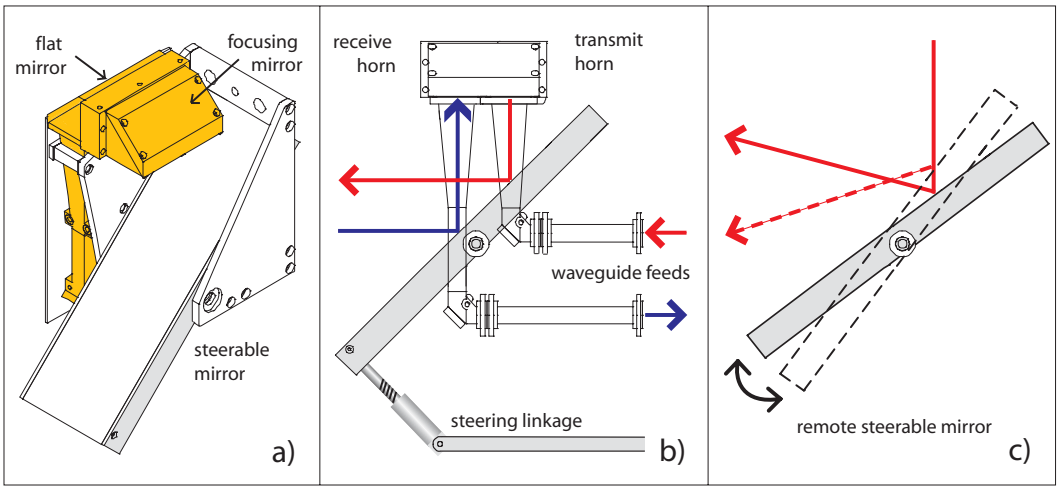

Figure 4.16: Drawings of the steerable antenna. (a) CAD drawing of folded hog-horn antennas (yellow) with flat and parabolic focusing mirrors. (b) Schematic side view of the antenna assembly showing transmit and receive horn and mirror steering linkage. (c) Flat steerable mirror. Different lines of sight result from the adjustable position of the mirror.

The far-field beam divergence of the antenna is 5.5° FWHH (full width half hight) at 105 GHz in the toroidal plane for both orientations of the wave electric field. In the poloidal plane we found 5.2° FWHH and 6.8° FWHH for the two electric field orientations, respectively. Figure 4.18 shows the corresponding square law detector measurements of the radiation patterns. The detector was positioned at a distance of $> 63\,\mathrm{cm}$ from the antenna in the far field region. The side lobes are down by $-15\,\mathrm{dB}$ at $\pm 17°$ in the toroidal plane. The antenna gain is about 30 dB.
Since the ECRH launchers are installed right next to the steerable antenna, RF-pick-up at 105 GHz and 140 GHz is unavoidable and could damage the receiver part of the reflectometer. In order to protect the reflectometer from high power ECRH stray radiation, remote controlled waveguide shutters are installed in the transmit and receive path. Test measurements using a diode detector revealed a radiation power of 3.2 mW in the receiver waveguide during ECRH pulses when operating the new gyrotron system (1 MW). The receiver of the reflectometer can tolerate a RF input power level of 5 mW abs. max. Nevertheless caution is necessary, since the power level in the waveguide can be significantly underestimated by the simple test measurement performed [74]. Hence, the operation of the new ECRH system is a severe restriction to the new Doppler diagnostic. Currently, the simultaneous operation of both systems is not possible. However, a possible solution would be to install waveguide notch filters for the ECRH frequencies.

V-band system

The two V-band channels are installed in torus sector 13. The reflectometers are located above the torus, placed on the support structure of the tokamak. They

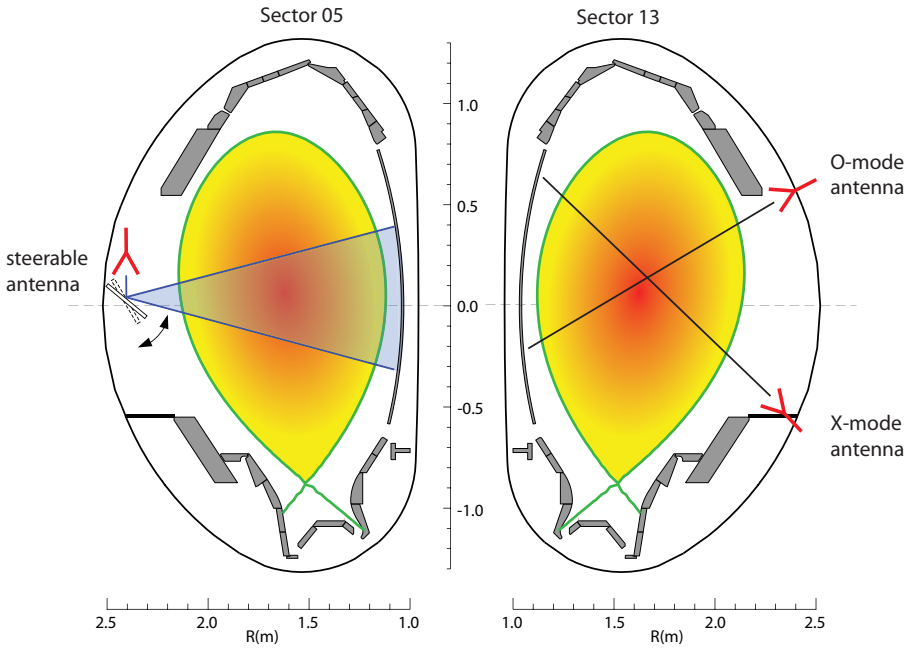

Figure 4.17: Lines of sight of the three Doppler antenna pairs: Fixed lines of sight for the O- and X-mode antenna in sector 13 and various lines of sight (indicated by blue region) for the steerable antenna in sector 05.

are connected to in-vessel antenna pairs via fundamental and oversized waveguide transmission lines (with mitre bends). Starting at the reflectometer with rectangular (WR-15) waveguides, the fundamental waveguides are converted to 25 mm diameter, smooth bore, circular waveguides using linear tapers. Just outside the vacuum vessel the circular waveguides are tapered down to fundamental waveguides again, which continue in-vessel to the separate launch and receive antennas. The vacuum window is a 25 μm thick mica sheet sandwiched between o-ring sealed waveguide flanges [31]. Two antenna pairs are mounted in the vessel, one pair with O-mode polarization positioned on the low field side, above the plasma magnetic axis and pointing downwards with an angle of $+34°$, and one pair with X-mode polarization placed below the magnetic axis and pointing upwards with $-42.5°$ relative to the horizontal. Figure 4.17 (right side) shows the positions of the O- and X-mode antenna pairs and their fixed lines of sight with respect to the vessel. The antennas consist of back-to-back pyramidal hog-horns with elliptic focusing mirrors. Figure 4.19 shows a sketch of the O-mode antenna pair and its orientation. The axes of both antenna pairs are skewed by 10° in the toroidal direction to roughly align with the magnetic field line inclination at the plasma edge, so that the wave electric field is launched either perpendicular (X-mode) or parallel (O-mode) to the magnetic field direction. Consequently, cross-polarization effects are minimized. A detailed description of the V-band antennas is given by Klenge [68].Using a combination of waveguide switches and directional couplers the two reflectometers can be connected

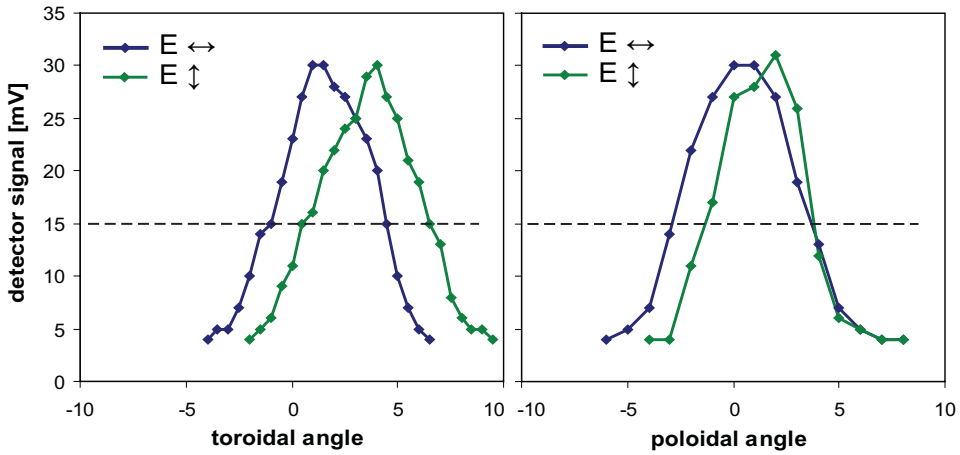

Figure 4.18: Far field beam divergence of the steerable antenna. The radiated power was measured using a square law detector [58]. The radiation pattern in the toroidal (left) and the poloidal plane (right) were measured for both wave electric field orientations (blue and green) at 105 GHz. The dashed line indicates the 3 dB width.

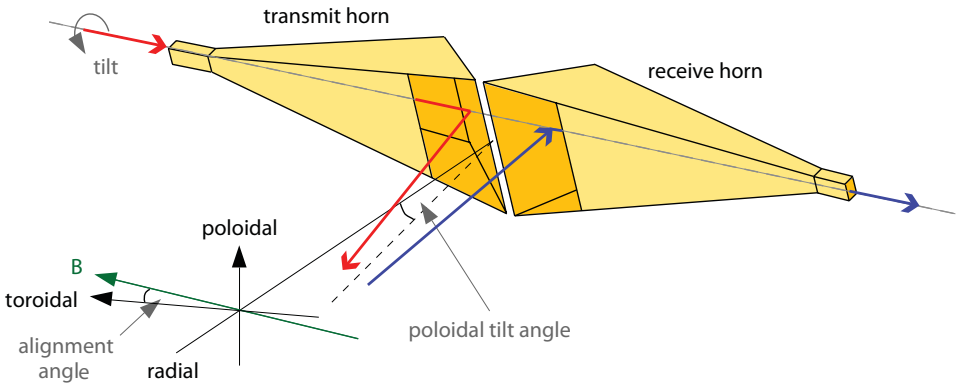

Figure 4.19: Sketch of O-mode hog-horn antenna pair with elliptic focusing mirrors (modified from [31]). The antennas are tilted in the poloidal plane and aligned toroidally with an edge magnetic field line inclination of 10°.

to different antenna pairs for simultaneous O- and X-mode measurements, or to the same antenna pair for radial correlation measurements [75].

4.3 Measurement technique & Data analysis

4.3.1 Measurement technique

The technique of Doppler reflectometry is based on the reflection of the launched microwave from a plasma cutoff. The radial position of this cutoff depends on the frequency of the wave. Furthermore, the cutoff position for a given frequency depends on the plasma density profile and the magnetic field of the tokamak. The O-mode cutoffs appear generally at higher densities compared to the X-mode cutoffs (see figures 4.3 and 4.23). With increasing density the cutoff layer position for a particular wave frequency shifts radially outwards. Hence, the lower the density the deeper the microwave propagates into the plasma before it gets reflected. When the density profile is (temporarily) stationary, different radial positions inside the plasma can be probed by changing the frequency of the microwave, since the radial cutoff position shifts with the launched frequency. Figure 4.23 shows that with increasing frequency the cutoff moves more and more towards the core.
Frequency hopping, i.e. stepping the launch frequency in a staircase fashion spanning the whole frequency band, allows for probing the plasma from edge to core. The number of different set frequencies, determines the number of radial measurement positions and thus the radial resolution. Typically, a frequency pattern has $20 - 25$ frequencies ranging from 75 GHz to 108 GHz in roughly equidistant frequency steps of ≈ 1.4 GHz. The choice of frequencies is influenced by the frequency response of the diagnostic (figure 4.6). Frequencies, for which the instrument response curve shows large dips and peaks are generally avoided. The length of a single frequency interval is typically $4 - 6$ ms depending on where in the plasma the measurement is taken. In the edge of the plasma ELM events can disturb the reflectometer signal and hence a longer step length is chosen, whereas in the plasma core the signal quality is very good and a smaller step length already provides sufficient data to extract a reliable average Doppler shift frequency. (Note that each change in launch frequency involves a settling time of less than 0.18 ms for the two reflectometer PLLs to re-lock.) The frequency step lengths and the number of frequencies are chosen such that a full frequency pattern repeats after 100 ms. Figure 4.20 shows a typical frequency pattern together with the received raw data displayed as a spectrogram. One observes that ELM events disturb the Doppler reflectometer signal [75]. For this reason only the Doppler signal measured in between ELMs is evaluated.

4.3.2 Frequency spectrum

The Doppler shift is extracted from the frequency spectrum (complex amplitude signal $I+iQ = A\ exp(i\phi)$) - figure 4.21. The spectrum usually has a narrow spike at zero frequency corresponding to the carrier wave intensity (due to leakage of the transmitter signal into the receiver). Also centered around zero frequency a broader peak is often found that is due to the $m = 0$ direct reflection. The Doppler component ($m = -1$ - backscattered signal) is a separate broad peak either up- or down-shifted in frequency depending on the direction of the plasma rotation. The Doppler shift frequency is obtained by a fitting procedure based on an algorithm, which first re-

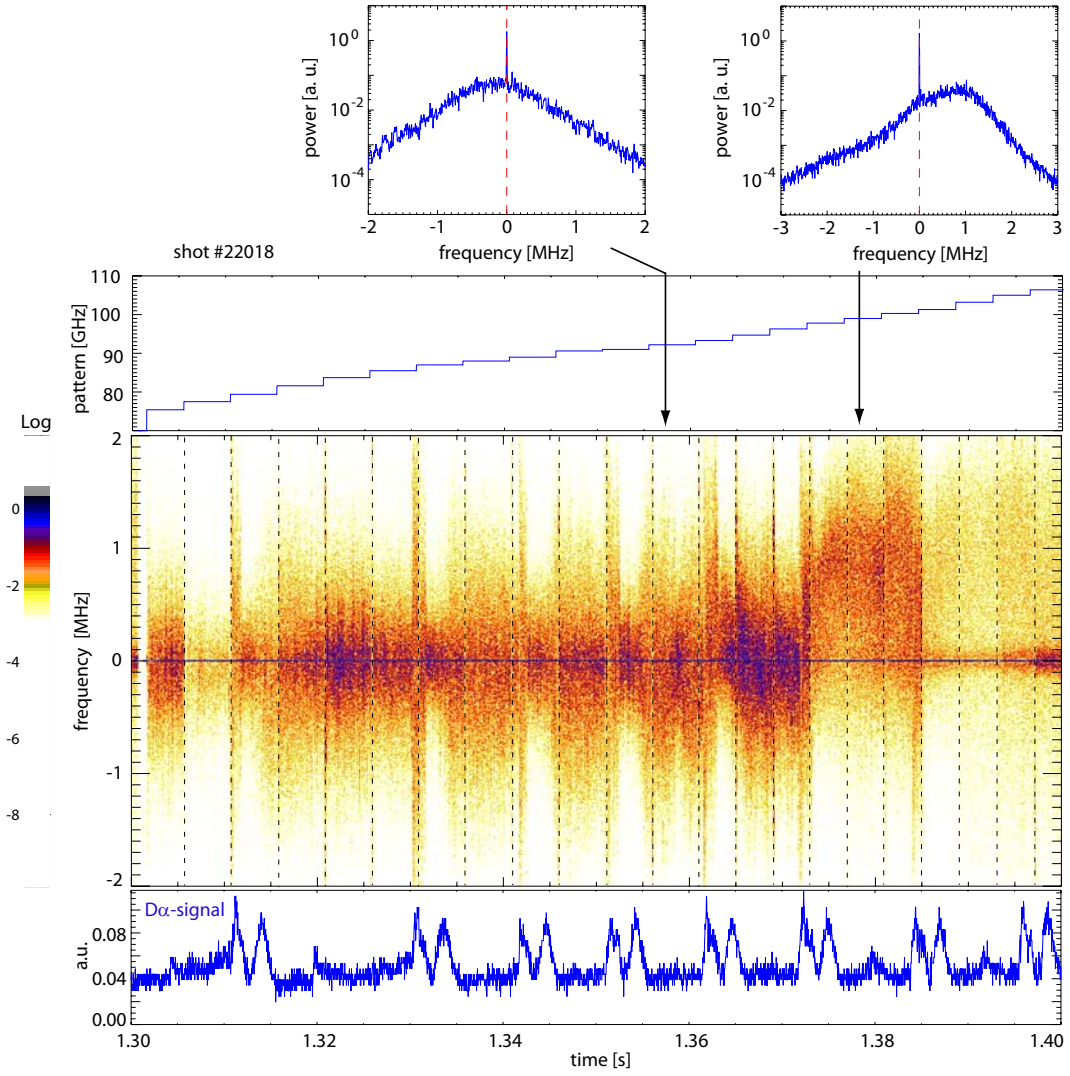

Figure 4.20: Frequency spectrogram of the raw Doppler reflectometer data for discharge #22018 along with the frequency pattern used for this measurement and the corresponding D_α-signal indicating the ELM events during this time slice ($1.30 - 1.40\,\mathrm{s}$ - H-mode).

moves the carrier peak, splits the spectrum into its symmetric and asymmetric parts and then fits either one or two double Gaussian to the asymmetric component (contains the Doppler shift information) using a least-squares minimization [68]. The center frequency of the Gaussian curve fitted to the Doppler peak is interpreted as the Doppler shift frequency f_D. The sign of f_D gives the rotation direction. For standard discharge configurations and antenna lines of sight pointing downwards with respect to normal incidence onto the cutoff layers a positive Doppler shift corresponds to a plasma rotation in the electron diamagnetic drift direction, while a

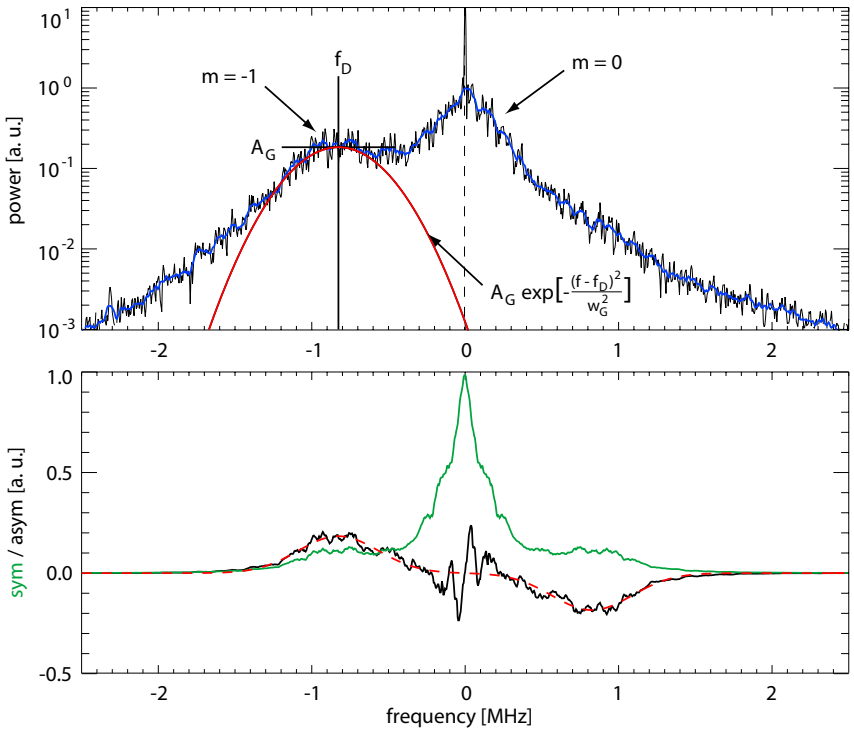

Figure 4.21: Frequency spectrum (complex amplitude signal $A\,exp(i\phi)$) with $m = 0$ direct reflection component and $m = -1$ Doppler peak. Also shown are the symmetric (green) and asymmetric parts (black) of the spectrum with fitted double Gaussian (red).

negative Doppler shift corresponds to a rotation in the ion drift direction (see figure 4.23). This correlation reverses when the antenna line of sight is pointing upwards. The sign convention is that a rotation in the ion drift direction corresponds to a positive rotation direction ($+u_\perp$).

4.3.3 $u_\perp$ profiles

The plasma rotation velocity perpendicular to the magnetic field ($u_\perp$) can be calculated from the measured Doppler shift using equation 4.10:

$$u_\perp = \frac{2\pi}{k_\perp} f_D$$

By stepping the frequency of the probing microwave through the whole W-band range Doppler shift spectra are obtained for each frequency. Hence, a radial profile of $u_\perp$ can be constructed by converting the launched microwave frequencies to radial cutoff positions. Using the frequency pattern of figure 4.20, a complete plasma rotation profile is measured every 100 ms during the discharge. The determination of the cutoff layer position inside the plasma requires some effort.
For normal incidence of the probing beam onto a plasma slab, the cutoff position can

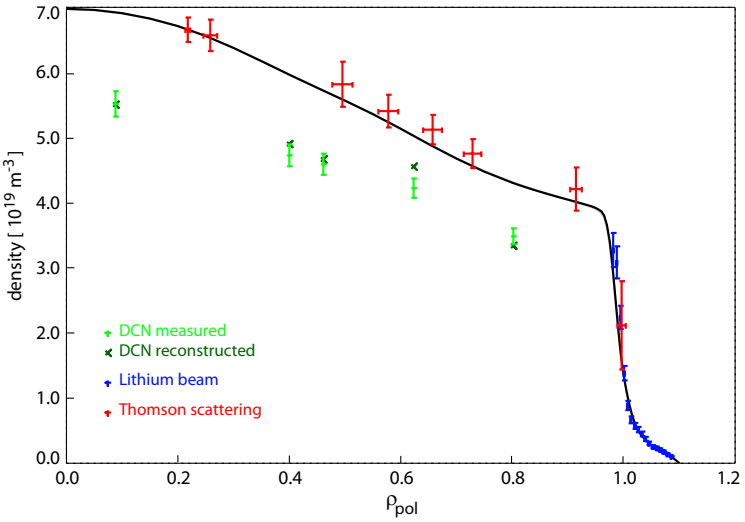

Figure 4.22: Density profile of discharge #22343 at 1.8 s obtained by combining density data of different diagnostics.

be calculated theoretically for a given density profile and magnetic field using the cold plasma approximation [76]. The cutoff layers in figure 4.23 and also the cutoff frequencies plotted in figures 4.3 and 5.2 b) are calculated this way. Analytic equations for O- and X-mode cutoffs for poloidally oblique incidence onto a plasma slab are given in reference [77]. However, there exist no analytic expressions in the literature that would account for experimental conditions like toroidally oblique incidence (here 6.12°), significant cutoff curvature, beam divergence and (strong) beam refraction. Especially in the core region and for high poloidal tilt angles beam refractive effects are very strong and cause a significant discrepancy between the analytically calculated and the true cutoff position. For this reason the cutoff positions have to be determined using beam tracing with real plasma and magnetic field geometry. The ray tracing calculations are performed with the TORBEAM code [59]. This beam tracing code was developed at ASDEX Upgrade for numerical calculation of the propagation and absorption of electron cyclotron waves in tokamak plasmas. Since TORBEAM takes effects of refraction into account, the code is applied for calculating the trajectories of the microwave beams launched for Doppler reflectometry measurements. Figure 4.23 shows examples of ray traces (trajectories of the beam axis) as blue curves for three different microwave beams (92, 98 and 108 GHz) launched with X-mode polarization. The corresponding cutoff layers analytically calculated for normal incidence are highlighted (thicker lines) for comparison. The antenna line of sight is the same in each of the three cases (1.8°). The ray trajectories follow the antenna line of sight outside the plasma, but then the rays deflect within the plasma not reaching the plotted corresponding cutoff layers. The further the ray penetrates into the core, the greater the discrepancy between the deflected ray and the cutoff layer. At the plasma edge the difference is usually small ($\Delta\rho_{pol} \approx 0.01$), but in the

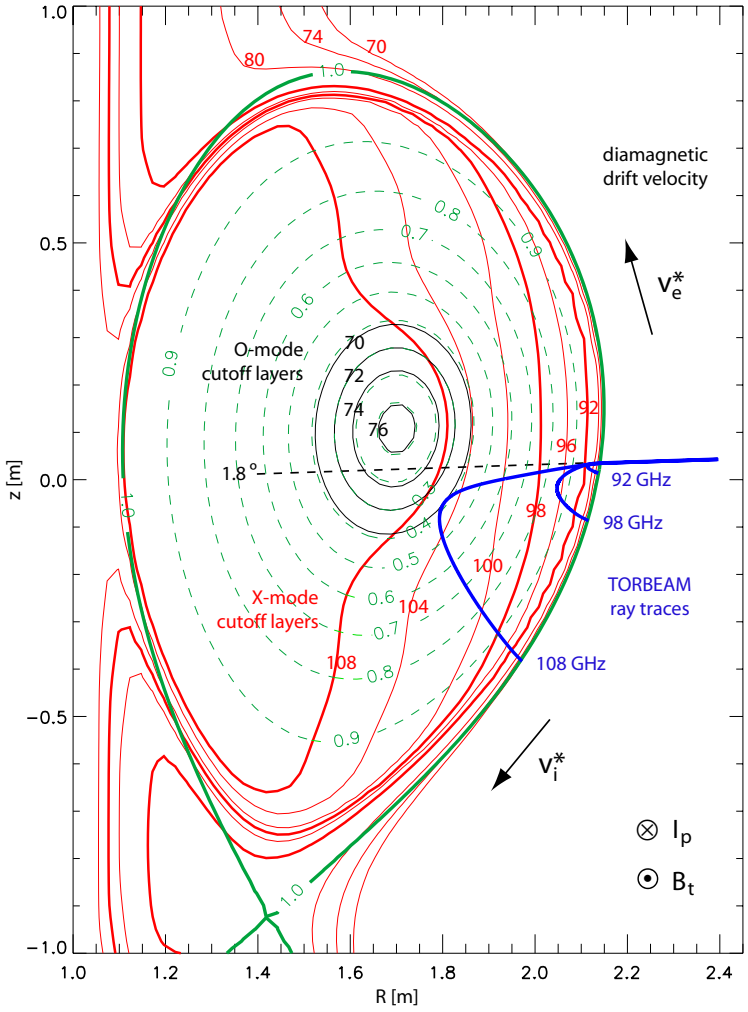

Figure 4.23: Poloidal plasma cross section showing TORBEAM ray traces for three microwave beams with different frequencies launched from the steerable Doppler antenna. Also shown are O- mode (black) and X-mode cutoff layers (red) for various GHz-frequencies calculated with equations [76] assuming normal incidence of the beam onto a plasma slab. The arrows indicate the diamagnetic drift direction for the ions and electrons in a plasma with standard discharge configuration.

core the difference is significant. For small tilt angles the discrepancy in the core is already considerable ($\Delta\rho_{pol} \approx 0.1$ - figure 4.23) and for steep tilt angles it is even more severe ($\Delta\rho_{pol} \approx 0.25$ - figure 5.2 a). For the data analysis of the Doppler measurements the cutoff position is determined as the radial position where the index of refraction along the ray trajectory reaches a minimum. This cutoff often corresponds to the position where the ray trace bends over (minimum in ρ_{pol}). A comparison between TORBEAM beam tracing and full-wave code simulation [78] validated beam tracing as an appropriate tool for determining the radial cutoff position, although

the simpler beam tracing model actually becomes void in the cutoff region. The major advantage of beam tracing is that a single run using real plasma conditions takes only a few seconds compared to a full-wave simulation run with approximated discharge conditions requiring hours of computation. Hence, each measurement position is obtained using TORBEAM with an experimental density profile and plasma equilibrium reconstruction. The used density profile is a combination of profile data from DCN interferometry, Thomson scattering and Li-beam. Figure 4.22 shows an example profile (discharge # 22343 at 1.8 s). The Li-beam diagnostic [48] provides very good density data for the plasma edge (SOL and pedestal region), while the DCN interferometry [46] and Thomson scattering diagnostic [47] cover mainly the core region. Note that the DCN data points do not lie on the profile curve, since the interferometry technique measures a line integrated density. But the fitted profile reconstructs the DCN line integrals quite well.
In addition to the radial cutoff position a TORBEAM run also provides the local perpendicular turbulence wavenumber at the cutoff, which is calculated via the Bragg equation 4.8 using the minimum of the index of refraction N along the ray trace:

$$k_\perp = 2k_0 N,$$

where k_0 is the wavenumber of the probing microwave beam. Taking the inverse of $k_\perp$ and multiplying it with $2\pi f_D$ (obtained from the corresponding frequency spectrum) yields $u_\perp$ at the cutoff. Various examples of $u_\perp$ profiles are presented in chapters 5 and 6.

4.3.4 $k_\perp$ spectrum

Since the Doppler reflectometry technique is sensitive to a specific perpendicular turbulence wavenumber selected by the antenna tilt angle via the Bragg condition, it is possible to measure the turbulence $k_\perp$ spectrum by scanning the tilt angle. In addition, Doppler reflectometry provides a radially localized measurement of the spectrum. However, for a fixed probing frequency a scan of the antenna tilt changes not only the probed $k_\perp$ via N but also the measuring position due to beam refraction. Scanning the probing frequency ω_0 on the other hand changes of course the cutoff position and also $k_\perp$ through k_0. Thus, obtaining the $k_\perp$ spectrum at a fixed radial position (in terms of ρ_{pol}) requires combining data from both tilt and frequency scans.
The received Doppler shifted signal power is an indicator of the fluctuation amplitude. The backscattered power at $(k_\perp, \omega)$ is proportional to the spectral power density (also called spectral distribution function) of the density fluctuations

$$S(k_\perp, \omega) = |\tilde{n}(k_\perp, \omega)|^2 \tag{4.15}$$

The spectral power density $S(k_\perp)$ at the wavenumber $k_\perp$ is obtained by integrating over the frequency spectrum. The integral of the Doppler shifted component is directly proportional to the amplitude (A_G) times the width (w_G) of the Gaussian

fit curve. Hence,

$$S(k_\perp) \sim |\tilde{n}(k_\perp)|^2 \propto A_G \cdot w_G \tag{4.16}$$

Both, the peak power and the width are obtained from the frequency spectrum (figure 4.21). The probed turbulence $k_\perp$ is determined using beam tracing (as above). The received signal power needs to be corrected for the frequency response of the diagnostic and the gain setting of the variable gain amplifier (subsection 4.2.1) in order to extract the actual backscattered power.
Full wave simulation is used to study the variation of the Bragg backscattering efficiency with the antenna tilt angle [79, 80, 81]. Various physical and geometric conditions need to be taken into account like e.g. forward scattering contribution (path losses), broad band turbulence and realistic plasma geometry (curved cutoff layers, real density profiles and magnetic field geometry). However, these aspects are incorporated only partly in the different codes [82]. Hence, the simulation results have not reached a stage of sufficient reliability. Nevertheless, preliminary simulation results by Lechte, which are obtained by employing simplified plasma geometry (slab, linear density gradient) and turbulence (sinusoidal perturbation), show a dependence of the scattering efficiency on the tilt angle [83]. This finding is confirmed by the results of other full wave codes [80, 81]. Generally, a decrease of the received backscattered power with increasing tilt is observed. However, quantitative predictions can not be made at the present state [82]. The current simulation results indicate that the scattering efficiency depends non-linearly on various factors like e.g. the polarization of the microwaves, the fluctuation level and the size of the scattering region. The latter is linked to the penetration depth in the case of divergent beams and hence to the antenna geometry plus the associated radiation pattern. Since a validated, systematic full wave simulation study for a X-mode polarized microwave beam does not exist presently, the $k_\perp$ spectra presented in chapter 7 are not corrected for the scattering efficiency variation with the tilt angle. The possible effects of a corresponding correction on the measured spectra is discussed in section 7.3.

4.3.5 Errors

The two sources for the $u_\perp$ uncertainty are the perpendicular wavenumber and the Doppler shift frequency. The uncertainty of f_D arises mainly from the fluctuations of the Doppler shift with time (especially in the presence of ELM events) and also sometimes from the grade of accuracy of the Gaussian fit to a poorly pronounced Doppler peak. Usually, a frequency interval is divided into smaller time slices and a value of f_D is determined for each time slice. The error is then deduced from the variations in f_D during the full frequency interval. In the case of poorly pronounced Doppler peaks an additional uncertainty is added, estimated from visual interpretation. Depending on the quality of the raw data f_D can be generally determined with an accuracy of $\pm 50 - 200\,\mathrm{kHz}$ - typically $\pm 100\,\mathrm{kHz}$. The determination of $k_\perp$ relies strongly on the (correct) modeling of the divergence and refraction of the launched microwave beam along its path. Although the adjustment of the antenna line of sight is calibrated, a possible error in the antenna setting cannot be excluded. Hence, the uncertainty in the beam propagation dominates

the measurement error of $k_\perp$. For the analysis performed in this thesis the error of the antenna adjustment is assumed to be $\pm 1°$. An error analysis using the beam tracing code gives an estimate of the $k_\perp$ and also ρ_{pol} errors due to this adjustment uncertainty. It is found that the relative $k_\perp$ errors decrease with increasing antenna tilt angle. For low tilt angles the errors range between 10% and 14% depending on the frequency or equivalently the radial position. For moderate tilt angles the relative $k_\perp$ errors reduce to 9% - 12% and for high tilts the error range is 5% - 7%. The radial errors increase with increasing microwave frequency and additionally with increasing antenna tilt angle. For small frequencies probing the outer edge of the plasma ($\rho_{pol} < 0.95$) the ρ_{pol} error is generally smaller than 0.005 for all possible tilt angles. For frequencies probing the region $0.95 > \rho_{pol} > 0.75$ the radial errors are in the range of 0.005 - 0.020 depending on the tilt angle. When probing the plasma region where $\rho_{pol} < 0.75$ the errors range between 0.010 and 0.025.
It should be pointed out that the density profile used in the beam tracing for data analysis and error analysis is a potentially significant error source. The uncertainty of the density profile imposes a systematic error on the measurement and the determination of the corresponding errors. Obviously this affects the radial measurement positions, but also the measured $u_\perp$ through $k_\perp$. Note that the systematic error due to the (possible) incorrectness of the density profile is not included in the measurement errors given above. Nevertheless, this error source is minimized by using a combination of profile data from several diagnostics. In addition to the density profile, beam tracing relies on the plasma equilibrium reconstruction using the CLISTE code [84]. Hence, errors in the equilibrium calculation also contribute to the systematic error in the Doppler measurements.

Besides f_D, also A_G and w_G depend on the quality of the Doppler shifted component in the frequency spectrum and the accuracy of the Gaussian fit to the peak. Generally, the uncertainty induced by the amplitude fluctuation of the Doppler peak with time during a frequency interval is greater than the error due to a deficient fitting. The uncertainty of A_G and w_G is minimized by averaging over the time interval of a frequency step. The resulting errors are typically small ($< 10\%$). Only when probing very low or high turbulence wavenumbers the errors can reach up to 20%. The $k_\perp$ spectra are analyzed for a small radial range typically $\Delta\rho = 0.025$. Hence, often more than one frequency step (corresponding to a certain tilt angle) contribute to the spectrum yielding two or more data points with very similar $k_\perp$ values. The variation of $S(k_\perp) \propto A_G \cdot w_G$ seen in the spectrum generally exceeds the errors of A_G and w_G deduced for the single frequency steps (from amplitude fluctuations during the intervals). Hence, the $S(k_\perp)$ error bars are derived from the spreading of the data points in the spectrum at a fixed $k_\perp$. Depending on the probed wavenumber the relative errors typically reach 20% or even up to 35% for high turbulence wavenumbers (figure 7.1). In cases were only one data point is available for a certain $k_\perp$ value (i.e. tilt angle) typical error values are assumed.
Since the measurement of a $k_\perp$ spectrum requires several identical plasma discharges (chapter 5), a systematic error is introduced, which depends on the reproducibility of the discharge conditions. Another (minor) systematic error is caused by the in-

crease of the path losses with increasing penetration depth of the microwave beam. However, this error only affects the comparison of $k_\perp$ spectra from different radial positions and not the measured spectrum itself. A possibly significant source of error is the variation of the diagnostic response with the antenna tilt angle (see section 4.3.4). Full wave simulations show a dependence of the backscattered power on the (variable) tilt angle [79, 80, 81]. However, more detailed full wave simulations are needed to establish a clear relationship between $S(k_\perp)$ of the scattered signal detected by a Doppler reflectometer and the level of turbulence at $k_\perp$. This error source and its possible impact on the measurement is discussed in detail in chapters 8.

Chapter 5

Performance of new Doppler channel

5.1 General description

The current V-band Doppler reflectometry system allows for measuring radial profiles of the perpendicular plasma rotation velocity ($u_\perp$) from which profiles of the radial electric field (E_r) can be deduced. However, the plasma core is only accessible in low density discharges and the measurements are hence mostly restricted to the plasma edge and Scrape-off layer. The availability of two V-band reflectometer units offers the possibility to measure the radial correlation lengths of the turbulence and the E_r-shear rate via correlation Doppler reflectometry [75, 63]. Although the V-band system provides the opportunity for a variety of measurements, the access to differing turbulence wavenumbers ($k_\perp$) is very constrained. As described in section 4.2.3 the V-band channels employ antennas with fixed lines of sight (figure 4.17) that set the probed turbulence wavenumbers to a small range. A (limited) scan of the turbulence wavenumber can be performed only by varying the shape of the plasma. However, by changing the plasma triangularity, plasma conditions are likely to change, too [63, 31].
This drawback of the V-band system motivated the installation of a new remote-steerable antenna with a variable line of sight, which allows for dynamic wavenumber selection. Consequently, the steerable antenna (section 4.2.3) offers the possibility to measure the turbulence wavenumber spectrum for a variety of constant plasma conditions. Figure 5.1 shows a selection of possible vacuum lines of sight with respect to the plasma. (These lines of sight were used for the wavenumber spectrum measurements - see section 7.) The second important upgrade of the Doppler reflectometry system is the corresponding reflectometer, which features an improved design (section 4.2.1). It operates in the W-frequency-band and hence allows for probing a wider radial range compared to the V-band system. Using the new channel with X-mode polarization of the microwaves, radial profiles of $u_\perp$ can be measured with good edge to core coverage. In addition, higher turbulence wavenumbers can be probed when operating with W-band frequencies, since the

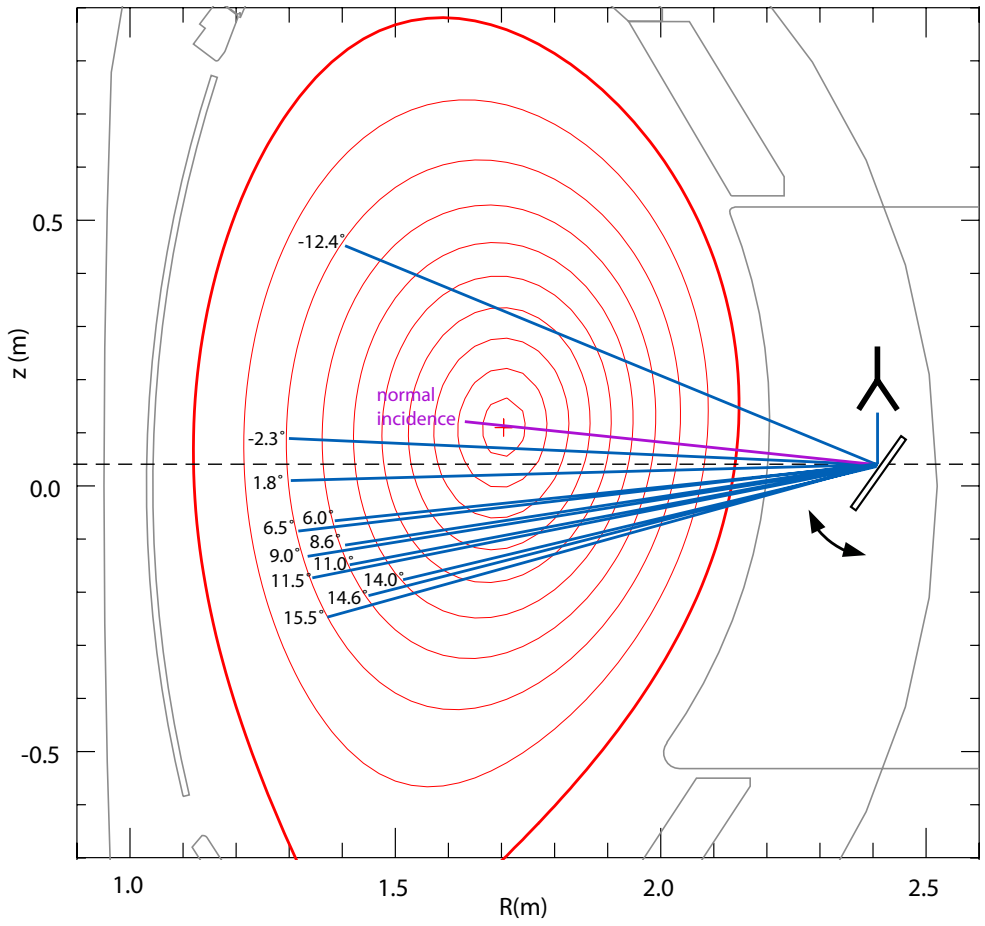

Figure 5.1: Various possible vacuum lines of sight of the steerable antenna. The given angles are measured relative to the horizontal. The magnetic flux surfaces are shown in red.

vacuum wavenumber (k_0) of the launched microwaves enters the Bragg condition (equation 4.8). The analysis of the received scattered power requires the precise knowledge of the diagnostic frequency response in order to obtain the turbulence wavenumber spectrum. Therefore, a frequency stable transmitter is a design requirement for the W-band reflectometer. The older V-band reflectometer have just free-running oscillators as transmitter sources, which are inherently unstable sources. Additional frequency uncertainties due to temperature drifts during an operation day impede the precise determination of the frequency response of these units. (Note that the reliability of the $u_\perp$ profile measurement is practically not affected by this circumstance.) The W-band reflectometer in contrast employs a custom-made phase locked frequency synthesizer as transmitter source and is hence suited for measuring wavenumber spectra.

The operating range of the new channel in terms of radial and wavenumber coverage is illustrated in figure 5.2 c) for a given discharge (see section 5.3). Plotted are

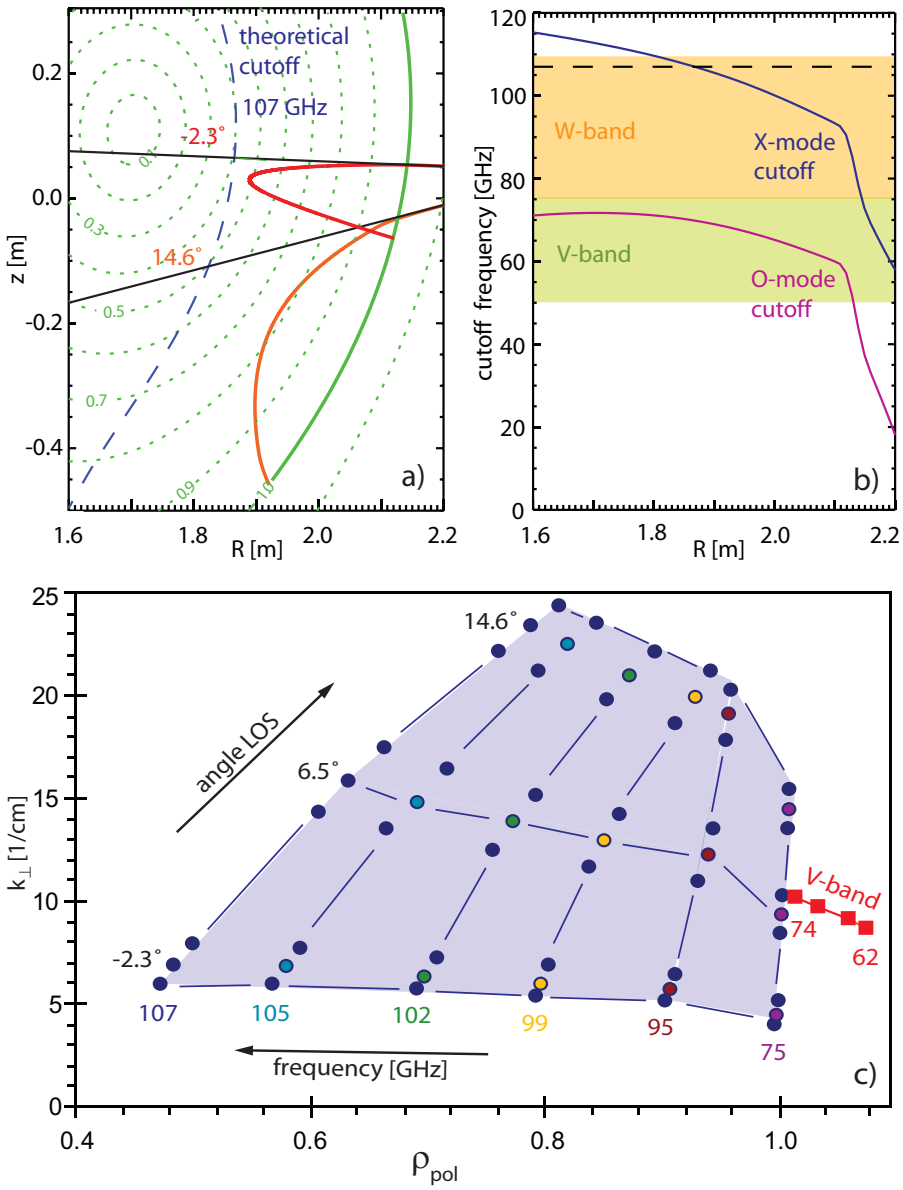

Figure 5.2: Operating range of the new Doppler channel. a) Ray traces of the reflected beam (scattering order $m = 0$) for two different tilt angles (black lines indicate the vacuum lines of sight) and a fixed frequency of 107 GHz. b) Theoretical cutoff frequencies (normal incidence) for O- and X-mode polarization at the plasma midplane. The dashed line marks 107 GHz. c) Probed perpendicular wavenumbers for a given frequency and antenna tilt angle plotted versus the corresponding radial cutoff position obtained by beam tracing.

the probed $k_\perp$ values for a particular frequency and antenna tilt angle versus the corresponding radial cutoff position. The various colors mark different frequencies

specified in the figure together with the used antenna tilt angles. The shaded area indicates the experimentally accessible perpendicular wavenumbers and radial positions for this example discharge. The plot however is typical of ASDEX Upgrade plasma conditions. Raising the density or the magnetic field pushes the access region radially outwards. For a given antenna tilt angle the probed $k_\perp$ varies with radial position. $k_\perp$ increases from the edge to the core, because the frequency and so k_0 is increasing in this direction ($k_\perp \sim k_0$). Therefore, when presenting radial profiles the probed $k_\perp$-span is always given in addition to the tilt angle setting. The small $k_\perp$ value corresponds to the radially outermost point and the high $k_\perp$ value to the innermost point of the profile. For low antenna tilt angles the plasma core can be probed. Note that the actual minimum values of ρ_{pol} for each antenna tilt depend on the density profile, which determines the radial cutoff position for a given frequency (figure 5.2 b), section 4.3). The refraction of the microwave beam inside the plasma intensifies with increasing tilt angle and diminishes the radial access. This fact is illustrated in figure 5.2 a), where ray traces of the reflected beam are shown for two different tilt angles and fixed frequency. Thus, the opportunity to probe the higher turbulence wavenumbers is at the expense of radial coverage. Summarizing, core profiles are best measured at low tilt angles, where the radial coverage is widest and wavenumber spectra are best measured around $\rho_{pol} = 0.7 - 0.9$, where the wavenumber coverage is widest. For comparison, the red line in figure 5.2 c) indicates the ρ_{pol}- and $k_\perp$ values accessible when using the fixed tilt V-band system and X-mode polarization. Note that O-mode polarization yields a wider radial coverage ($\rho_{pol} \approx 1.0 - 0.7$).

5.2 Commissioning

With the start of the experimental campaign in May 2007 the W-band channel was put into operation and for the first time the system performance could be tested during plasma operation. A first scan of the antenna tilt angle demonstrated that pronounced Doppler shifts can be measured for the whole set of possible lines of sight. In order to validate the results of the new diagnostic, they were cross-checked with the results obtained with the established V-band system. For a direct comparison of the two systems the V-band channel is operated in O-mode polarization, while the W-band channel is operating in X-mode to allow for a radial overlap of the two systems. Note that the W-band channel still has a wider radial coverage in general. The tilt angle of the steerable antenna was adjusted such that similar $k_\perp$ values were probed with the two channels. For this setting the measured radial profiles of the plasma rotation velocity $u_\perp$ agree very well within errors. Two examples are shown in figures 5.3 and 5.4, where the results of the W-band channel (red) and the V-band channel (blue) are overlaid for comparison. The profiles were measured during a discharge with standard plasma configuration ($B = -2.5\,\mathrm{T}$, $I_p = +0.8\,\mathrm{MA}$).
The perpendicular rotation velocity is the sum of different velocity terms.

$$u_\perp = v_{E\times B} + v_{turb} = v_\phi \frac{B_\theta}{B} - v_\theta \frac{B_\phi}{B} - v^* + v_{turb} \tag{5.1}$$

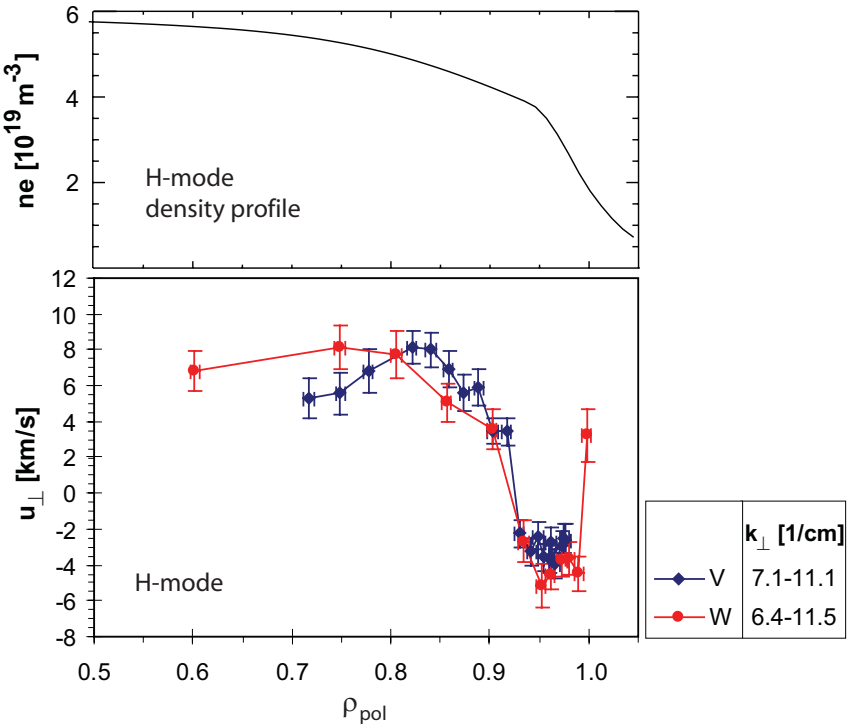

Figure 5.3: Comparison of radial $u_\perp$ profiles measured with the W-band (X-mode) and the V-band system (O-mode) during the H-mode (3.3 s) phase of discharge #21820.

The $E \times B$ velocity is given by the force balance equation for a particular plasma species (i.e. ion, electron or impurity) and is composed of a toroidal ($v_\phi B_\theta / B$), a poloidal ($v_\theta B_\phi / B$) and a diamagnetic (v^*) velocity term. In general, the intrinsic phase velocity of the turbulence is negligible with respect to $v_{E\times B}$. In the plasma core region $u_\perp$ is positive and generally dominated by the toroidal fluid velocity term [75, 31]. At the plasma edge $u_\perp$ reverses direction coinciding with the large pressure gradient in the pedestal region leading to the diamagnetic and poloidal velocity terms becoming more significant. The radial positions of the negative dip in the profiles of figures 5.3 and 5.4 agree for both channels and are consistent with previous Doppler reflectometry measurements. However, the pedestal "knee" at $\rho_pol = 0.95$ in the fitted H-mode density profile may be at a slightly too low ρ_pol value. This in turn would affect the radial position of the dip in the corresponding profile, which directly depends on the density profile. If the pedestal knee would shift more towards the edge, then the width of the negative dip would decrease accordingly and the described correlation between pedestal region and negative $u_\perp$ is maintained. The depth of the negative dip generally increases with increasing confinement [75]. In the plasma scrape-off layer $u_\perp$ is positive again.
Comparing the profiles measured during the L-mode and H-mode phase of the discharge shows some differences. For the L-mode phase, the radial coverage is increased

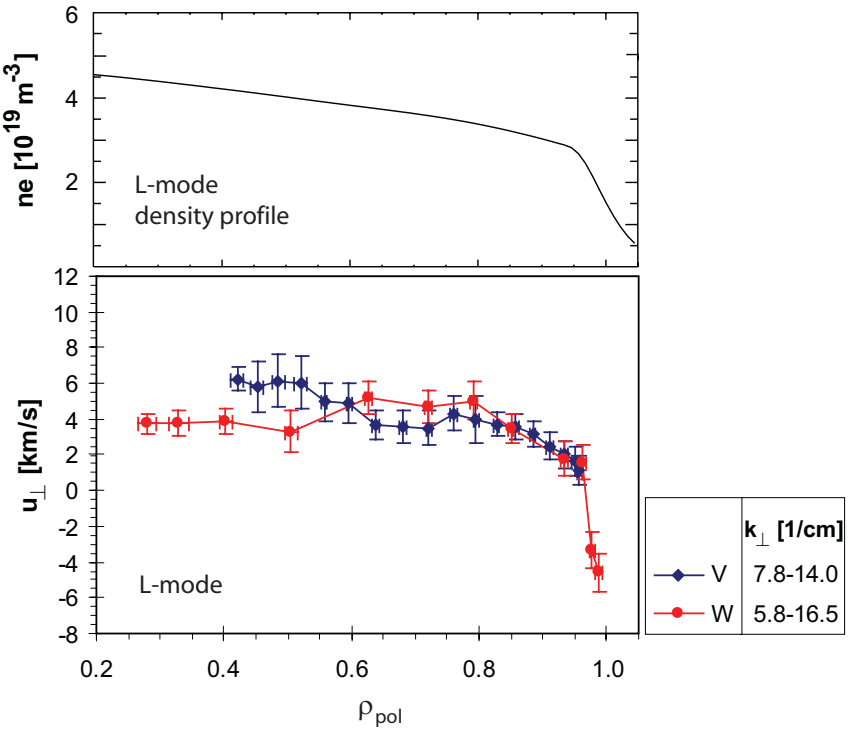

Figure 5.4: Comparison of radial $u_\perp$ profiles measured with the W-band (X-mode) and the V-band system (O-mode) during the L-mode (4.2 s) phase of discharge #21820. Note the different radial scale compared to figure 5.3.

towards the core due to a lower density profile shifting the cutoff layers to lower ρ_{pol} values. Also, a lower rotation velocity is measured in the core due to less NBI power injected during this discharge phase (2.5 MW opposed to 7.5 MW in H-mode phase). For this discharge the depths of the negative dip are comparable in both confinement regimes. However, the dip is substantially broader in H-mode (expanding radially inwards) leading to a better confinement.

Figure 5.5 shows further examples of $u_\perp$ profiles measured during a different discharge with similar plasma conditions ($B = -2.5\,\mathrm{T}$, $I_p = +0.8\,\mathrm{MA}$, 2.5 MW NBI). Again, a good agreement within the errors is found between the V-band and W-band channel, although in this case different wavenumbers were probed by the two channels. The measured $u_\perp$ increases towards the core and rolls over around $\rho_{pol} \approx 0.75$.

5.3 Discharge series

The steerable antenna is controlled via a mechanical steering linkage, which currently is manually operated. Thus, changing the antenna line of sight requires entry to the ASDEX Upgrade torus hall. In order to scan the probed turbulence wavenumber for measuring the $k_\perp$ spectrum several identical discharges are required,

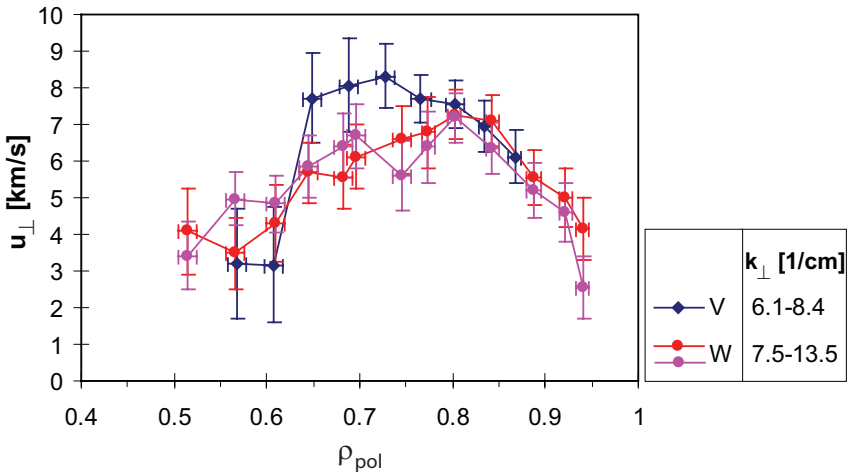

Figure 5.5: Comparison of radial $u_\perp$ profiles measured with the W-band (X-mode) and the V-band system (O-mode) during discharge #21828 (1.3 s, L-mode). Note that different $k_\perp$ values are probed by the two channels.

since the antenna tilt angle can only be adjusted between shots. For this reason two different discharge series were performed to address various physical aspects.

The first discharge series consists of seven identical discharges. The discharges were well reproducible thus providing constant plasma conditions for the measurement. The antenna tilt setting was different for each shot of the series. Table 5.1 lists the shot numbers and the corresponding antenna tilt angles measured relative to the horizontal (figure 5.1). The lowest $k_\perp$ values are probed using a tilt angle, that is close to normal incidence onto the cutoff layers. Here $-2.3°$ was chosen as a compromise between probing low wavenumbers and being able to resolve the Doppler peak in the frequency spectrum. With increasing tilt angle also the probed $k_\perp$ values increase. The highest turbulence wavenumbers are probed with a tilt angle close to the operational limit of the steerable antenna - here 14.6°. By using a tilt angle of $-12.4°$ similar $k_\perp$ values are probed as when using a tilt of 1.8°, since the tilt angle at the cutoff layer is similar for both antenna settings.
The discharge scenario for the first shot series is based on a discharge with standard configuration and plasma shape. This LSN discharge with a magnetic field of $B = -2.5\,\mathrm{T}$ and a plasma current of $I_p = +0.8\,\mathrm{MA}$ is purely NBI heated. The NBI heating power is applied in two steps - 2.5 MW and 5.0 MW - to generate discharge phases with different confinement regimes, since the primary intension of this experiment is to compare the $k_\perp$ spectra measured during L- and H-mode. The density in these discharges is optimized using gas puff fueling for Doppler measurements to provide good edge to core coverage. Figure 5.6 shows the time evolution of important plasma parameters for this discharge sequence. After the plasma current ramp-up the NBI power is raised to 5.0 MW and the core density increases to about $5.8 \times 10^{19}\,\mathrm{m}^{-3}$. At 1.06 s the discharge changes from L- to

shot number	tilt angle	probed $k_\perp$
22009	-2.3°	4-6 cm^{-1}
22010	1.8°	6-10 cm^{-1}
22011	6.5°	9-14 cm^{-1}
22012	9.0°	12-17 cm^{-1}
22013	11.5°	14-19 cm^{-1}
22014	14.6°	15-23 cm^{-1}
22018	-12.4°	7-11 cm^{-1}

Table 5.1: Shot numbers of the first discharge series and corresponding antenna tilt angle settings plus probed $k_\perp$ values.

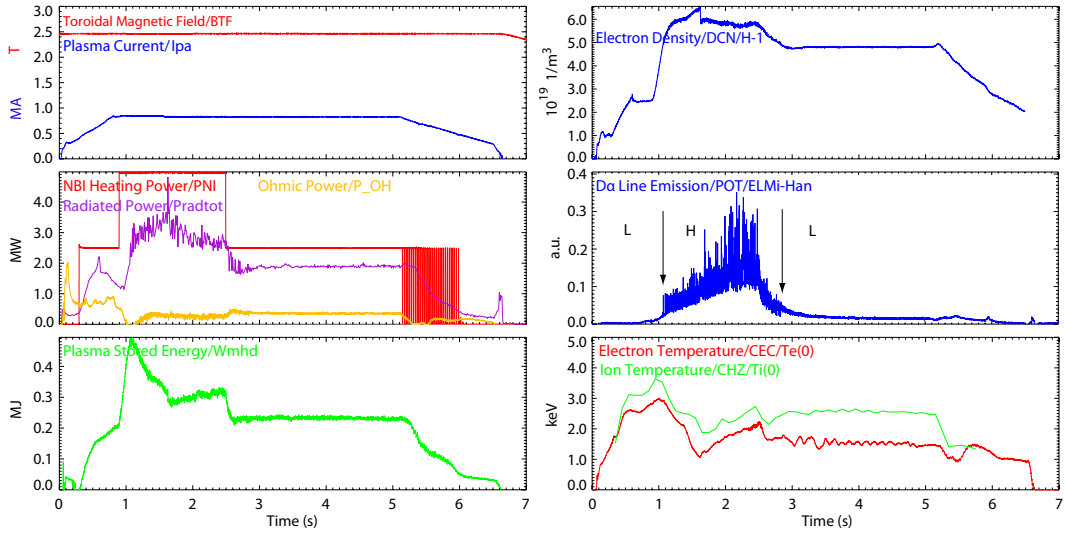

Figure 5.6: Time traces of important plasma parameters for the first discharge series.

H-mode, indicated by the measured D_α line radiation intensity in the divertor. The L-H transition is identified at the point when the D_α signal shows spikes, which correspond to ELM events. These are a characteristic of the H-mode. During the H-mode phase the core electron and ion temperatures fall and rise again due to (2, 1) MHD-mode activity, which is reflected by a steep decrease and a following increase of the plasma stored energy. (The MHD-mode was present throughout the H-mode phase for all discharges of the sequence.) When the NBI heating power is reduced to 2.5 MW at 2.5 s the discharge goes back to L-mode accompanied by a reduction in the stored energy and core density ($4.8 \times 10^{19}\,m^{-3}$). Compared to the H-mode phase the ratio of the power coupled to the plasma (NBI power plus ohmic power) and the power radiated from the plasma is smaller in L-mode.

shot number	tilt angle	probed $k_\perp$	comment
22343	1.8°	6-10 cm^{-1}	no GDC
22344	6.0°	9-14 cm^{-1}	no GDC
22348	8.6°	11-16 cm^{-1}	no GDC
			air leak and N_2-flooding machine conditioning
22404	11.0°	13-17 cm^{-1}	10 min He-GDC,
22405	14.0°	14-18 cm^{-1}	10 min He-GDC,
			problems with I_p ramp-up start-up tests
22429	15.5°	19-21 cm^{-1}	2 min D-GDC
22430	-2.3°	4-6 cm^{-1}	2 min D-GDC
22432	-12.4°	7-12 cm^{-1}	10 min D-GDC

Table 5.2: Shot numbers of the second discharge series and corresponding antenna tilt angle settings plus probed $k_\perp$ values. The fourth column lists the pre-shot glow discharge cleaning (GDC) intervals and operation incidents.

The second discharge series consists of eight discharges divided unintentionally into three blocks. The three discharges of the first block were made with a well conditioned machine. Then unfortunately, the breaking of a vacuum feedthrough caused a serious air leak and the vessel was flooded with N_2 to prevent further contamination of the machine. After a series of conditioning discharges another two shots of the Doppler discharge sequence were performed. In order to achieve plasma breakdown 10 min of helium glow discharge cleaning before the shot was necessary. Consequently, the helium content of the plasma was relatively high in these two discharges. The poor machine conditions then caused a further interruption of the discharge series. Finally, the last three discharges of the Doppler sequence could be done with a reasonably conditioned machine. However, glow discharge cleaning using deuterium was still necessary. Table 5.7 lists the shot numbers of the second discharge series and the corresponding antenna tilt angle settings. In addition, the glow discharge cleaning intervals and the operation incidents are given in a fourth column.

Of course, the same discharge scenario was used for each shot of the second series. However, the plasma condition were not perfectly reproducible throughout the whole discharge sequence. Figure 5.7 shows time traces of the main plasma parameters. Despite possible small variations in the measured quantities, the time evolution of discharge #22405 is representative of the second series. The shot is a pure H-mode discharge with standard configuration ($B = -2.5\,\mathrm{T}$, $I_p = +0.8\,\mathrm{MA}$) and LSN

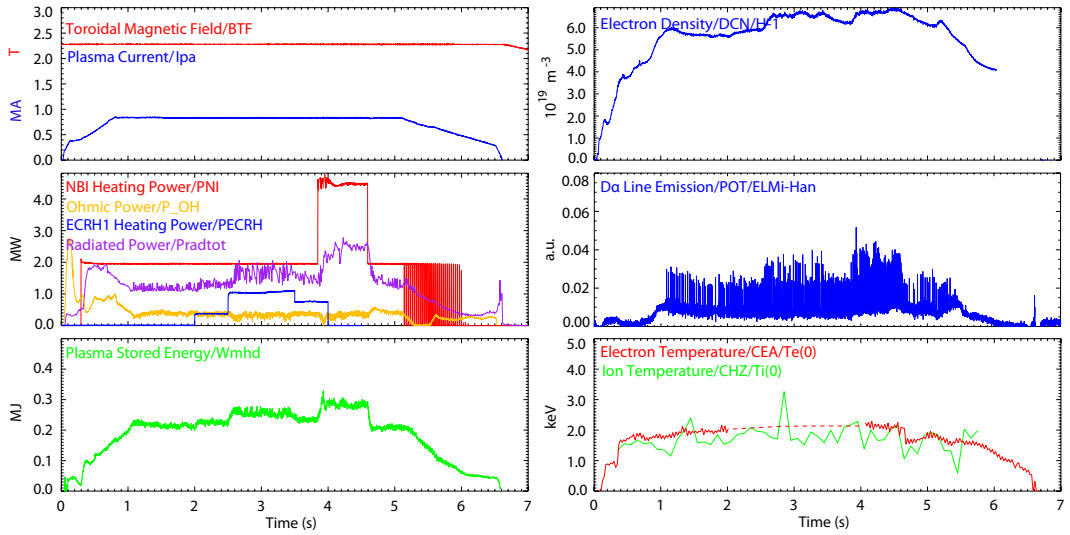

Figure 5.7: Time traces of important plasma parameters for the second discharge series (represented by discharge #22405).

shape. Also for this series the density is optimized to give a wide radial coverage for the Doppler measurements (core density around $6.0 \times 10^{19}\,\mathrm{m}^{-3}$). Compared to the first discharge sequence a different heating scheme is applied this time, since the intention of this second experiment is to measure the $k_\perp$ spectrum during discharge phases which are dominated by different turbulence forms. Phases with strong electron heating should be dominated by TEM/ETG type turbulence, while without direct electron heating other turbulence forms (ITG, TEM) should prevail. In these discharges stepped NBI heating is applied (2.0 MW and 4.5 MW) to drive the toroidal rotation and to heat the ions. For direct electron heating the ECRH system is used. Its heating power is applied in three steps - 0.4 MW, 1.0 MW and 0.75 MW - in addition to 2.0 MW of NBI power. The ECRH power deposition was at $\rho_{pol} \approx 0.4$. The core electron and ion temperatures are comparable, which is favorable when trying to destabilize ETG modes, since the linear ETG threshold scales with the ratio of T_e/T_i [23]. This is why in addition to electron heating, moderate ion heating using NBI is required. The plasma stored energy increases with increasing heating power.

The results obtained for these two different discharge series are presented in the next chapters.

Chapter 6

Perpendicular rotation velocity

6.1 $k_\perp$ dependence of $u_\perp$

Figure 6.1 shows a series of frequency spectra measured at $\rho_{pol} = 0.75$ for different probed $k_\perp$ values (shot numbers 22343-22348). As expected, the Doppler shift f_D increases proportional to the turbulence wavenumber, while the amplitude of the Doppler peak is decreasing. (Note that the amplitudes in the spectra are not corrected for the gain setting and the diagnostic frequency response, hence are not equal to A_G used for calculating the $k_\perp$ spectrum.) The corresponding perpendicular rotation velocities agree within the measurement errors - figure 6.2. The figure shows the radial $u_\perp$ profiles for the first three shots of the second discharge series. The

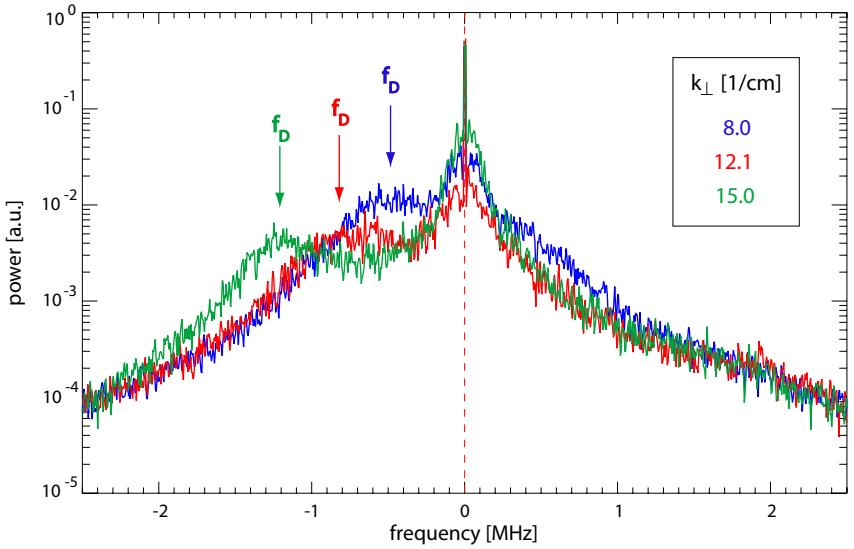

Figure 6.1: Doppler frequency spectra measured for three different $k_\perp$ values at $\rho_{pol} = 0.75$ (2^{nd} series at 1.8 s, shot numbers 22343-22348). The frequency shift f_D increases with $k_\perp$.

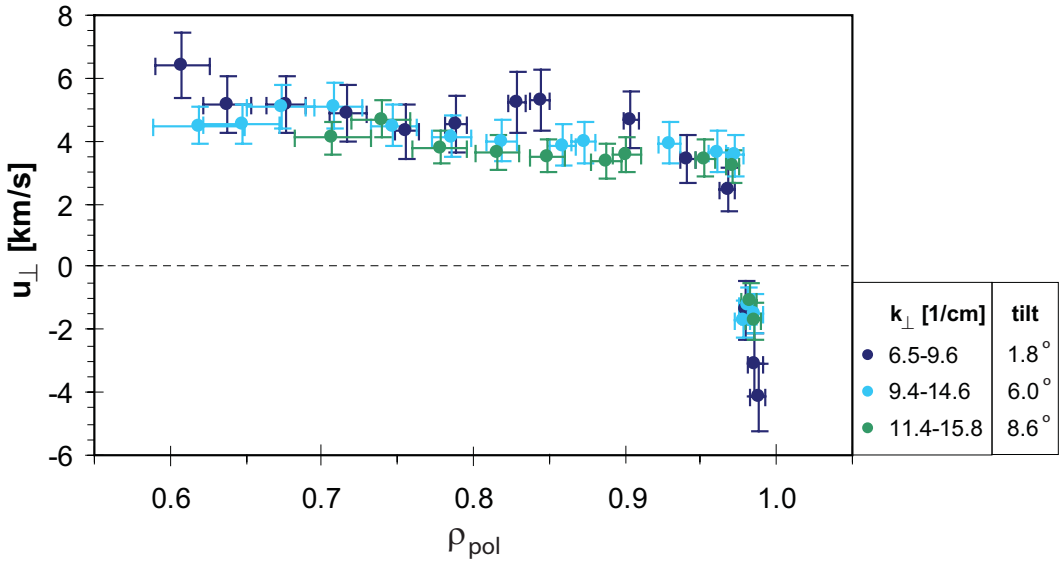

Figure 6.2: Radial $u_\perp$ profiles for the first set of discharges of the 2^{nd} series at 1.8 s. Each profile is measured with a different antenna tilt angle setting giving a different range of the probed $k_\perp$ for each discharge. The profiles agree well within the measurement errors.

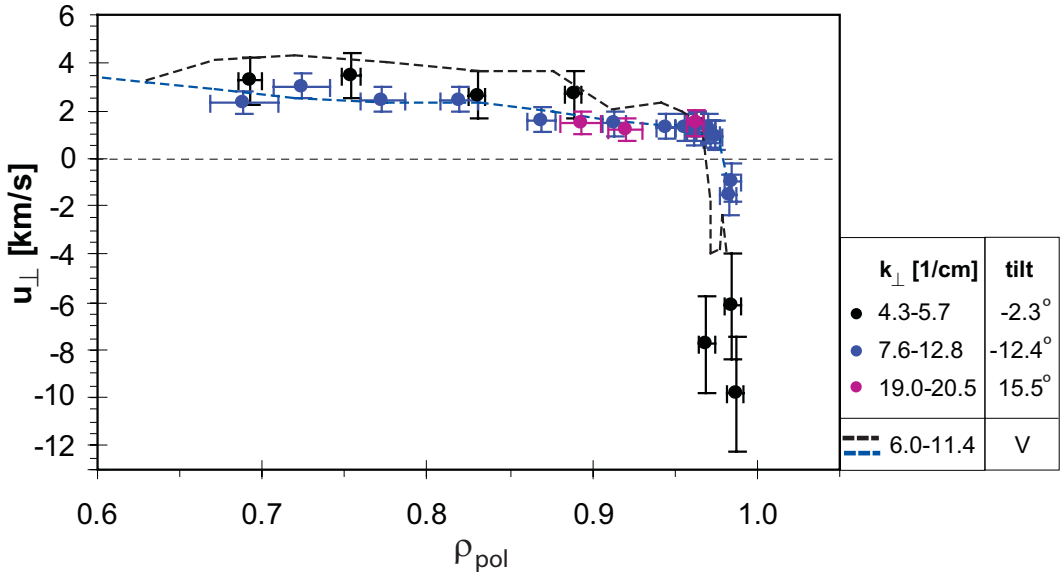

Figure 6.3: Radial $u_\perp$ profiles for the third set of discharges of the 2^{nd} series at 1.8 s. Each profile is measured with a different antenna tilt angle setting including the lowest and highest possible tilt. The corresponding V-band profiles are shown for comparison as dashed curves in respective colors.

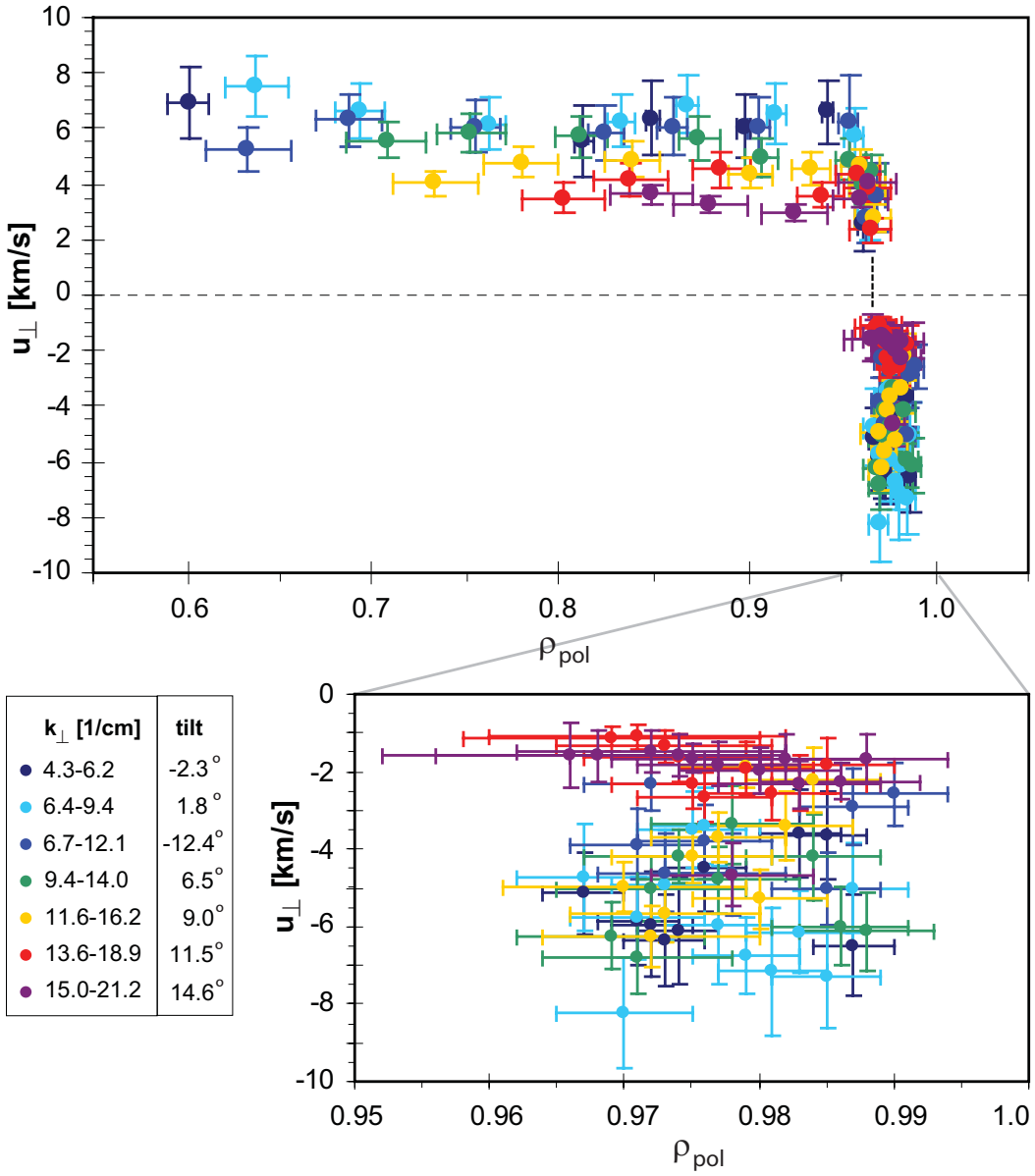

Figure 6.4: Full set of $u_\perp$ profiles for the 1^{st} series at 1.3 s (H-mode). The profiles show a variation of $u_\perp$ with the probed $k_\perp$.

good agreement of the profiles suggests that the phase velocity of the turbulence v_{turb} is either negligible or a nonzero constant in this range of probed $k_\perp$. This argumentation is also supported by another set of $u_\perp$ profiles corresponding to the last three discharges of the second discharge sequence, which are shown in figure 6.3. In the core region, the profiles match within the error bars, although very different $k_\perp$ values are probed in these discharges using the lowest and the highest possible tilt angles for these measurements.

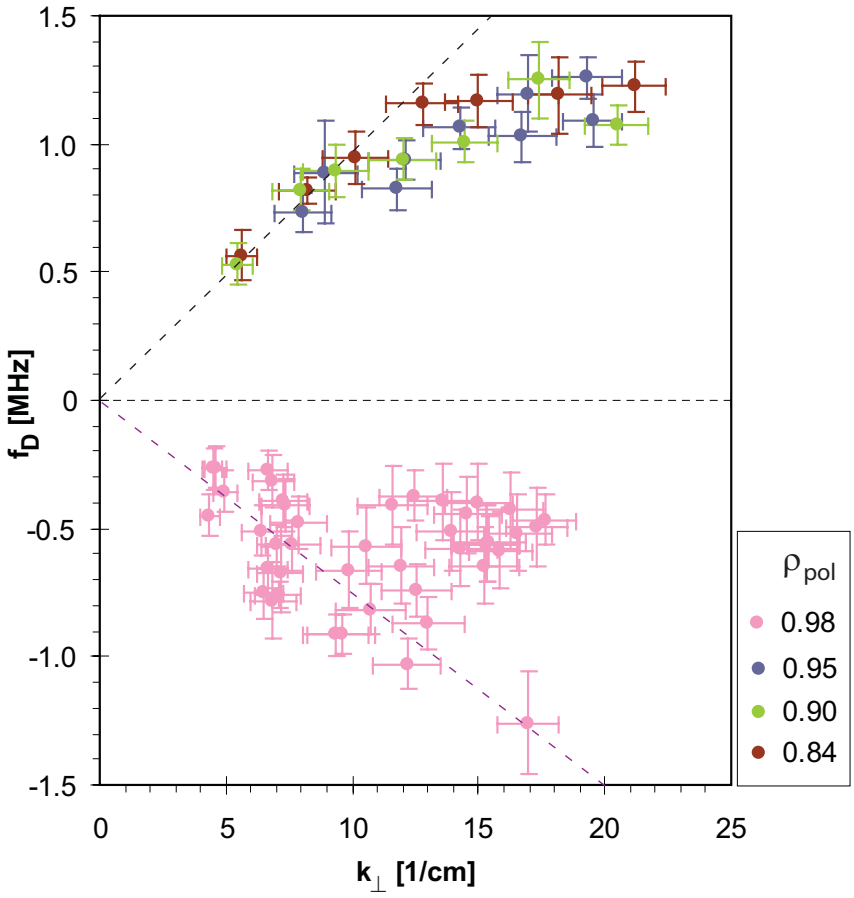

Figure 6.5: Doppler shift frequency versus probed turbulence wavenumber for the 1^{st} series at 1.3 s (H-mode).

(Note that the adverse machine operating conditions during the second discharge series resulted in rather poor reproducibility of the discharges. Consequently, a direct comparison of the profiles is basically restricted to within the three sets of discharges of the second series.)
In figure 6.3 the corresponding profiles from the V-band channel are plotted as dashed curves together with the profiles from the W-band channel for comparison. Once again, the $u_\perp$ profiles obtained by the two different Doppler systems show a remarkably good agreement. Further, one observes that in the core region the black curve is shifted to higher $u_\perp$ values with respect to the blue curve. Taking this fact into account, an excellent match of the three W-band profiles is found. The V-band system is probing a different $k_\perp$-range and hence contributes to the observation that the $u_\perp$ profile is independent of the probed turbulence wavenumber for this set of profile data. However, a significant discrepancy is noted at the plasma edge for the low tilt measurement. Here, the measured W-band profile disagrees with both the corresponding V-band profile and the profiles measured for different tilt angles.

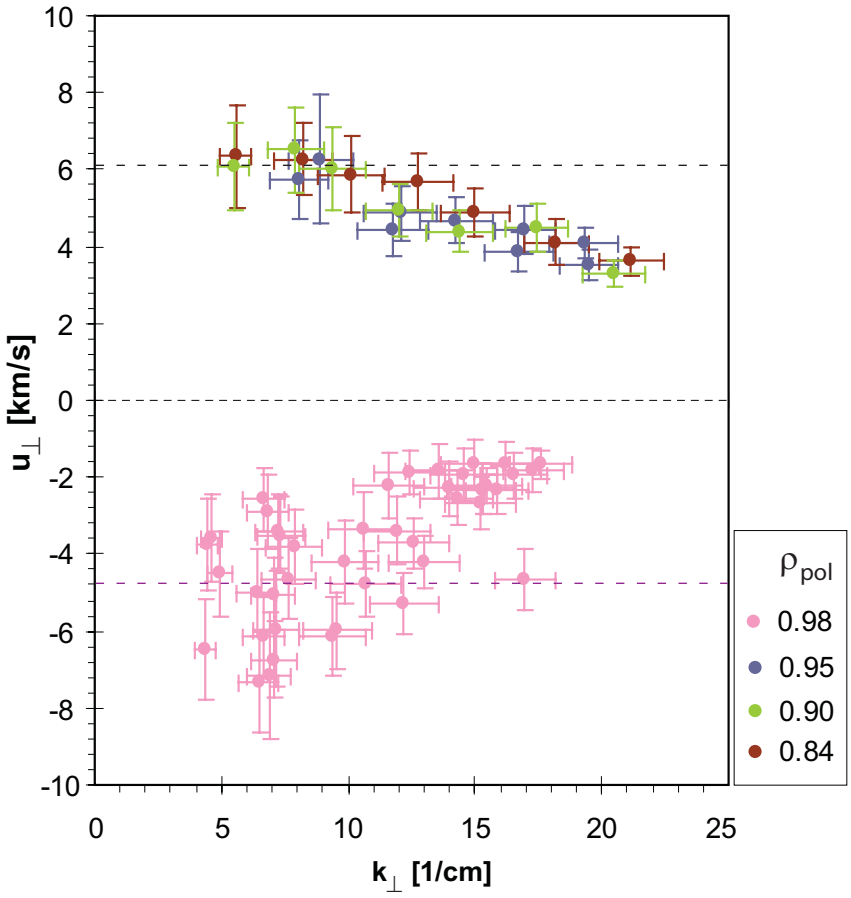

Figure 6.6: Perpendicular rotation velocity versus probed turbulence wavenumber for the 1^{st} series at 1.3 s (H-mode). The dashed lines for the different radial positions correspond to the lines in figure 6.5.

The $u_\perp$ profiles measured during the tilt angle scan of the first discharge series exhibit a different behavior. Figure 6.4 shows the $u_\perp$ profiles for the whole set of different antenna tilts. Although the profiles of adjacent tilt angles generally match within the error bars, a trend of decreasing (absolute) $u_\perp$ values with increasing $k_\perp$ values is observed for this set of H-mode profiles measured at 1.3 s. The variation is substantial in the core region, where the rotation velocity is nearly constant with radius. Here, the measured $u_\perp$ falls from $\approx 6\,\mathrm{km/s}$ when probing low turbulence wavenumbers to $\approx 4\,\mathrm{km/s}$ for high wavenumbers. The difference is thus a factor of about 1.5 and the corresponding profiles (including the error bars) clearly do not agree. In H-mode the extraction of the Doppler shift frequency is more complicated in the edge region, which partly contributes to the larger scatter in the edge data points of the profile. Nevertheless, also here a variation of the $u_\perp$ values with turbulence wavenumber is found. Analyzing another time point (2.2 s) in the H-mode phase of the discharges yields a very similar result (figure 6.9 a).

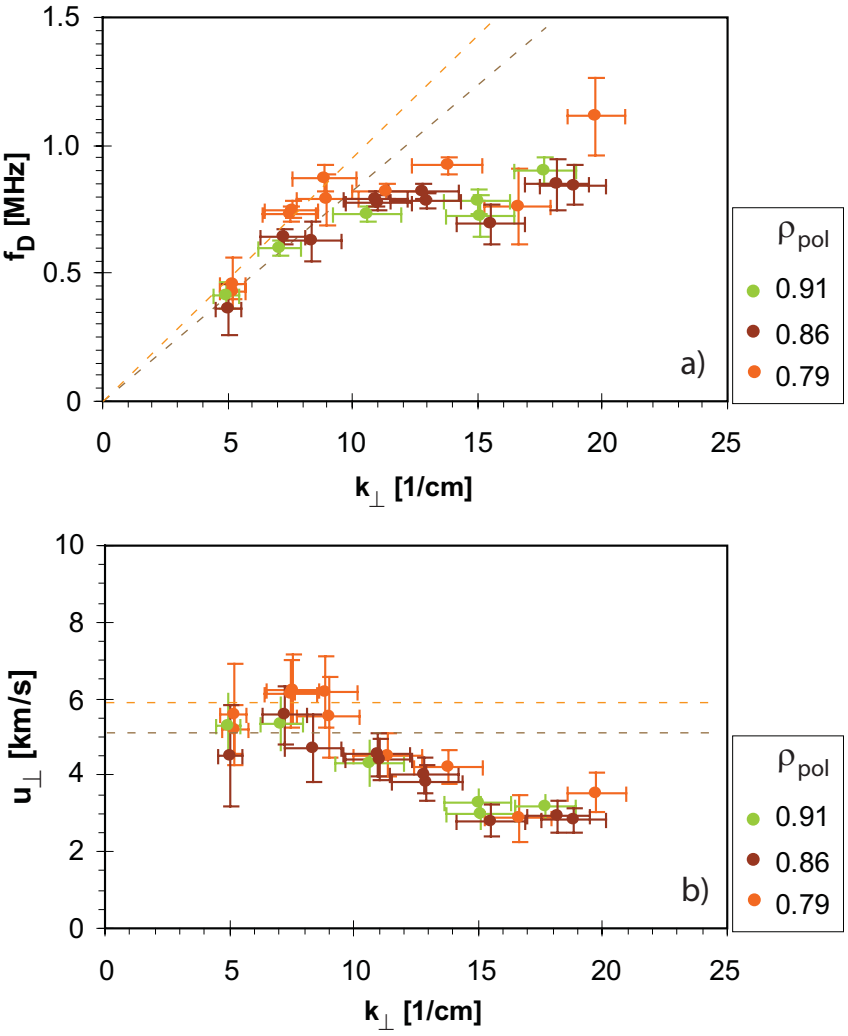

Figure 6.7: Doppler shift frequency (a) and corresponding perpendicular rotation velocity (b) versus probed turbulence wavenumber for the 1^{st} series at 4.1 s (L-mode). The dashed lines in (b) for the different radial positions correspond to the lines in (a).

Another way of presenting the data is to plot the measured Doppler shift frequency versus the probed turbulence wavenumber for different radial positions - figure 6.5. The different curves for the measurement positions inside the pedestal coincide in this example, showing that the perpendicular rotation velocity is roughly constant as a function of radial direction. The $E \times B$ velocity should correspond to a straight line through zero, $f_D/k = v_{E\times B}/2\pi$. For low wavenumbers up to $\approx 10\,\mathrm{cm}^{-1}$ the data points lay on a straight (dashed curves). In this wavenumber range the measured $u_\perp$ seems to be independent of the probed $k_\perp$. A similar result has also been reported in references [65, 56] for this range of turbulence wavenumbers. However, for higher

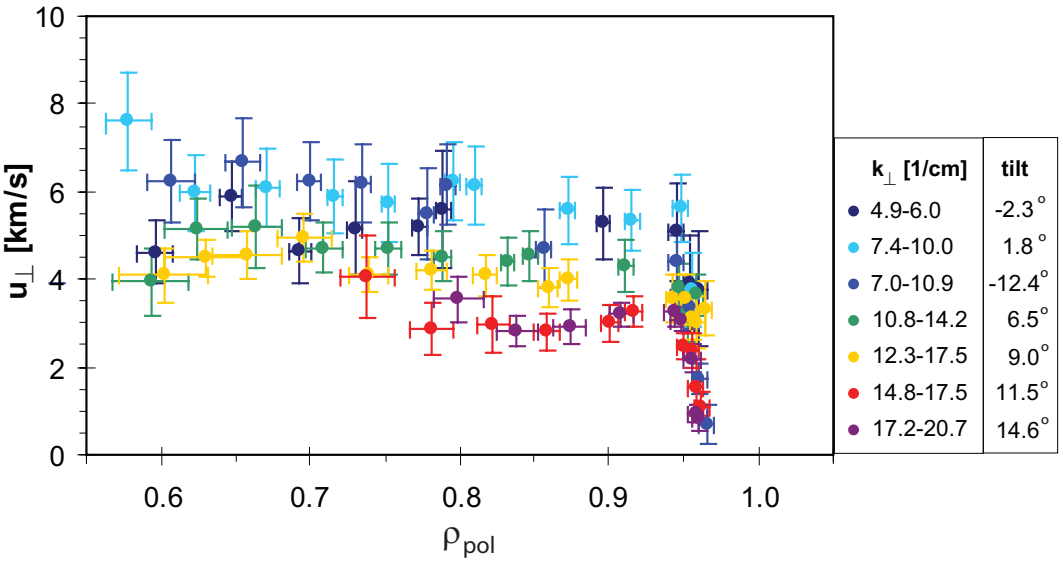

Figure 6.8: Full set of $u_\perp$ profiles for the 1^{st} series at 4.1 s (L-mode). The profiles show a variation of $u_\perp$ with the probed $k_\perp$.

wavenumbers the measured Doppler shift starts to deviate from the linear trend. As a result the (absolute) perpendicular rotation velocity decreases with increasing $k_\perp$ values - figure 6.6.

A similar result is obtained for the L-mode phase of the discharges (first series at 4.1 s). Figure 6.7 a) shows the corresponding f_D versus $k_\perp$ plot. Again, the data points at higher wavenumber values deviate significantly from a linear trend. Above approximately $10\,\mathrm{cm}^{-1}$, f_D saturates but then tends to rise again for $k_\perp \gtrsim 15\,\mathrm{cm}^{-1}$, such that the linear behavior of f_D is interrupted by a plateau at medium $k_\perp$ values. As a consequence, the resulting $u_\perp$ is constant with respect to $k_\perp$ for low turbulence wavenumbers, decreases with $k_\perp$ for medium wavenumbers and seems to be constant again for high wavenumbers, but a factor of 2 lower compared to the $u_\perp$ value for low $k_\perp$. This behavior is very robust with virtually identical results from a second L-mode time point (3.6 s) of the first discharge series.

The full set of $u_\perp$ profiles corresponding to the data of figure 6.7 is shown in figure 6.8. The variation of $u_\perp$ with $k_\perp$ seems to be most dominant in the range $0.95 > \rho_{pol} > 0.85$, i.e. the core region right inside the pedestal. Unfortunately, due to the lower plasma density during the L-mode discharge phase, no edge measurements are available for this set of profile data.

6.2 Velocity components of $u_\perp$

Recalling that the perpendicular rotation velocity is composed of different velocity terms.

$$u_\perp = v_{E\times B} + v_{turb} = v_\phi \frac{B_\theta}{B} - v_\theta \frac{B_\phi}{B} - \frac{\nabla P}{qnB} + v_{turb} \tag{6.1}$$

On ASDEX Upgrade, the charge exchange recombination spectroscopy (CXRS) diagnostic routinely measures the toroidal impurity (C^{6+}) fluid velocity, which is expected to be similar to the ion toroidal fluid velocity. The diamagnetic velocity ($v^* = \nabla P/qnB$) can be determined from measurements of the standard diagnostics, which routinely provide temperature, density ($\nabla P = n\nabla T + \nabla nT$) and magnetic field. Unfortunately, there is no diagnostic available currently which is capable of measuring the poloidal fluid velocity reliably. Previously CXRS has been used for this measurement but the errors typically exceed the measurement itself and hence, the interpretation is very problematic [50]. Figure 6.9 shows a selection of H-mode $u_\perp$ profiles for the first discharge series at 2.2 s (a) and the second discharge series at 3.3 s (b). The toroidal fluid velocity mapped to the perpendicular frame ($v_\phi B_\theta/B$) is plotted for comparison. For the second discharge sequence the NBI heating power was reduced (2.0 MW) compared to the first series (5.0 MW), hence the toroidal rotation is lower. However, in both cases the toroidal velocity exceeds the perpendicular velocity, but for the core region the profiles have the same shape, such that $u_\perp$ follows the toroidal rotation but shifted to lower velocity values. The ion diamagnetic velocity in the core region is about 1.4 km/s for the first series and 0.7 km/s for the second series and may account for part of the difference. (The corresponding impurity diamagnetic velocities are 0.23 km/s and 0.12 km/s, respectively.) The remaining difference between $v_\phi B_\theta/B - v^*$ and the measured $u_\perp$ might be explained by the poloidal rotation velocity term ($v_\theta B_\phi/B$) and/or the phase velocity of the turbulence (v_{turb}). Unfortunately, since there is no direct measurement of either of these two velocities, their contribution to $u_\perp$ has to be deduced from theoretical predictions. The poloidal velocity is calculated in the neoclassical approximation using the NEOART code [85] with experimental T_e, T_i, n_e and v_ϕ profile data and plasma equilibrium reconstruction. In the considered core region ($0.6 < \rho_{pol} < 0.96$, inside pedestal top) the theoretical estimate gives very small poloidal velocities for both discharge series ($v_\theta < -0.1$ km/s for deuterium ions and $v_\theta < 0.5$ km/s for impurity ions). Note that the mapping to the perpendicular frame has only a minimal effect on the value of the poloidal velocity, since $B_\phi/B \approx 1$ and hence $v_\theta B_\phi/B \approx v_\theta$. A rough estimate of the intrinsic phase velocity of the turbulence in the core region can be obtained theoretically from the temperature measurement.

$$v_{turb} \sim F\frac{c_s \rho_s}{R} = F\frac{T_e}{eBR} \tag{6.2}$$

with $c_s = \sqrt{T_e/m_i}$, $\rho_s = \sqrt{T_e m_i}/eB$ and factor F possibly ranging between 0 and 5 [86]. R is the major plasma radius. Equation 6.2 predicts v_{turb} to increase towards the core with maximum values in the order of 1 km/s. Comparing the calculated $E\times B$ velocity (solid line in figure 6.9) with the profiles of the first discharge

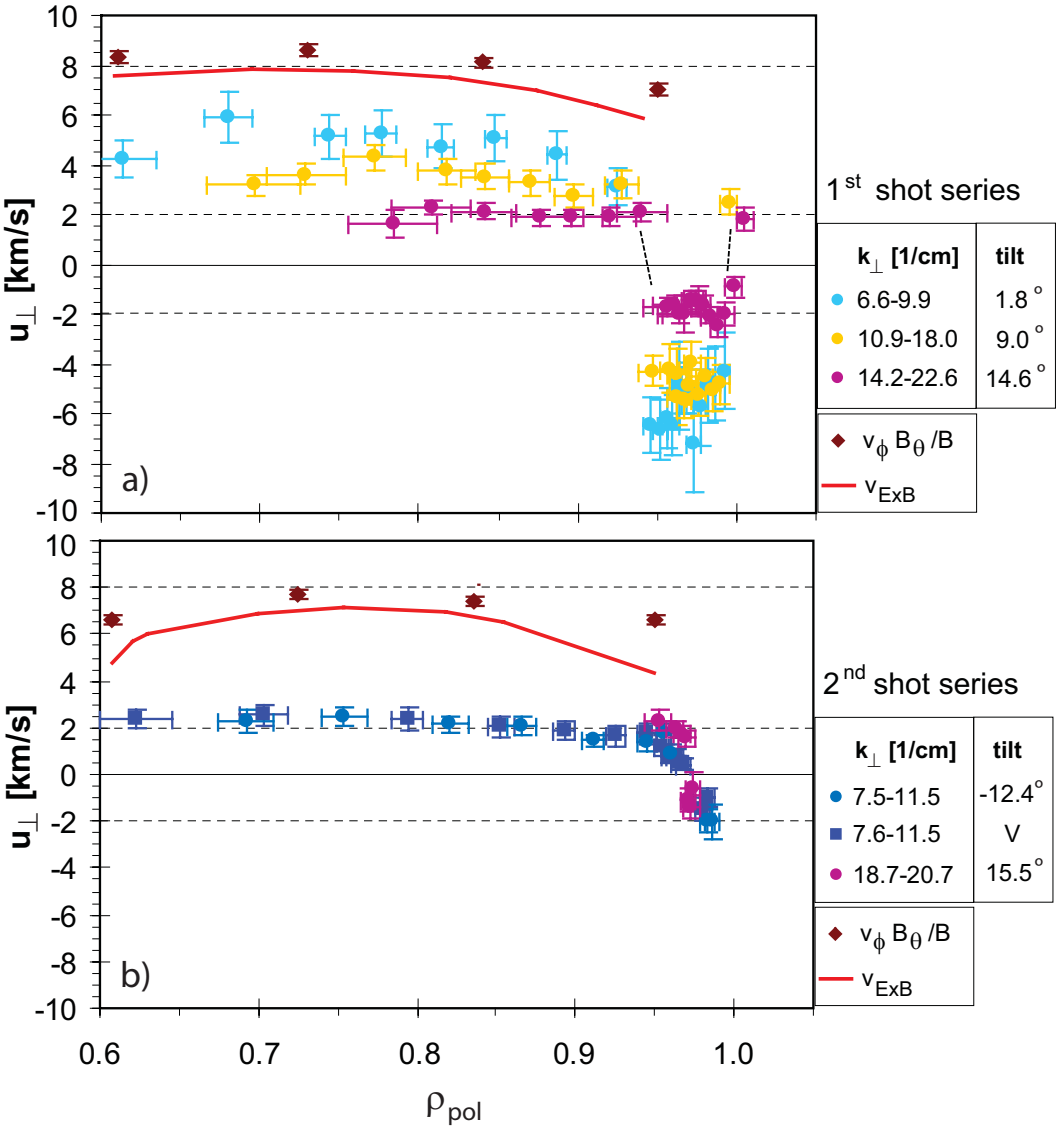

Figure 6.9: Selection of H-mode $u_\perp$ profiles for the 1^{st} series at 2.2 s (a) and the 2^{nd} series at 3.3 s (b). The corresponding (estimate of the) $E \times B$ velocity (solid line) and its toroidal component (diamonds) are shown for comparison.

series shows that $v_{E\times B}$ exceeds the measured $u_\perp$. The disagreement is smallest for the profile probing low turbulence wavenumbers (light blue points). Considering the estimated v_{turb} in the calculation of $u_\perp$ would yield an approach of the curves assuming the turbulence is propagating in the electron diamagnetic direction but no close match. The profiles vary in magnitude from about 6 km/s to 2 km/s with increasing turbulence wavenumbers. Consequently, the profile measured probing high $k_\perp$ values (violet points) differs considerably from the calculated $E \times B$ velocity

($\Delta \sim 4 - 5\,\mathrm{km/s} \gg$ estimated v_{turb}). For the second discharge series no variation of the $u_\perp$ profiles with $k_\perp$ is observed. Independent of the tilt angle setting and the Doppler system (2× W-, 1× V-band channel) a perpendicular rotation velocity of approximately 2 km/s is measured in the core. However, the profiles strongly disagree with the expected $E \times B$ velocity, which is similar to $v_{E\times B}$ of the first discharge series.

6.3 Discussion

In general, a very good agreement between the profiles measured with the established V-band system and the new W-band system is observed when probing similar wavenumbers, validating the proper functionality of the new channel. By scanning the antenna tilt angle a variation of $u_\perp$ with the probed turbulence wavenumber is found for the profiles of the first discharge series (e.g. figure 6.4) but not for the profiles of the second discharge series (e.g. figure 6.3).
It has been shown using full wave simulation that the Doppler shift frequency and thus the determination of $u_\perp$ is very robust for broad ranges of antenna tilt angles and fluctuation levels [79, 80] provided that the probed turbulence wavenumber does not lay in the steep fall-off region of the underlying $k_\perp$ spectrum. Since this condition is not fulfilled for all probed wavenumbers, the observed profile variation with $k_\perp$ may hence be an instrumental characteristic.
For the first discharge series the variation of $u_\perp$ with $k_\perp$ is illustrated in figure 6.6. The discrepancy between the measured $u_\perp$ and the expected linear trend may also be explained by the second velocity component of $u_\perp$, the phase velocity of the turbulence v_{turb}. However, this would mean that, for this example, v_{turb} contributes significantly to the velocity measured by Doppler reflectometry, which may be not consistent with theoretically predicted small turbulence velocities. Furthermore, v_{turb} would be not constant, i.e. would exhibit a nonlinear dispersion relation. Note that a contribution of a constant v_{turb} to the measured $u_\perp$ could not be identified as such by the Doppler measurement alone. From figure 6.6 it becomes not definitely clear whether v_{turb} may be important for low or for high turbulence wavenumbers. Numerical simulations [25, 87] and experimental measurements [88] report nonlinear dispersion relations with a decrease of v_{turb} with increasing turbulence wavenumbers, hence may support a significance of v_{turb} at low $k_\perp$. However, the measured data may also support the assumption that v_{turb} is increasing about linearly with increasing $k_\perp$ above a value of $\approx 10\,\mathrm{cm}^{-1}$, hence may be important for high wavenumbers. Unfortunately, the comparison of the perpendicular velocities with the calculated $E \times B$ velocity also does not yield a definite result in this respect, since the $u_\perp$ profiles all disagree with the estimated $v_{E\times B}$.
This mismatch is also observed for the second discharge series, where the profiles strongly disagree with the calculated $E \times B$ velocity (figure 6.9 b). This is unusual, since normally a good agreement of $u_\perp$ and $v_{E\times B}$ is reported from other experiments, i.e. $u_\perp \approx v_{E\times B}$ [56, 31, 68, 75]. The $u_\perp$ profiles measured with the different tilt angles settings are in agreement, and thus in this discharge sequence $u_\perp$ is observed

to be independent of the probed $k_\perp$. A comparison of $u_\perp$ with the mapped toroidal velocity ($v_\phi B_\theta / B$) suggests that the contribution of $v_\theta B_\phi / B + v_{turb}$ is significantly underestimated by the theoretical predictions. A disagreement between experimental poloidal velocities and neoclassical calculations has been found in other tokamaks, reporting a discrepancy of one order of magnitude in the v_θ values [89, 90]. Following up on this result would yield $v_\theta \approx 4\,\mathrm{km/s}$ instead of the simulated $v_\theta \approx 0.4\,\mathrm{km/s}$ in the core region and the resulting $v_{E\times B}$ curve would indeed be consistent with the measured profiles. Applying the same approach to the data of the first discharge series (figure 6.9 a) would give an $E \times B$ velocity coinciding with the $u_\perp$ profile measured for high $k_\perp$ (violet points).
A more comprehensive discussion of the results will follow in chapter 8.1.

Chapter 7

Turbulence wavenumber spectrum

7.1 General remarks

Using the new Doppler W-band channel, turbulence wavenumber power spectra were measured at various radial positions for different plasma conditions. Figure 7.1 shows spectra of the density fluctuations $|\tilde{n}_e(k_\perp)|^2$ as a function of $k_\perp$ at two radial positions, $\rho_{pol} = 0.86$ and 0.95, obtained with the first discharge series (see section 4.3.4). Note the logarithmic scales. The $k_\perp$ spectra follow a power law $k_\perp^{-\alpha}$

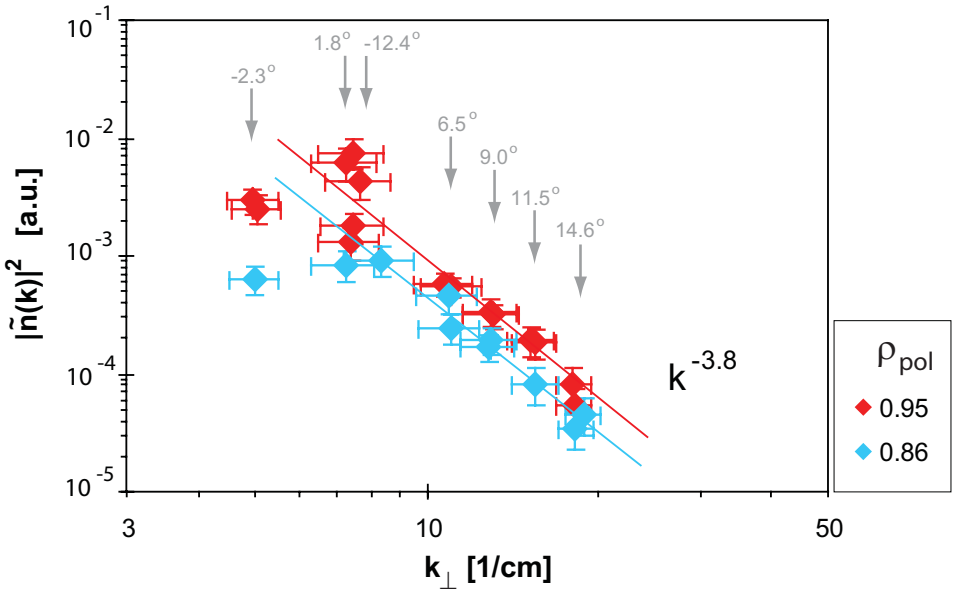

Figure 7.1: Turbulence $k_\perp$ spectra measured during the L-mode phase (4.1 s, 2.5 MW NBI) of the 1^{st} series. Logarithmic plot of the density fluctuations $|\tilde{n}_e(k_\perp)|^2$ as a function of $k_\perp$ for different radial positions ρ_{pol} (inside of pedestal top). The vertical error bars do not account for uncertainties due to geometric effects.

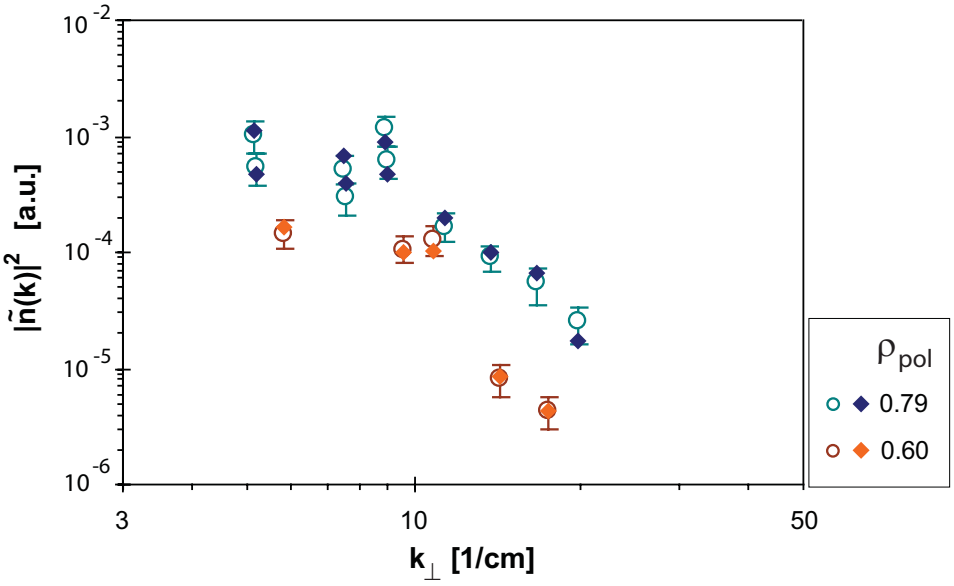

Figure 7.2: Turbulence $k_\perp$ spectra measured during the L-mode phase (4.1 s, 2.5 MW NBI) of the 1^{st} series. Logarithmic plot of the density fluctuations $|\tilde{n}_e(k_\perp)|^2$ as a function of $k_\perp$ for different radial positions ρ_{pol} (inside of pedestal top). Comparison between $k_\perp$ spectra obtained by using A_G and w_G informations (circles) and by using only A_G information (diamonds, spectra scaled).

with a spectral index $\alpha = 3.8$. The error bars given in the figure 7.1 are exemplary for all following $k_\perp$ spectra in this chapter (see section 4.3.5). However, the vertical error bars do not account for the (possible) uncertainties due to geometric effects.

The density fluctuations $|\tilde{n}_e(k_\perp)|^2$ scale directly with the amplitude A_G and width w_G of the Doppler component in the $S(k_\perp, \omega)$ spectrum. Figure 7.2 shows a comparison of $k_\perp$ spectra obtained by using amplitude and width information, $|\tilde{n}_e(k_\perp)|^2 \propto A_G \cdot w_G$ (circles), and using amplitude information only, $|\tilde{n}_e(k_\perp)|^2 \propto A_G$ (diamonds). The corresponding spectra agree within errors for both examples. (Note that the $\diamond$ spectra are scaled with respect to the $\circ$ spectra.) When analyzing the data, the visual impression is that A_G can be extracted reliably even for poorly pronounced Doppler peaks merging into the background, whereas the determination of w_G in such cases is very problematic. The same is true (even for well pronounced peaks), if the amplitude of the Doppler component is more than one order of magnitude smaller than the $m = 0$ component in the measured frequency spectrum. Especially for high tilt angle settings, this is often the case due to the low fluctuation levels in the corresponding spectral ranges. Based on these facts plus the result of figure 7.2, the $k_\perp$ spectra shown in this chapter are obtained by analyzing A_G only.

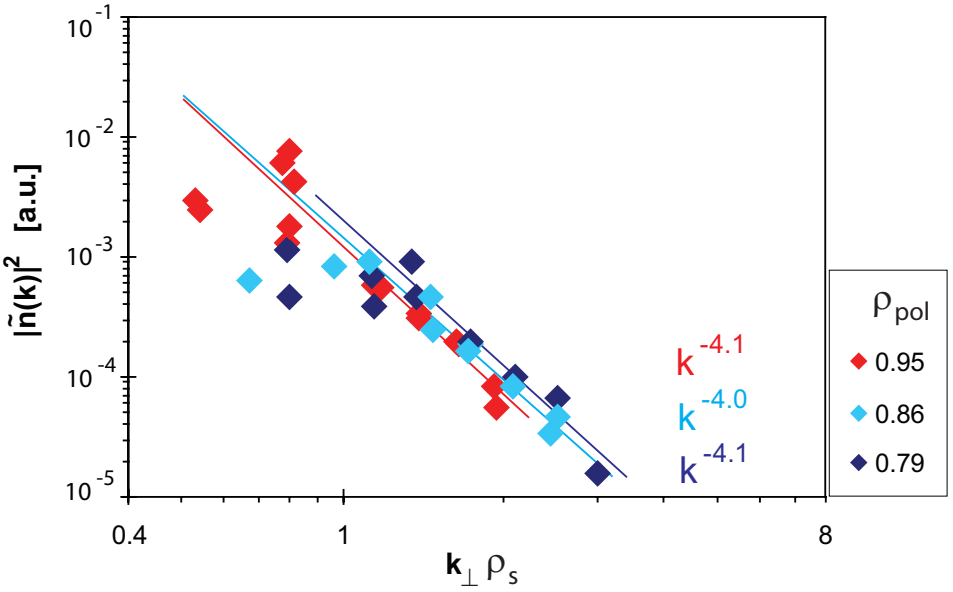

Figure 7.3: L-mode $k_\perp$ spectra (1^{st} series at 4.1 s, 2.5 MW NBI). Logarithmic plot of $|\tilde{n}_e(k_\perp)|^2$ as a function of $k_\perp \rho_s$ for different radial positions ρ_{pol} (inside of pedestal top). A power law $k_\perp^{-\alpha}$ is fitted to the medium/ high $k_\perp$ part of each spectrum.

7.2 Measured $k_\perp$ spectra

The data shown in figures 7.1 and 7.2 are replotted in figure 7.3 in units $k_\perp \rho_s$ (dimensionless) rather than $k_\perp$, where the scale length ρ_s is the ion gyro radius evaluated with the electron temperature (equation 2.17).

$$\rho_s = \frac{\sqrt{m_i T_e}}{eB}$$

Since ρ_s is different at each radial position ($\rho_s = 1.07\,\text{mm}$ at $\rho_{pol} = 0.95$ and $\rho_s = 1.52\,\text{mm}$ at $\rho_{pol} = 0.79$) the spectra shift with respect to each other when plotted against $k_\perp \rho_s$. As a result the wavenumber spectra coincide.
The $k_\perp$ spectra measured during the L-mode phase (4.1 s, 2.5 MW NBI) of the first discharge series cover a spectral range of $k_\perp \rho_s \approx 0.6 - 3.0$. In this range the spectra appear to fall off monotonically following a power law. The fluctuation levels obtained for medium and high tilt angle settings ($-12°$, $6°$ to $15°$) obey a power law with $\alpha = 4.1$, but the fluctuation levels measured for low tilt angle settings ($-2.3°$, $1.8°$) deviate from this power law. Thus, the spectral shape is characterized by a flat part at low turbulence wavenumbers and a fall-off at high wavenumbers with a break point ("knee") at around $0.8 \lesssim k_\perp \rho_s \lesssim 1.3$ depending on the radial position. However, the deviation of the fluctuation levels corresponding to the two lowest tilt angles from the power law seems to be systematic, i.e. it occurs in all measured $k_\perp$ spectra. (This effect is discussed in section 7.3.) As a consequence, the power laws $k_\perp^{-\alpha}$ are fitted to the medium/ high $k_\perp$ part of each spectrum, excluding the data

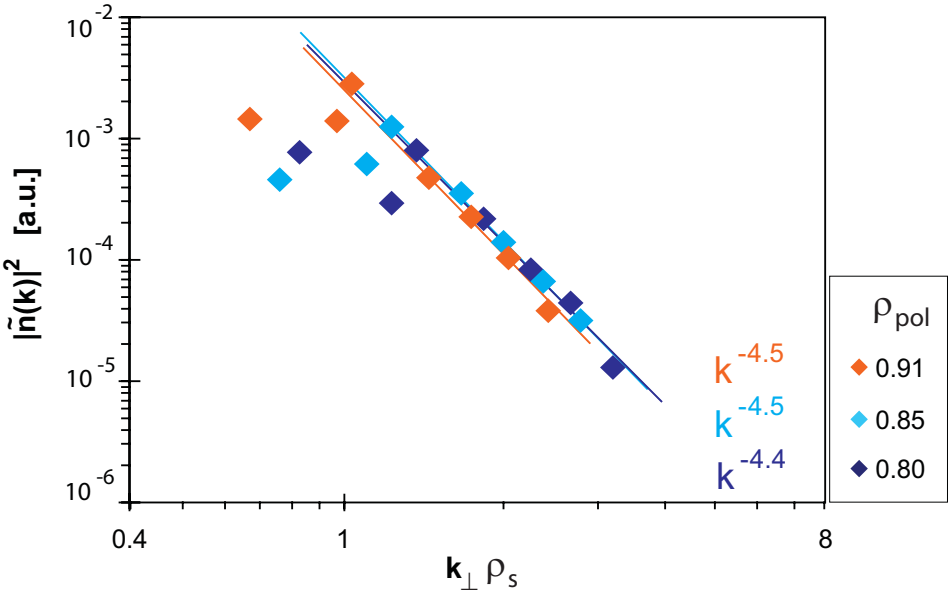

Figure 7.4: L-mode $k_\perp$ spectra (1^{st} series at 3.6 s, 2.5 MW NBI). Logarithmic plot of $|\tilde{n}_e(k_\perp)|^2$ as a function of $k_\perp \rho_s$ for different radial positions ρ_{pol} (inside of pedestal top). A power law $k_\perp^{-\alpha}$ is fitted to the medium/ high $k_\perp$ part of each spectrum.

points measured for the two lowest tilt angle settings. Figure 7.4 shows another set of L-mode $k_\perp$ spectra with power law fits measured at 3.6 s (2.5 MW NBI). Here, α is found to be 4.5, thus slightly higher than in the other case. For both L-mode time points the spectral index is radially constant in the probed ρ_{pol} range showing good validation of the behavior. In H-mode however, the spectral index varies with radius. Figures 7.5 and 7.6 show $k_\perp$ spectra measured during the H-mode phase at 2.2 s and 1.3 s of the first discharge series. With decreasing ρ_{pol} values the spectral fall-off gets steeper in both cases and α changes from 4.4 to 7.0 and from 7.1 to 9.6 respectively. Figure 7.7 shows the measured spectral indexes versus the measurement positions (box symbols). The vertical error bars are determined by the minimal and maximal power laws marginally in agreement with the data. While in L-mode α is constant with radius, it varies almost linearly with radius in H-mode and experiences a large change in the probed radial range. For this set of data α is generally greater in H-mode than in L-mode. Although the absolute values of α differ for the two H-mode cases, the slope is very similar ($\frac{d\alpha}{d\rho_{pol}} \approx 20$).

Figure 7.8 a) shows the fluctuation levels measured in the flat part of the spectra (low $k_\perp \rho_s$) versus the probed radial position (box symbols). Generally, the low $k_\perp$ fluctuation levels increase with ρ_{pol} in the probed core region, i.e. $\rho_{pol} > 0.78$ up to pedestal top at $\rho_{pol} \approx 0.965$. Comparing the fluctuation levels of L-mode and H-mode shows overall higher turbulence levels for L-mode with a steeper increase with radius. The lowest fluctuation levels are measured at H-mode time point 1.3 s,

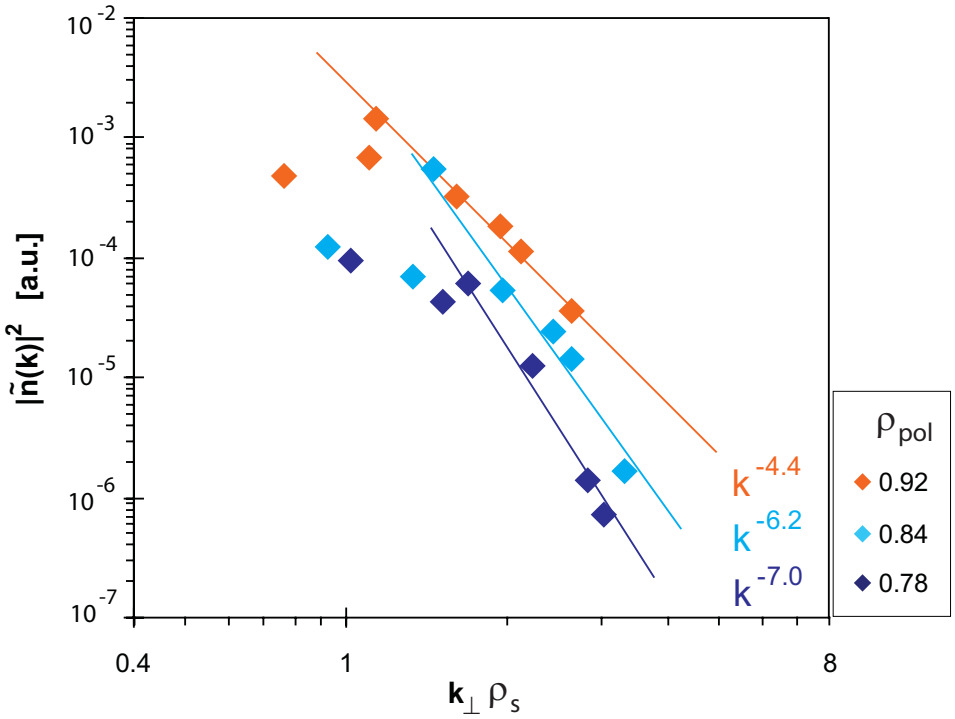

Figure 7.5: H-mode $k_\perp$ spectra (1^{st} series at 2.2 s, 5.0 MW NBI). Logarithmic plot of $|\tilde{n}_e(k_\perp)|^2$ as a function of $k_\perp \rho_s$ for different radial positions ρ_{pol} (inside of pedestal top). A power law $k_\perp^{-\alpha}$ is fitted to the medium/ high $k_\perp$ part of each spectrum.

which showed the highest spectral indexes, whereas the highest fluctuation levels are measured for L-mode associated with the lowest spectral indexes measured. Figure 7.8 b) shows the fluctuation levels measured in the fall-off region of the spectra at $k_\perp \rho_s = 2.2$. (Note the much smaller vertical scale.) Generally, they display very little variation with radius. Only the fluctuation levels measured in H-mode at 2.2 s increase with ρ_{pol}. Near the pedestal top the fluctuation levels for L-mode and H-mode do not differ significantly contrary to the observations made for the flat part of the spectra at low $k_\perp \rho_s$. This may indicate that the turbulence reduction associated with the transition from L-mode to H-mode occurs predominantly at low $k_\perp \rho_s$.

As described above the $k_\perp$ spectra are characterized by a knee point that is found to depend on the radial measurement position. Figure 7.9 shows the position of the spectral knee point (box symbols) in units $k_\perp \rho_s$ versus radial measurement position. Typically, the knee point shifts to higher $k_\perp \rho_s$ values with decreasing radius ranging between $0.8 \lesssim k_\perp \rho_s \lesssim 1.8$. For L-mode lower values are obtained than for H-mode. The position of the spectral knee seem to be correlated with the data point corresponding to tilt angle $-12.4°$ (open circle symbols), also shown in figure 7.9. The knee point generally follows the gradient of this data point, which is

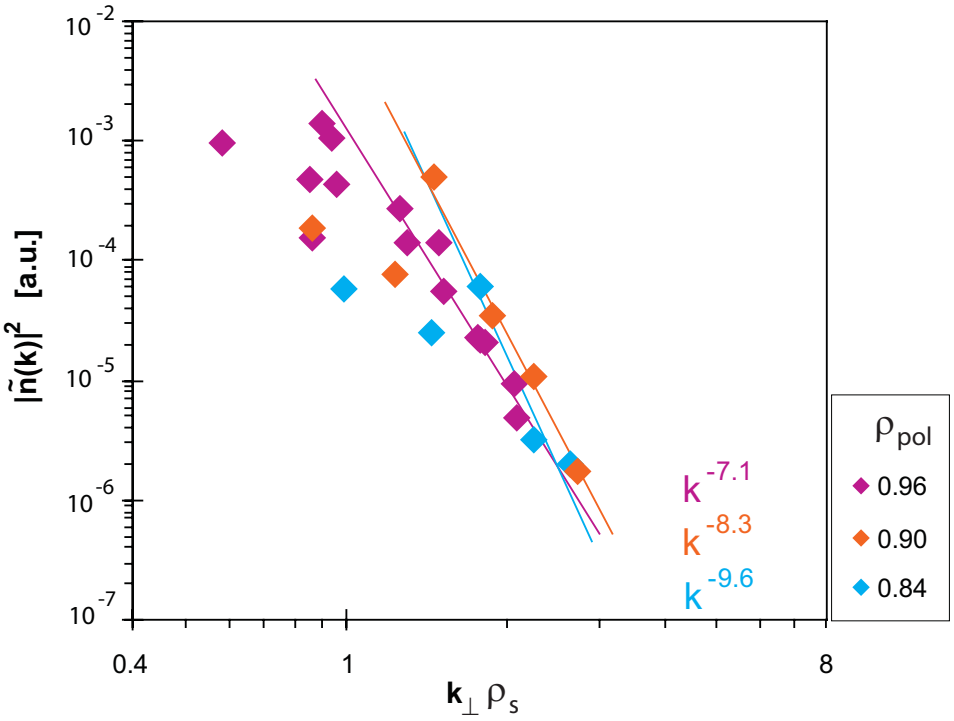

Figure 7.6: H-mode $k_\perp$ spectra (1^{st} series at 1.3 s, 5.0 MW NBI). Logarithmic plot of $|\tilde{n}_e(k_\perp)|^2$ as a function of $k_\perp \rho_s$ for different radial positions ρ_{pol} (inside of pedestal top). A power law $k_\perp^{-\alpha}$ is fitted to the medium/ high $k_\perp$ part of each spectrum.

part of the power law fall-off. Or expressed differently, the flat part of the spectrum is formed consistently by the fluctuation levels measured for the two lowest tilt angle settings ($-2.3°$, $1.8°$).

While the plasma discharges of the first shot series are purely NBI heated (5 MW during the H-mode phase), direct electron heating (1 MW) is applied in addition to 2 MW of NBI power in the second discharge sequence (section 5.3). Wavenumber spectra are measured at 1.8 s (NBI only) and 3.3 s (NBI + ECRH) to study the influence of electron heating on the turbulence $k_\perp$ spectra. Comparing figures 7.10 and 7.11 shows changes in the $k_\perp$ spectra when applying ECRH compared to pure NBI heating, possibly indicating a change in the underlying turbulence properties. The H-mode spectra measured at 1.8 s (figure 7.10) exhibit a similar behavior as the H-mode spectra obtained for the first discharge series. The spectral index varies with radius at a similar rate with $\frac{d\alpha}{d\rho_{pol}} \approx 25$ (figure 7.7, triangle symbols). The values in the core region range from $\alpha = 4.8$ to 6.6 and the $k_\perp$ spectra show a relatively continuous decrease, i.e. they have a clear spectral shape. In the pedestal region, α is generally found to be smaller than in the core. Particularly the spectrum measured at $\rho_{pol} = 0.98$ is comparatively flat in the probed $k_\perp \rho_s$ range. However, the

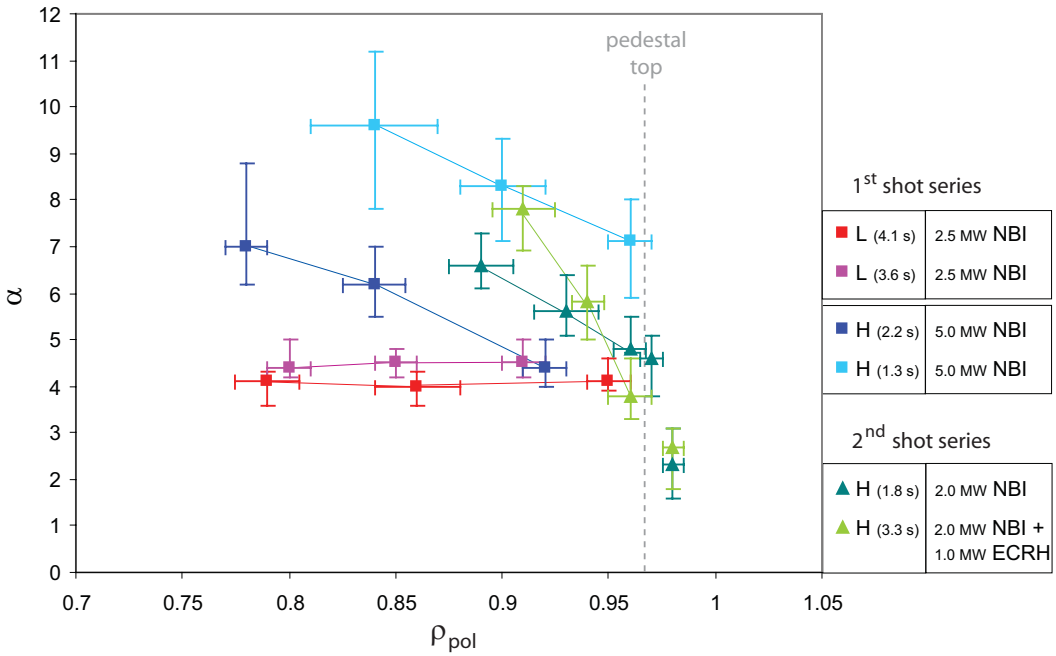

Figure 7.7: Spectral index α versus radial measurement position ρ_{pol} for the full set of measured turbulence $k_\perp$ spectra. The 1^{st} series is labeled with $\square$ and the 2^{nd} series with $\triangle$.

quality of the data is degraded for edge $k_\perp$ spectra due to an increased scatter in the measured fluctuation levels, possibly caused by the unsteady plasma edge conditions (ELM events) distorting the measured raw data. The core $k_\perp$ spectra measured at 3.3 s (figure 7.11) do not show the typical continuous decrease, but exhibit a small bump around $k_\perp \rho_s \approx 2$, which seems to flatten the spectra locally. This effect seems to strengthen with increasing ρ_{pol}, i.e towards the edge. While the spectrum at $\rho_{pol} = 0.91$ has the usual shape, the spectrum at $\rho_{pol} = 0.96$ has a plateau (complicating the fit of a power law) and finally the spectrum at $\rho_{pol} = 0.97$ has a pronounced bump at $k_\perp \rho_s \approx 2.4$ plus a large scatter (impeding a reliable power law fit to the medium/ high $k_\perp$ part of the spectrum). Unfortunately, the $k_\perp \rho_s$ coverage of the edge $k_\perp$ spectra is not sufficient to show the trend of the spectra at higher $k_\perp \rho_s$ values. Thus it remains unclear, if the fluctuation levels decrease at the higher sales ($k_\perp \rho_s \approx 3$) as observed for the core $k_\perp$ spectra. Nevertheless, comparing the spectra measured at the two different time points of the second discharge series, particularly at $\rho_{pol} = 0.97$, suggests that the turbulence changes its characteristics with the different heating schemes. This can be also seen in figure 7.7. Although the radial variation of α is linear at time point 3.3 s (NBI + ECRH) as observed for the other H-mode cases (NBI only), the slope is significantly steeper (factor three) with $\frac{d\alpha}{d\rho_{pol}} \approx 79$.

In the probed core region the fluctuation levels at low $k_\perp \rho_s$ measured for time point

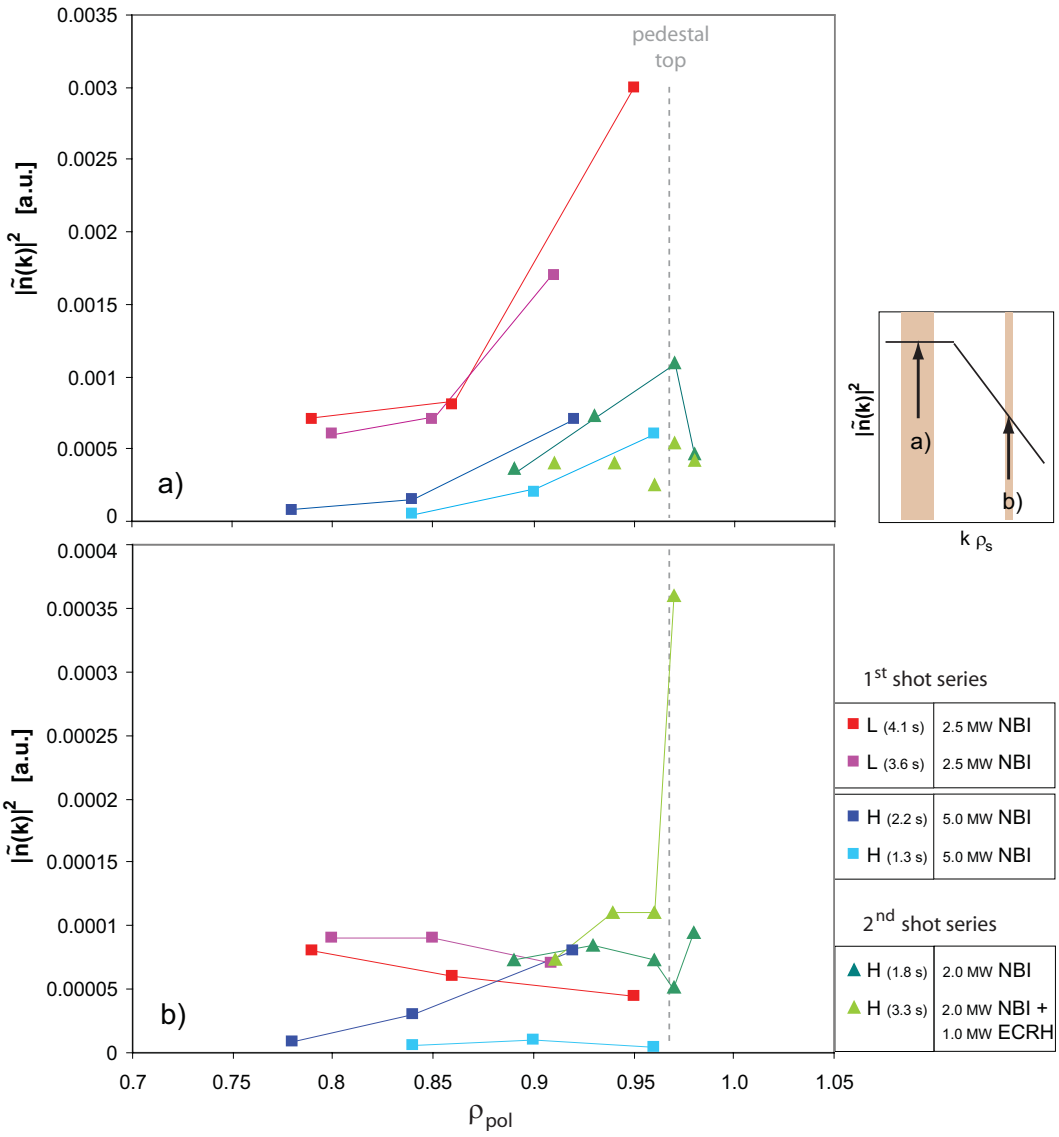

Figure 7.8: Fluctuation levels measured at (a) low $k_\perp \rho_s$ (flat part of the spectra) and (b) high $k_\perp \rho_s$ (fall-off region, $k_\perp \rho_s = 2.2$) versus radial measurement position ρ_{pol} for the full set of measured turbulence $k_\perp$ spectra. Note the different vertical scales.

1.8 s (NBI only) increase with radius as observed for the first discharge series (figure 7.8 a). In the pedestal region they then drop significantly. The measured values are also in agreement with the H-mode data of the first discharge series. In contrast, the fluctuation levels measured for time point 3.3 s (NBI + ECRH) are relatively small and show a roughly constant behavior with radius plus no significant drop in the pedestal region. The fluctuation levels measured in the fall-off region of the spectra also differ for the two time points (figure 7.8 b). Here, the fluctuation levels

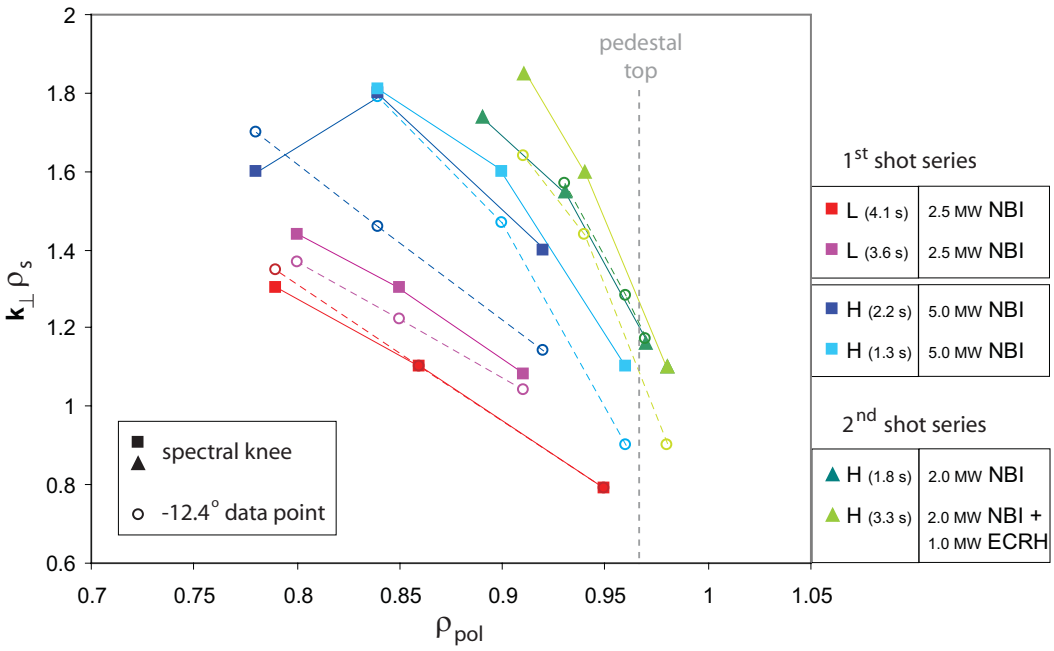

Figure 7.9: Position of the spectral knee point (□, △) and the data point corresponding to tilt angle $-12.4°$ (○) in units $k_\perp \rho_s$ versus radial measurement position ρ_{pol} for the full set of measured turbulence $k_\perp$ spectra.

corresponding to a purely NBI heated plasma (1.8 s) display only small changes with radius. When applying NBI plus ECRH (3.3 s) the fluctuation levels are slightly higher inside the pedestal top and show a sharp increase to a substantially higher value in the pedestal region. This very high value results from the pronounced bump at high $k_\perp \rho_s$ observed in the corresponding wavenumber spectrum. Note that the overall turbulence level (i.e. $|\tilde{n}(k_\perp)|^2$ integrated over all $k_\perp$) does not increase, since the enhanced fluctuation amplitude appears at large wavenumbers contributing only little due to the comparatively low fluctuation levels at high $k_\perp$ (note the different vertical scales in figure 7.8).

The shift of the spectral knee with radial measurement position is also observed for the second discharge series as shown in figure 7.9 (triangle symbols). The position of the spectral knee point is found to range between $1.1 \lesssim k_\perp \rho_s \lesssim 1.9$ in a relatively small radial region ($0.89 < \rho_{pol} < 0.98$) showing a steep decrease with radius. The obtained values are slightly higher than for the H-mode data of the first discharge series and they also seem to show a correlation with the data point corresponding to tilt angle $-12.4°$ (open circle symbols).

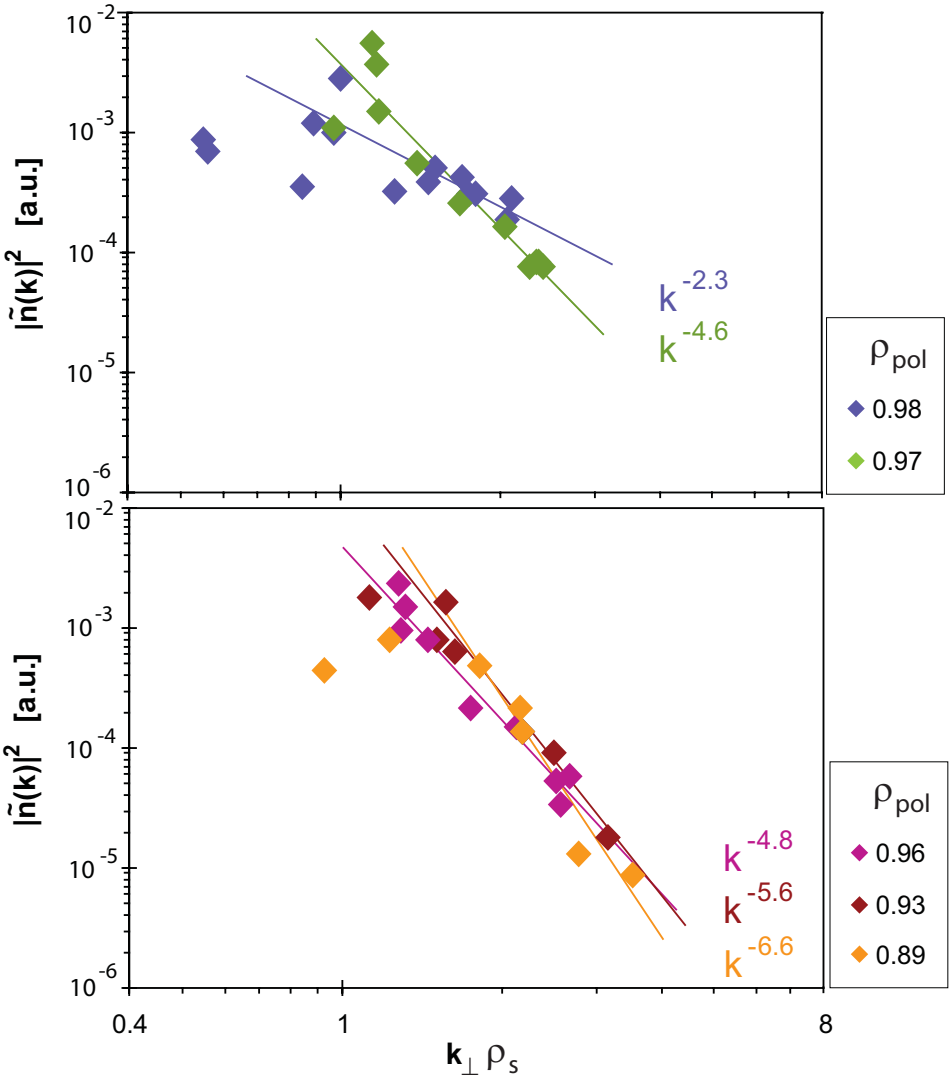

Figure 7.10: H-mode $k_\perp$ spectra (2^{nd} series at 1.8 s, 2.0MW NBI only). Logarithmic plot of $|\tilde{n}_e(k_\perp)|^2$ as a function of $k_\perp \rho_s$ for different radial positions ρ_{pol} (top: pedestal region, bottom: inside of pedestal top). A power law $k_\perp^{-\alpha}$ is fitted to the medium/ high $k_\perp$ part of each spectrum.

7.3 Discussion

Measurements of the turbulence $k_\perp$ spectrum performed on other tokamak experiments generally yield spectral indexes of 3-4 for ohmic and L-mode discharges [65, 35, 91, 17, 33]. The L-mode $k_\perp$ spectra presented in this thesis have slightly higher spectral indexes, typically between 4.0 and 4.5. The small difference may be due to the missing correction for the variation of the scattering efficiency with tilt angle. As mentioned above, quantitative corrections are not available at present,

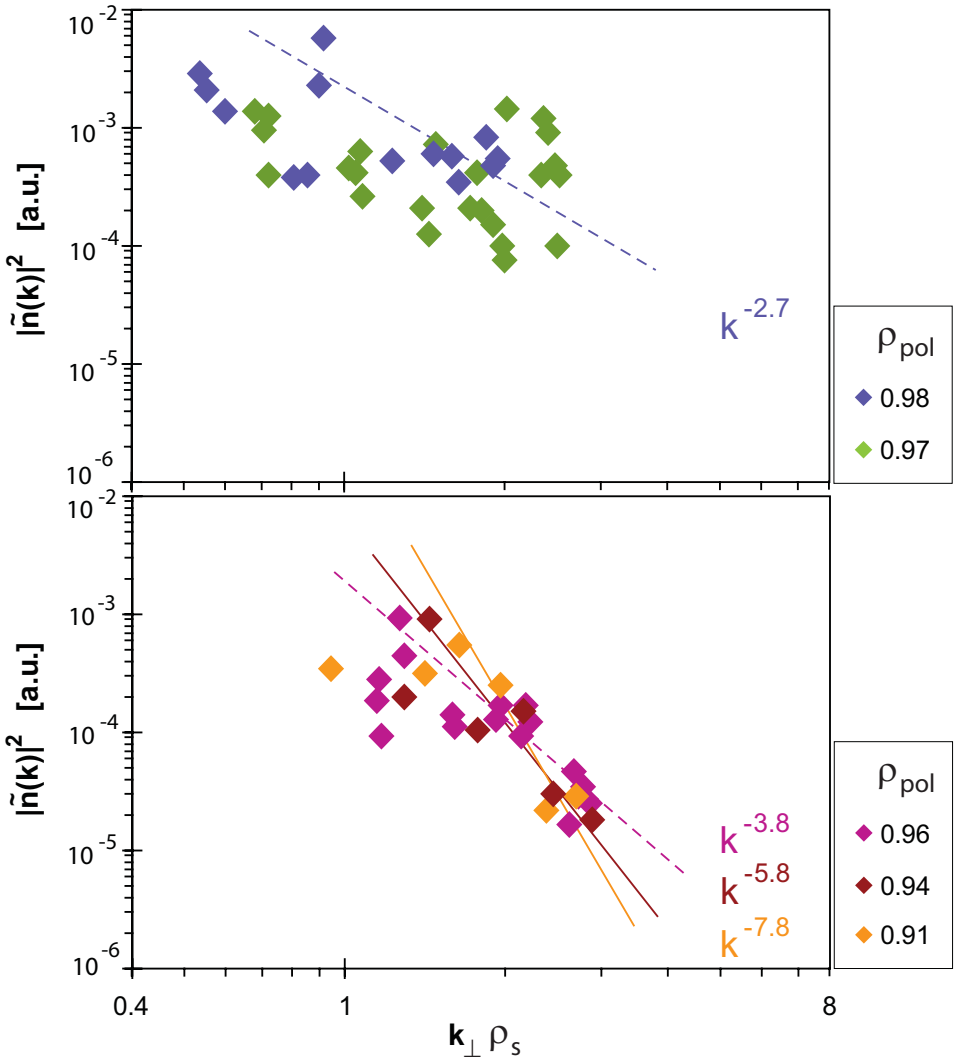

Figure 7.11: H-mode $k_\perp$ spectra (2^{nd} series at 3.3 s, 2.0 MW NBI + 1.0 MW ECRH). Logarithmic plot of $|\tilde{n}_e(k_\perp)|^2$ as a function of $k_\perp \rho_s$ for different radial positions ρ_{pol} (top: pedestal region, bottom: inside of pedestal top). A power law $k_\perp^{-\alpha}$ is fitted to the medium/ high $k_\perp$ part of each spectrum.

but a qualitative prediction is nevertheless possible: the larger the probed $k_\perp$ value, i.e. the larger the tilt angle, the larger also the corresponding correction factor. Consequently, the measured fluctuation levels at high $k_\perp$ would increase when the correction is taken into account and this would result in a flattening of the spectral shape, i.e. α would decrease. Hence, the spectral indexes presented here (figure 7.7) can be regarded as an upper limit. While in L-mode plasmas α is found to be constant with radius, it increases towards the core in the probed radial region for H-mode plasmas indicating a change in the character of the turbulence. A variation

of α with radius has been reported in previous turbulence measurements in L-mode probing the full radial region ($0.0 > \rho_{pol} > 0.88$) [92]. However in the radial range $\rho_{pol} > 0.63$ the measured spectral indexes ($\alpha \sim 4.2 - 4.4$) were found to be roughly constant consistent with the measurements presented here.

While the behavior of the high $k_\perp$ part of the spectrum seems to be relatively distinct, the behavior of the low $k_\perp$ part requires careful considerations. The fluctuation levels measured using shallow tilt angles ($-2.3°$, $1.8°$) deviate from the power law fitted to the fluctuation levels obtained for the higher tilt angles. The resulting spectral shape is flat at low $k_\perp \rho_s$ and decreases according to a power law at higher $k_\perp \rho_s$ with a knee point around $0.8 \lesssim k_\perp \rho_s \lesssim 1.9$, which shifts with the radial measurement position. This basic shape is generic for turbulence wavenumber spectra and seen in many experiments [57, 93, 92, 91]. However, the position of the spectral knee point is generally found at $0.1 \lesssim k_\perp \rho_s \lesssim 1.1$. ($k_\perp \rho_s \sim 1.1$ reported only for deep core region $r/a < 0.5$ [92].) The measured values shown in figure 7.9 are significantly higher than generally expected in the probed radial region. Further, the flat part of the wavenumber spectra is formed consistently by the fluctuation levels measured for the tilt angle settings $-2.3°$ and $1.8°$. Hence, one may not exclude a diagnostic effect causing the systematic deviation from the power law. Various possibilities may be considered. The full wave simulations account for the effects of higher Bragg order scattering on the scattering efficiency. If a significant part of the launched microwave power is scattered into higher Bragg orders ($m = -2, -3, ...$), then less power is received at the backscattered order ($m = -1$). The simulation results show qualitatively that this effect is important for low tilt angles at high fluctuation levels. It is important to also include the contribution of forward scattering effects in the correction factors. Possibly, multiple forward scattering processes degrade the detected backscattered power level for low tilt angle settings. If the forward scattering and/or the higher order scattering contribution were substantial, then possibly all data points would follow the power law when corrected for geometric effects. Another alternative could be that the discrepancy is due to an inherent feature of the steerable antenna configuration. In this case, a more detailed antenna characterization would be required (comprehensive tests, calibration measurements) to examine the antenna response and to deduce possible calibration factors.

The various arguments will be discussed in chapter 8.2 in the context of a more detailed discussion of the experimental results.

Chapter 8

Discussion of experimental results

Doppler measurement
With a tilted antenna line of sight Doppler reflectometry measures a Doppler shift in the returned frequency spectrum due to transverse (mostly poloidally) propagating plasma density fluctuations. The measured quantity - the spectral Doppler shift - is obtained for a certain tilt angle and launch microwave frequency determining the local measurement position in the plasma. The Doppler shift appears in the frequency spectrum as a Gaussian peak due to the finite wavenumber sensitivity $\Delta k_\perp$ of the diagnostic (see below). From a Gaussian fit curve, $A_G exp[-\frac{(f-f_D)^2}{w_G^2}]$, to the spectral Doppler component the Doppler shift frequency f_D, the peak amplitude A_G and the peak spectral width w_G is determined. f_D is directly proportional to the perpendicular rotation velocity $u_\perp$ of the density turbulence moving with the bulk plasma (equation 4.10). $A_G \cdot w_G$ is directly proportional to the spectral power density $S(k_\perp)$ at the wavenumber $k_\perp$ (equation 4.16). Note that a prerequisite for the Doppler measurement is the presence of fluctuations or turbulence to backscatter from. Both, simulation studies and experimental observations indicate a critical threshold in the turbulence amplitude below which a Doppler measurement is not possible [94, 31].
The antenna characteristics and the curvature of the cutoff layer determine the instrument response in the wavenumber space $\Delta k_\perp$. The diagnostic is sensitive to a (small) range of turbulence wavenumbers centered around the nominal $k_\perp$ that is defined by the antenna tilt angle via the Bragg condition (equation 4.6). Thus, $\Delta k_\perp$ principally determines the spectral width of the Doppler peak w_G, i.e. the narrower the wavenumber sensitivity the narrower the Doppler peak ($\Delta k_\perp \propto w_G$). The best $\Delta k_\perp$ possible with a spot radius w of the microwave beam at the cutoff can be calculated according to reference [95] via

$$\Delta k_\perp = \sqrt{2} \cdot \frac{2}{w} \cdot \sqrt{1 + \left(\frac{w^2 k_0}{\rho_c}\right)^2} \tag{8.1}$$

where ρ_c is the effective curvature radius within the spot, which reduces to the cutoff layer curvature for plane wave fronts. For the steerable antenna the calculated spectral resolution $(\Delta k_\perp / k_\perp) = (w_G / f)$ varies between $1.8 < (\Delta k_\perp / k_\perp) < 2.1$ for

low tilt angles and between $0.13 < (\Delta k_\perp / k_\perp) < 0.16$ for high tilt angles depending on the probed radial position (i.e. launched frequency). Turbulence $k_\perp$ spectra were obtained in the radial region $0.78 < \rho_{pol} < 0.98$, for which the wavenumber sensitivity is calculated according to equation 8.1 to be roughly constant with $\Delta k_\perp \sim 2.3\,\mathrm{cm}^{-1}$ for all used tilt angles. A comparison between $k_\perp$ spectra analyzed with $S(k_\perp) \propto A_G \cdot w_G$ and with only $S(k_\perp) \propto A_G$ (figure 7.2) showed a good agreement of the corresponding spectra and thus $A_G \propto A_G w_G$, i.e. in the probed ρ_{pol} range w_G is indeed found to be roughly constant for the various tilt angles. Hence, the turbulence wavenumber spectra presented in this thesis are evaluated according to $S(k_\perp) \propto A_G$ justified by the experimental conditions and results. The $k_\perp$ sensitivity deduced from the measured spectral width of the Doppler peak, i.e. deduced from the raw data, $\Delta k_\perp = k_\perp (w_G / f_D)$, is significantly larger (factor 2) than the estimated $\Delta k_\perp$ from formula 8.1 possibly indicating turbulence broadening of the spectrum [96].

Influences on measurement
There are various effects that could in principle influence the Doppler measurements.

i) Spectral roll-off
Using full wave simulation it has been shown that the measured Doppler shift frequency is very robust for broad ranges of antenna tilt angles and fluctuation levels, if the underlying turbulence wavenumber spectra is broad, i.e. includes $k_\perp$ to allow for Bragg backscattering [79, 80, 97]. Da Silva reported that even if the wavenumber for the occurrence of linear Bragg backscattering, $k_\perp$, is not present in the wavenumber spectrum, non-linear Bragg backscattering can occur yielding the same Doppler shift frequency for high levels of turbulence [97]. For low turbulence levels however the frequency shift is smaller than the Doppler frequency shift for linear Bragg backscattering. In this case, $u_\perp$ calculated from the frequency shift would be underestimated. Blanco reported a more severe impact of the spectral width of the turbulence $k_\perp$ spectrum on the measured Doppler shift frequency [80], similar to the results obtained by Conway with the physical optics model [94]. According to the full wave simulation results the measured frequency shift agrees with the nominal Doppler shift only when probing a region of the $k_\perp$ spectrum with nearly constant intensity. If the amplitude of the turbulence $k_\perp$ spectrum changes within the wavenumber range probed by the diagnostic, i.e. $k_\perp \pm \Delta k_\perp$ (instrument response in $k_\perp$ space), which should be the case when probing a $k_\perp$ in the spectrum roll-off region, then the measured frequency shift and hence $u_\perp$ would be significantly underestimated. This results from the different turbulence amplitudes at low (i.e. $k_\perp - \Delta k_\perp$) and high (i.e. $k_\perp + \Delta k_\perp$) wavenumbers. The response of the diagnostic should be lower for high wavenumbers, since here the fluctuation levels are lower. Consequently, the amplitude of the Doppler structure should be depressed in the corresponding high frequency range and thus the center frequency of the structure should be skewed towards a lower frequency, which is detected as the shift frequency.

ii) Bragg orders
The launched microwave beam is scattered not only in the $m = -1$ Bragg order but also in higher Bragg orders ($m = -2,\ m = -3,\ ...$) for a particular $k_\perp$, which are generally not seen by the receive antenna. Hence, the microwave power scattered into these higher orders is lost. Full wave simulations results indicate that higher Bragg order scattering becomes important for low tilt angles at high fluctuation levels [83]. This has an effect on the Bragg backscattering efficiency, since less signal power is received at the backscattered order ($m = -1$), if a significant part of the launched power is scattered into higher orders. Consequently, higher order scattering could influence the measured $k_\perp$ spectrum.
According to the Bragg condition $k_\perp = mk = 2k_0N$ for backscattering, higher scattering orders ($m = -2,\ m = -3,\ ...$) associated with lower k values ($k = \frac{1}{2}k_\perp,\ \frac{1}{3}k_\perp,\ ...$) would contribute to the same Doppler shift in the received frequency spectrum for any fixed tilt angle [56]. Physical optics simulations show that the dominant $m = -1$ Bragg order peak saturates with increasing turbulence level and the $m = -2$ Bragg order peak becomes stronger [78]. In cases where the main $m = -1$ order signal is weakened due to strong roll-off in the turbulence $k_\perp$ spectrum (high spectral index), the contribution from the $m = -2$ order at $\frac{1}{2}k$ may dominate due to the higher turbulence level in the corresponding spectral range. A possible contribution from power scattered in higher orders by fluctuations with $\frac{1}{2}k,\ \frac{1}{3}k$, etc. to the received signal has no influence on the measured $u_\perp$, since the lower k value cancels the higher scattering order m, i.e. all scattering orders yield the same $u_\perp$. However, it would cause distortion in the measured wavenumber spectrum, since the detected high turbulence level corresponding to $\frac{1}{2}k$ may be misattributed to k.

iii) Antenna side lobes
An antenna radiation pattern usually has side lobes which may create additional Doppler peaks in the frequency spectrum [78]. A side lobe signal is associated with a different $k_\perp$ than the main lobe signal due to the different incidence angle of the side lobe. In addition to $k_\perp$ also the measurement position changes with the tilt angle and hence the side lobe signal differs in more than one aspect from the real main lobe Doppler signal. If the latter is lost, e.g. due to low turbulence levels, and the side lobe peak is misinterpreted as the main Doppler peak, both the measured $u_\perp$ profiles and the $k_\perp$ spectra would be corrupted. The measured turbulence levels may in this case be misattributed to too high or too low $k_\perp$ values thus distorting the $k_\perp$ spectrum and the error in the $u_\perp$ profiles may result from the error in the radial measurement position and the associated Doppler shift. Furthermore, $u_\perp$ would be calculated with the $k_\perp$ corresponding to the main lobe such that even in the case of radially constant Doppler shifts $u_\perp$ would be false.

iv) Scattering efficiency
As already mentioned in section 4.3.4 full wave simulation show that the Bragg backscattering efficiency varies with the antenna tilt angle [79, 80, 81]. Generally, the received backscattered power decreases with increasing tilt. Obviously, this influences the measured $k_\perp$ spectrum, i.e. changes the spectral index α. If the

measured spectra were corrected for the backscattering efficiency variation, α would generally decrease. Preliminary simulation results suggest that this decrease should be roughly similar for all spectral indexes (considering the relevant tilt angles) in the probed radial region [83]. The $u_\perp$ profiles in contrast should remain mostly unaffected.

v) Instrumental failure
A malfunction of the steerable antenna, i.e. wrong setting of the tilt angle, would grossly impact on both the $u_\perp$ profiles and the $k_\perp$ spectra, since the measured Doppler peaks would be associated with wrong turbulence wavenumbers and radial measurement positions. A more subtle instrumental failure, e.g. a significant change in the antenna send and receive radiation pattern with the tilt angle due to blocking or shielding of part of the radiation by the antenna housing could also influence the measurements in an unexpected way.

vi) Turbulence phase velocity
The turbulence phase velocity appears always in the $u_\perp$ measurement ($u_\perp = v_{E\times B} + v_{turb}$). Depending on the plasma conditions and the heating scenario its contribution to the measured $u_\perp$ may be negligible or relevant compared to $v_{E\times B}$. Generally, numerical simulations with linear and nonlinear turbulence codes show phase velocities of the order of a few hundred m/s. The plasma edge is expected to be dominated by electron drift wave turbulence with a phase velocity comparable or smaller than the electron diamagnetic drift velocity [87]. The core region is dominated by ITG, TEM and/or ETG turbulence. Here, the numerical simulations usually give $v_{turb} \sim Fc_s\rho_s/R$ (equation 6.2) with factor F ranging between 0 and 5 [86], which typically corresponds to phase velocities of a few hundred m/s to about 1 km/s. However, there are also indications that in the core region very high turbulence velocities may be possible, e.g. corresponding to ETG turbulence [78]. In cases where v_{turb} is negligible compared to the $E\times B$ velocity $u_\perp$ approximately equals $v_{E\times B}$. If however v_{turb} is non-negligible, then $u_\perp$ and $v_{E\times B}$ differ consequently. A contribution of v_{turb} to the measured $u_\perp$ cannot be identified as such by the Doppler measurement alone, if the turbulence dispersion relation is linear. Hence, a contribution of a non-negligible turbulence phase velocity remains undetectable during a $k_\perp$ scan unless the dispersion relation is nonlinear. Then, its influence on the measured perpendicular velocity would be revealed by a change in magnitude of $u_\perp$ when scanning the probed turbulence wavenumber.

vii) $E\times B$ velocity components
The $E\times B$ velocity is composed of different velocity terms (equation 6.1), which can be derived from experimental measurements and theoretical calculations. The toroidal impurity C^{6+} fluid velocity is provided by the CXRS diagnostic, which measures the velocity profiles close to the tokamak low field side midplane and hence at approximately the same position as the Doppler diagnostic. Note that the $E\times B$ velocity is independent of the species (e.g. ions, electrons, impurity ions) and is hence determined for the plasma impurity C^{6+}, i.e. all velocity components of $v_{E\times B}$

are evaluated for C^{6+}. The poloidal C^{6+} fluid velocity is obtained from neoclassical calculations. However the derived velocity values should be regarded as an estimate, since a disagreement between experimental poloidal velocities and neoclassical calculations has been found in other tokamaks, reporting a discrepancy of one order of magnitude [89, 90]. The diamagnetic velocity can be calculated from experimental data. Naturally, the correctness of the $E \times B$ velocity depends on the reliability of its individual components. While the toroidal and the diamagnetic velocity terms have the usual specific experimental measurement errors, the neoclassical estimate could likely cause a significant error in $v_{E\times B}$ computed from the force balance equation, such that even for negligible turbulence phase velocity a comparison of $u_\perp$ with the calculated $v_{E\times B}$ would show a disagreement.

viii) Plasma conditions
The reliable reproducibility of the discharges corresponding to a tilt angle scan, i.e. discharge series, is a prerequisite for the correct interpretation of the results. While a good discharge reproducibility is assured for the first discharge series problematic machine operating conditions during the second discharge series resulted in a rather unreliable discharge reproducibility with changing impurity contents (the second series was divided unintentionally into three separate discharge blocks - see section 5.3). Depending on the (high) impurity content of the plasma the turbulence behavior could change significantly. Hence, from block to block drastically changing plasma conditions may have occurred, but presumably not during a discharge block. Consequently, in chapter 6 the three sets of discharges are studied separately.

The question is whether the mentioned effects could be significant and affect the measured $u_\perp$ profiles and/or the $k_\perp$ spectra or whether they could explain the observations. This will be discussed in the following two sections separately for the velocity profiles and the turbulence spectra.

8.1 $u_\perp$ measurements

First discharge series
With the new W-band reflectometer channel operated with a stepped launch frequency, radial $u_\perp$ profiles are obtained, which show a dependence on the turbulence wavenumber (e.g. figure 6.4). The variation of the measured $u_\perp$ with probed $k_\perp$ is found consistently for different time point in the H-mode and L-mode phases of the discharge sequence. The perpendicular rotation velocity decreases with increasing turbulence wavenumber (figure 6.6) which is equivalent to a deviation of the corresponding Doppler shifts from an expected linear trend.
Many measurements at low $k_\perp$ from the V-band system and other fusion devices normally give $u_\perp$ values close to the expected $E \times B$ velocity, which in turn is typically deduced from CXRS measurements [31, 68, 75, 56]. Therefore, the observed variation of $u_\perp$ with $k_\perp$ requires some discussion. Simple explanations for the anomalous behavior, like malfunction of the steerable antenna (no change of the

tilt angle) or drastically changing plasma conditions can be ruled out by counter evidence given respectively by the appearance of the raw data and the CXRS toroidal rotation measurements during the full discharge sequence. Higher Bragg order signals also do not appear to be a plausible explanation, although they would cause a similar anomalous appearance of the data in figure 6.5, i.e. in a plot of f_D versus $k_\perp$, since the measured Doppler shift would be misattributed to k instead of $\frac{1}{2}k$. However, higher order signals would leave the $u_\perp$ profiles unaffected and can thus not explain the observed $u_\perp$ variation. For the probed radial region there have been no second or higher order signals identified. Also, a possibly misinterpreted antenna side lobe signal is unlikely to be the cause for the observed continuous decrease of $u_\perp$ with increasing $k_\perp$. A condition for misinterpreting a side lobe signal as main lobe signal is a very poor main lobe Doppler peak merging into the background of the frequency spectrum such that it becomes indiscernible or the complete loss of the main lobe Doppler peak due to too low turbulence levels not exceeding the turbulence amplitude threshold for Doppler measurements. Certainly for L-mode core data this situation is unlikely. Even if this condition would be met, the misinterpretation would be revealed when examining the full set of $u_\perp$ profiles: As long as the main lobe signal is detectable the calculated $u_\perp$ would be the same for the various probed $k_\perp$. If the main lobe is lost and the side lobe is evaluated instead, then the calculated $u_\perp$ would jump to a significantly different value. Then, as long as the side lobe signal is evaluated the calculated (wrong) $u_\perp$ would again be roughly the same for the probed $k_\perp$. Thus, the transition from analyzing the main lobe signal to analyzing the side lobe signal should be characterized by a distinct step in the $u_\perp$ profile sequence. This clear step in the $u_\perp$ values is not seen in the core region. In the pedestal region however, where the turbulence level is expected to be low in H-mode and the amplitude threshold may not be reached, a possible misinterpretation may not be definitely excluded, since here the profiles do not clearly show a gradual decrease but a jump, possibly affecting the data corresponding to tilt angles 11.5° and 14.6° (see figure 6.4).

A more likely interpretation of the experimental observations is drawn from a diagnostic feature. The measured turbulence $k_\perp$ spectra show roughly constant fluctuation levels for low wavenumbers followed by a strong roll-off for higher wavenumbers in the accessible spectral range. According to Blanco, the determination of $u_\perp$ will be erroneous when probing wavenumbers in the spectral fall-off region due to the varying diagnostic response in the probed wavenumber region, $k_\perp \pm \Delta k_\perp$, skewing the nominal Doppler shift to lower frequency values (see point i). The full wave simulation results show that this error will increase with increasing $k_\perp$. Depending on the radial measurement position the spectral knee point of the measured wavenumber spectra (indicating the beginning of the fall-off region) is around $7.5\,\mathrm{cm}^{-1} < k_\perp < 10\,\mathrm{cm}^{-1}$. These $k_\perp$ values coincide with the approximate wavenumber value above which the measured Doppler shifts start to deviate from a linear trend, which is $k_\perp \gtrsim 10\,\mathrm{cm}^{-1}$. For H-mode the magnitude of the discrepancy increases with increasing wavenumbers consistent with the simulation results. Hence, the data of figure 6.5 reflect the simulated behavior of the measured frequency shift and the resulting variation of $u_\perp$ with $k_\perp$ could be explained by

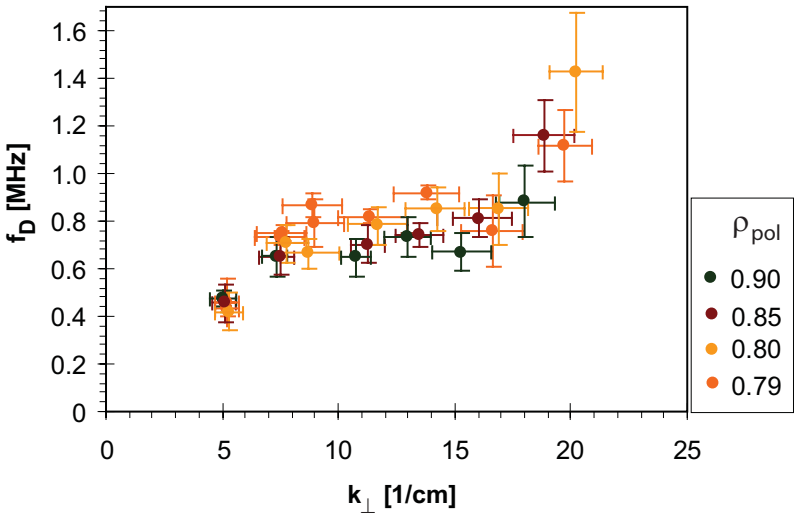

Figure 8.1: Doppler shift frequency versus probed turbulence wavenumber for the 1^{st} series at 4.1 s and 3.6 s (both L-mode).

this diagnostic effect. Therefore, the data suggests that the shape of the underlying $k_\perp$ spectrum is important for the correct measurement of $u_\perp$. As a consequence, the probed turbulence wavenumber should not be significantly higher than the wavenumber corresponding to the spectral knee point. Hence, this wavenumber value would place a limit on the maximum reliable tilt angle that can be used for the $u_\perp$ measurement. This interpretation is remarkably consistent with the experiment regarding the H-mode data. However, it can not explain as clearly the behavior of the L-mode data - see figure 8.1. Although the corresponding wavenumber spectrum is continuously decreasing with $k_\perp$, the measured frequency shift is increasing again at the high turbulence wavenumbers ($k_\perp \gtrsim 15\,\mathrm{cm}^{-1}$), which is not consistent with the simulation results. Another interpretation approach is to attribute the anomalous behavior of the measured perpendicular velocity profiles to the second velocity component of $u_\perp$, the turbulence phase velocity. The consequence of this interpretation would be that in this particular case v_{turb} is contributing significantly to the velocity measured by Doppler reflectometry. Also, v_{turb} would exhibit a nonlinear turbulence dispersion relation. For L-mode the dispersion relation would be found partly nonlinear exhibiting a slightly different behavior than in H-mode. This would support the fact that the turbulence characteristics and the confinement regime are linked. The question whether v_{turb} may be important for low and/or for high turbulence wavenumbers cannot be definitely answered by the Doppler measurements alone. A significance of v_{turb} at low $k_\perp$ is generally supported by numerical simulations [25, 87] and also by experimental measurements [88] reporting nonlinear dispersion relations with a decrease of v_{turb} with increasing $k_\perp$ (figure 8.2 shows a general example of pure TEM and pure ITG turbulence from nonlinear gyrokinetic simulations [98]). Assuming the discrepancy between the various $u_\perp$

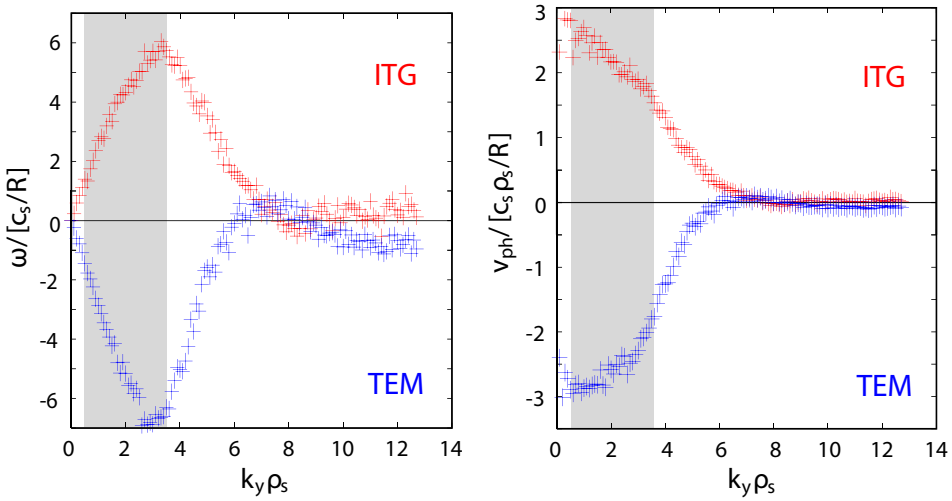

Figure 8.2: General example of frequency and corresponding turbulence phase velocity for pure TEM (blue) and pure ITG (red) turbulence from nonlinear gyrokinetic simulations based on simplified physics (mass ration $m_i/m_e \sim 400$, collisionless, electrostatic, circular flux surfaces) [98]. The grey areas indicate the $k_\perp \rho_s$ region probed by the Doppler diagnostic.

profiles would be indeed due to v_{turb}, then the turbulence inside the plasma $E \times B$ frame would rotate in the ion diamagnetic direction for the probed core region, i.e. inside the pedestal (suggesting ITG dominance) and in the electron diamagnetic direction for the pedestal region (consistent with the expected rotation direction of drift waves), thus reversing direction. However, the observation that the Doppler shifts measured for low turbulence wavenumbers show a linear behavior with $k_\perp$ may indicate that v_{turb} is increasing about linearly with the wavenumber above a value of $k_\perp > 10\,\mathrm{cm}^{-1}$ or equivalently $k_\perp \rho_s > 1.3$ in H-mode, thus suggesting an increasing influence of v_{turb} to the measured velocity for high wavenumbers. In this case, the turbulence in the plasma $E \times B$ frame would move in the electron diamagnetic direction for the core region, whereas in the pedestal region it would move in the ion diamagnetic direction. However, at $k_\perp = 20\,\mathrm{cm}^{-1}$ the turbulence phase velocity would have to reach approximately $2\,\mathrm{km/s} \sim 2v_e^*$. It could also be possible that v_{turb} is significant in the whole probed wavenumber range. There could be different turbulence types present simultaneously in the core region, e.g. ITG dominating at low and TEM at higher $k_\perp$, having opposite rotation directions (see figure 8.2). Under this assumption, $v_{turb,ITG}$ would add to $v_{E\times B}$ at low wavenumbers and $v_{turb,TEM}$ would reduce $u_\perp$ with respect to $v_{E\times B}$ at higher wavenumbers. A transition from probing ITG ($v_{turb,ITG}$) to TEM turbulence ($v_{turb,TEM}$) with increasing $k_\perp$ may possibly explain the observations made in L-mode - figure 8.1.
One approach to identify the circumstances concerning a significant v_{turb} is to calculate the $E \times B$ velocity from the measurements of other diagnostics and theoretical predictions and to compare the result with the measured perpendicular

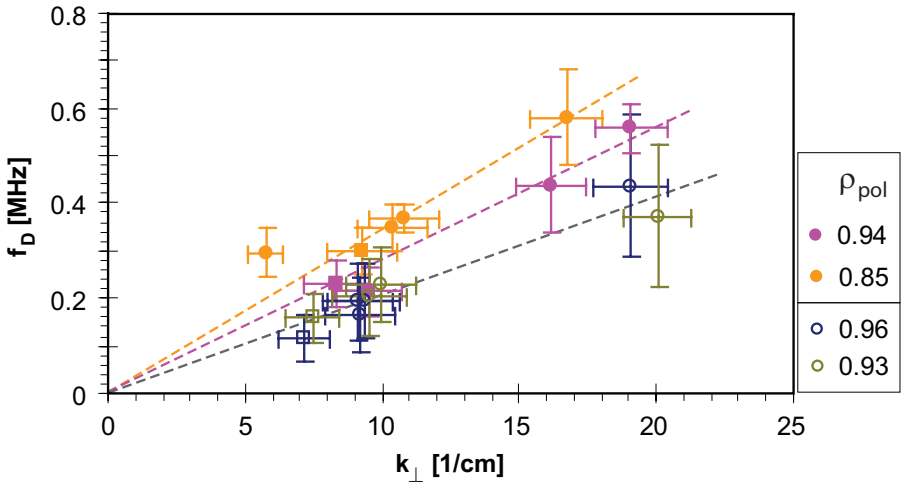

Figure 8.3: Doppler shift frequency versus probed turbulence wavenumber for the 2^{nd} series (open symbols correspond to a shot phase with pure NBI heating and closed symbols to NBI+ECRH). The box symbol denotes data from the V-band system.

velocities. For H-mode the determined $v_{E\times B}$ is presented in figure 6.9 together with the corresponding Doppler $u_\perp$ profiles. The calculated $v_{E\times B}$ significantly exceeds the experimental $u_\perp$ values, thus is closest to the $u_\perp$ profile measured at low $k_\perp$. A similar discrepancy is also observed for the L-mode profiles. The disagreement may suggest that the neoclassical poloidal velocity term is underestimated (i.e. calculated $v_{E\times B}$ is wrong) and/or that the contribution of v_{turb} to $u_\perp$ is not negligible for the probed wavenumbers (i.e. $u_\perp \not\approx v_{E\times B}$) provided that the toroidal velocity measurement by CXRS is reliable. An estimate of the toroidal rotation can be deduced from the (2,1) MHD mode frequency (5.5 kHz) yielding $v_\phi \sim 60$ km/s or $v_\phi B_\theta/B \sim 8.3$ km/s, thus validating the CXRS result. Consequently, the comparison does not yield further clarification, since it is not clear whether the estimated $v_{E\times B}$ is correct.

Basically, two interpretation approaches seem possible - turbulence phase velocity (point vi) and instrumental effect (point i). Unfortunately, a quantitative correction of the data for the described diagnostic feature is not possible, but qualitatively the profiles would shift towards higher $u_\perp$ values when corrected. Since the correction factor should increase with the probed $k_\perp$ [80], the profiles measured for medium and high wavenumbers would possibly come into agreement with the profile obtained for low $k_\perp$ (blue curve in figure 6.9). Then, the difference between the estimated $v_{E\times B}$ and $u_\perp$ would be not severe. The remaining velocity difference could be attributed to the turbulence phase velocity. Also, the rise of f_D at high $k_\perp$ found in L-mode (figure 8.1) could be due to an increase of v_{turb} at these wavenumbers. Thus, a combination of the two effects (point i + point vi) may explain the observations.

Second discharge series

The measured $u_\perp$ profiles show that for this sequence the perpendicular rotation velocity is independent of the probed turbulence wavenumber (e.g. figure 6.3). The W-band profiles measured at (very) different $k_\perp$ all coincide and are also in agreement with the corresponding $u_\perp$ profile measured with the independent V-band Doppler system. This is equivalent to a linear increase of the measured Doppler shift with the probed $k_\perp$ for a particular radial position, as shown in figure 8.3.
The good agreement of the profiles suggests that the intrinsic phase velocity of the turbulence is either negligible compared to the $E \times B$ velocity or a nonzero constant in this range of $k_\perp$. This observation is principally consistent with the general expectations of small turbulence velocities and linear turbulence dispersion relation. A diagnostic effect as described in point i) and the resulting variation of $u_\perp$ with $k_\perp$ is not observed although the spectral roll-off of the underlying turbulence is steep (i.e. high spectral indexes are measured). Despite the good match of the various $u_\perp$ profiles a strong inconsistency with the estimated $E \times B$ velocity is found (figure 6.9 b). The severe disagreement may have several possible reasons. The assumption that the toroidal velocity is substantially over-measured by the CXRS diagnostic does not seem to be supported by the fact that the observed toroidal rotation is in the right order of magnitude for a 2.0 MW NBI heated ASDEX Upgrade plasma. A toroidal rotation (mapped onto the perpendicular plane $v_\phi B_\theta / B$) as low as $\sim 3\,\mathrm{km/s}$ is possible but unlikely under these heating conditions. (Unfortunately, due to the lack of MHD mode activity, an estimate of v_ϕ from the mode frequency is not available for this discharge sequence.) Due to the shallow density and temperature gradients in the core region it can be also assumed that the diamagnetic velocity is small and hence will only weakly influence the result. As a consequence the discrepancy between $u_\perp$ and $v_{E\times B}$ suggests that the contributions of the neoclassical poloidal velocity and/or the turbulence phase velocity may be significantly underestimated by the theoretical predictions. Under the assumption that the neoclassical theory fails in predicting v_θ plus following up on the experimental results by Solomon and Crombe (see point vii) the neoclassical poloidal velocity $v_\theta \approx 0.4\,\mathrm{km/s}$ would increase to $v_\theta \approx 4\,\mathrm{km/s}$ in the core region and the resulting $E \times B$ velocities would indeed be consistent with the measured $u_\perp$. The portion of the turbulence phase velocity to the measured $u_\perp$ remains undetectable, since a possible contribution of a constant v_{turb} (linear turbulence dispersion relation) can not be identified as such by the Doppler measurement. However it is suspicious, that the measured perpendicular rotation of $u_\perp \approx 2\,\mathrm{km/s}$ is rather small for a NBI heated H-mode plasma (for all probed wavenumbers). A diagnostic failure of the W-band channel can be ruled out, since the V-band channel independently measures the same small rotation velocity. As described in section 5.3, the machine conditions were not optimal during the second discharge series (e.g. high impurity content due to air leak). Consequently, the conclusions drawn from the results of this discharge sequence may be valued lower than the results obtained for the first discharge series.

Conclusions
The reliability of the new W-band channel is validated by the very good agreement of the measured $u_\perp$ profiles with the data obtained by the established V-band system irrespective of the plasma conditions when probing a similar turbulence wavenumber range. Comparing the results of the first and the second discharge series shows consistency in some respects but also some significant contrasts. One should bear in mind that the results presented in this thesis come from the very first systematic measurements with the new W-band system. Since currently none of the different interpretation approaches alone could explain all the measured data consistently without contradicting usual expectations, further measurements plus benchmarking of the results with other diagnostics are needed to draw final conclusions.
Nevertheless, the results seems to show that in the probed core region the $u_\perp$ measurement is generally not influenced by higher Bragg order scattering (point ii) or antenna side lobe signals (point iii). There are indications that a significant contribution of the intrinsic phase velocity to the velocity measured by Doppler reflectometry cannot be excluded in general (point vi), although this argument could come into conflict with theoretical small phase velocities predicted for ITG, TEM and drift wave turbulence. A consequence of a non-negligible v_{turb} would be that the determination of the electric field profile from Doppler measurements would be more complicated. In the future, a benchmark with E_r measurements from passive He^+ emission spectroscopy [99] may clarify the impact of v_{turb} on the $u_\perp$ measurement, however just in the SOL and pedestal regions. Also there are strong hints that the shape of the underlying turbulence wavenumber spectrum is crucial for a correct measurement of the perpendicular rotation velocity via Doppler reflectometry (point i). The observed inconsistencies with the current simulation results [80] (second series or L-mode first series) may be due to several effects playing a role, like turbulence phase velocity, nonlinear backscattering effects [97] or complex plasma behavior. Concerning the first series, especially v_{turb} seems to be a candidate for explaining the observations in L-mode, which cannot be explained by the instrumental effect alone. For both discharge series the calculated $E \times B$ velocity exceeds the measured perpendicular velocities in contrast to previous Doppler reflectometry measurements at low $k_\perp$, which usually yielded $u_\perp$ values close to the expected $v_{E\times B}$. This result may hence raise doubts about whether the true poloidal velocity meets the neoclassical estimate or is (substantially) underestimated for these discharge conditions (point vii).

8.2 $k_\perp$ spectra

First discharge series
With the new steerable antenna configuration allowing for dynamic wavenumber selection in the wavenumber range $4 < k_\perp < 25\,\mathrm{cm}^{-1}$ by scanning the tilt angle, turbulence $k_\perp$ spectra are measured with high spatial resolution from $\rho_{pol} = 0.98$ to $\rho_{pol} = 0.78$. The shape of the spectra is similar to previous observations

[57, 93, 92, 91] with a flat part at low wavenumbers and a monotonic decrease for higher wavenumbers above a knee point. The fluctuation levels measured at low $k_\perp$ (flat part) increase towards the edge and are significantly higher in L-mode than in H-mode. The spectral knee point shifts with the radial measurement position and is found around $0.8 \lesssim k_\perp \rho_s \lesssim 1.9$. The rapid decay of the $k_\perp$ spectrum above the knee point is following a power law $S(k_\perp) \sim k_\perp^{-\alpha}$ with spectral index α changing with radius in H-mode.

In previous experiments the position of the knee point in the spectrum is observed at $0.1 \lesssim k_\perp \rho_s \lesssim 1.1$. A value as high as $k_\perp \rho_s \sim 1.1$ is only reported for the deep core region $r/a < 0.5$ by Remkes [92]. Numerical simulations predict the spectral knee point to occur at lower values, typically at $0.1 \lesssim k_\perp \rho_s \lesssim 0.5$. Hence, the measured values shown in figure 7.9 are substantially higher than generally found or expected in the probed radial region, i.e. basically all values (with one exception) equal or exceed the maximum value $k_\perp \rho_s \sim 1.1$ reported in literature. The shift of the knee point with the radial measurement position seems to be correlated with the shift of the data point corresponding to tilt angle setting $-12.4°$. This data point shifts to higher $k_\perp \rho_s$ values with decreasing values, since ρ_s changes with radius while the probed $k_\perp$ remains roughly constant for this fixed tilt angle setting. This correlation may be linked with the observation that the data points measured for the two lowest tilt angle setting ($-2.3°$, $1.8°$) are consistently deviating from the power law, thus forming the flat part of the wavenumber spectrum. Since this deviation is observed to be systematic this may raise doubts about the correctness of the knee point.

Comparing the turbulence amplitudes measured for the tilt angle settings $-12.4°$ and $1.8°$ shows that they often significantly disagree although very similar $k_\perp$ or $k_\perp \rho_s$ values are probed. Whereas the data corresponding to tilt angle $-12.4°$ typically exhibits the turbulence amplitude expected from the fitted power law, the data corresponding to tilt angle $1.8°$ generally exhibits a lower turbulence amplitude. Because of the systematic behavior one may suspect that the low fluctuation levels for tilt angles $-2.3°$ and $1.8°$ could be subject to a diagnostic effect. An instrumental failure due to the specific antenna configuration (see section 4.2.3) could be caused, if the send and receive radiation pattern changed significantly when scanning the tilt angles due to partial screening or deflecting of the send and/or received microwave power by antenna or other vessel components. However, such a failure seems unlikely, since the questionable fluctuation levels are observed for tilt angles that lay in between tilt settings for which reasonable power levels are obtained (e.g. $-12.4°$ and $6.5°$) and there are apparently no interfering hardware components when scanning from $-12.4°$ to $6.5°$ passing the affected tilts $-2.3°$ and $1.8°$. Nevertheless, a repeat of the antenna characterization would be useful (more comprehensive tests) to clarify the circumstances in that respect. Full wave simulations show that higher Bragg order scattering can influence the backscattering efficiency. Less power is received at the $m = -1$ order, if a significant part of the launched microwave power is scattered into higher Bragg orders (point ii). Preliminary simulation results by Lechte obtained by employing simplified plasma geometry (slab, linear density gradient) and turbulence (sinusoidal perturbation),

show qualitatively that this effect can become important for low tilt angles, however only at high fluctuation levels [83]. Unfortunately, this full wave code does not yet account for (multiple) forward scattering processes possibly causing additional power losses, thus degrading the detected backscattered power level. However, the contribution of forward scattering and/or higher order scattering would have to be substantial for shallow tilt angles in order to yield fluctuation levels lining up with the other data points in the spectrum (i.e. also following the power law) when applying a correction for these effects.

At this early stage of investigations with the new Doppler system, diagnostic effects influencing the measurement cannot be ruled out. However, the mentioned effects may possibly alter the spectrum, but not necessarily the fact that a flat part exists at low $k_\perp$, maybe with a different position of the spectral knee point more consistent with previous observations. Also, the results obtained from examining the flat part of the measured $k_\perp$ spectra (figure 7.8 a) should nevertheless hold, since the potentially affected fluctuation levels should scale roughly likewise for the different radial positions. The observed increase of the turbulence amplitude towards the pedestal (i.e. up to $\rho_{pol} \sim 0.96$) is consistent with previous turbulence measurements. A comparison between L-mode and H-mode shows significantly higher turbulence levels plus a steeper increase for L-mode over the whole probed radial range ($0.78 \lesssim \rho_{pol} \lesssim 0.96$), hence a reduced turbulence level in H-mode. A distinct decrease of the density fluctuation levels across the L-H transition for all probed radial turbulence wavenumbers, $4 \lesssim k_r \lesssim 24.5\,\mathrm{cm}^{-1}$, at a measurement position of $r/a = 0.7 - 0.8$ has been reported from the NSTX tokamak by Kaye [100]. Due to the comparable radial positions these measurements may substantiate the results made on ASDEX Upgrade in the outer core region. In addition to the high fluctuation levels at low $k_\perp \rho_s$, the L-mode $k_\perp$ spectra also show the smallest measured spectral indexes ($\alpha \sim 4$), whereas in H-mode the relatively low fluctuation levels at low $k_\perp \rho_s$ are accompanied by high spectral indexes yielding an overall lower turbulence level as can be seen in figure 8.4. However, the reduction in the high $k_\perp$ turbulence is found to be less significant than the reduction in the low $k_\perp$ turbulence (figure 7.8). Generally, the turbulence amplitude measured at $k_\perp \rho_s = 2.2$ are similar for L- and H-mode opposite to the observations made at small $k_\perp \rho_s$. This indicates that the observed turbulence reduction associated with the transition from L-mode to H-mode occurs predominantly at the low wavenumber turbulence.

The spectral indexes measured during L-mode confinement range between 4.0 and 4.5. These values are consistent with previous turbulence wavenumber spectrum measurements on other tokamak experiments, which typically yielded spectral indexes in the order of 3.0-4.5 for ohmic and L-mode discharges [65, 35, 91, 17, 33]. Due to the good agreement of the measured spectral indexes with the results of these previous studies, the influence of the scattering efficiency variation with the tilt angle (point iv) may be assumed to be small for L-mode discharges. A distinct transition in the spectral index from $\alpha = 3.5$ to $\alpha = 7$ at $k_\perp \rho_s \sim 1.3$ has been reported from the Tore Supra tokamak by Hennequin for L-mode deuterium plasmas [65]. Although the reported α values significantly exceed the ones presented in this thesis (L-mode) the transition point roughly coincides with the observed knee point

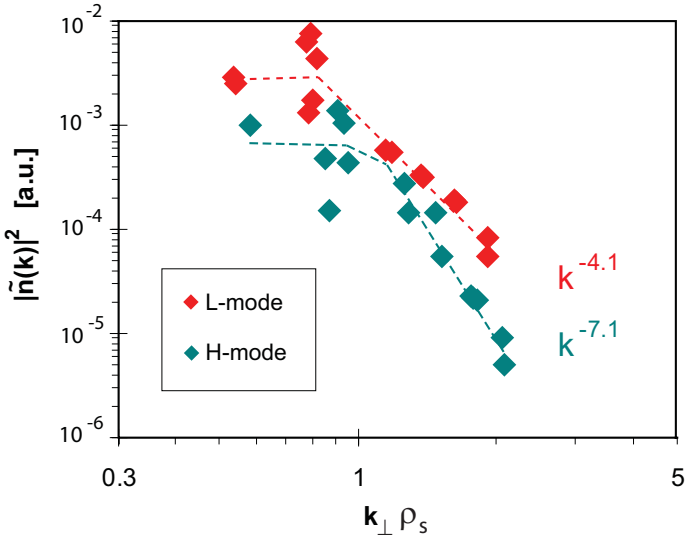

Figure 8.4: Comparison of $k_\perp$ spectra measured during H-mode (1^{st} series at 1.3 s) and L-mode (1^{st} series at 4.1 s) at radial position $\rho_{pol} \sim 0.955$ (inside of pedestal top).

positions. In H-mode the spectra generally fall off very steep with high spectral indexes between $4.4 < \alpha < 9.6$ depending on the radial position and the discharge conditions. The MHD mode activity during the H-mode phase of the discharge (see section 5.3) strongly influenced the plasma conditions, i.e. plasma stored energy and temperature profiles, and thus also the turbulence. The better confinement at time point 1.3 s relative to 2.2 s is reflected in the corresponding turbulence $k_\perp$ spectra, which show a general reduction of the turbulence for time point 1.3 s. The measured spectral indexes for H-mode in general are relatively high compared to those obtained with numerical turbulence codes. The simulations yield density fluctuation $k_\perp$ spectra with typically $\alpha < 4$ in the $k_\perp \rho_s$ region accessible to Doppler reflectometry [101, 86]. However, high spectral indexes up to $\alpha = 7.8$ have already been reported for L-mode plasmas [65, 102, 88] and thus values as high as $\alpha = 7 - 9$ for H-mode may seem possible. Still, the wavenumber spectra are not corrected for the scattering efficiency variation due to the lack of reliable quantitative correction factors for the different tilt angle settings. Qualitatively, a correction for this effect would result in a flattening of the spectra, i.e. a decrease of α. The measured high spectral indexes may hence be regarded as an upper limit.

For L-mode the spectra exhibit a constant α independent of the probed radial position ($0.79 > \rho_{pol} > 0.95$). Comparable L-mode measurements by Remkes probing the full radial region ($0.0 > \rho_{pol} > 0.88$) of the TORTUR tokamak showed a variation of α with radius [92]. But in the radial range $\rho_{pol} > 0.63$ the measured spectral indexes ($\alpha \sim 4.2 - 4.4$) were found to be roughly constant consistent with the L-mode results presented here. Contrarily, in H-mode α changes distinctly in the probed radial range with a consistent linear increase towards the core (figure

7.7). This may indicate that here the scaling properties of the turbulence depend on radius. Since an equivalent measurement in H-mode does presently not exist in the literature, a direct comparison with other experiments cannot be drawn unfortunately.

Second discharge series

A comparison between H-mode turbulence wavenumber spectra measured with different plasma heating scenarios showed that electron heating has an influence on the $k_\perp$ spectra. The spectra measured during the discharge phase with pure NBI heating (2.0 MW) exhibit very similar behavior to the H-mode spectra measured for the first discharge series (also only NBI heated) concerning all examined spectrum characteristics like low $k_\perp$ and high $k_\perp$ fluctuation levels, spectral indexes and spectral knee point. In contrast, the $k_\perp$ spectra measured during the discharge phase with a combination of ECRH (1.0 MW) and NBI heating (2.0 MW) exhibit a distinctly different behavior in many aspects suggesting a change of the turbulence characteristics with the heating scheme.

First we discuss the results obtained for time point 1.8 s (NBI only) having heating conditions comparable to the first discharge series. The fact that the results are very consistent is a good validation of the observed behavior. For this discharge sequence also pedestal $k_\perp$ spectra were presented. In the core region the measured low $k_\perp$ fluctuation level rises towards the edge until it drops significantly in the edge pedestal region consistent with the expectation that in H-mode the turbulence in the pedestal region is strongly reduced. The $k_\perp$ spectra show the expected continuous decrease following power laws with spectral indexes varying with radius between $4.8 < \alpha < 6.6$ at a similar rate as observed for the first discharge series. The spectral index corresponding to the pedestal $k_\perp$ spectrum at $\rho_{pol} = 0.98$ deviates from this linear variation having a smaller value ($\alpha = 2.3$). Figure 7.7 shows that α is smaller in the pedestal region (i.e. the measured spectra are flatter) than in the probed core region. This may indicate that different turbulence forms are dominating in the different plasma regions consistent with the expectations that the turbulence in the plasma pedestal should differ from the turbulence in the core region due to the steep density and temperature pedestal gradients.

Now we focus on the results obtained for time point 3.3 s (ECRH + NBI) having different plasma conditions through electron heating via ECRH. Although there is virtually no change in the electron temperature profile (figure 8.5) despite applying ECRH, several changes appear in the $k_\perp$ spectrum measurement. In the probed radial region the measured spectral indexes also vary linearly with radius but α decreases significantly faster relative to the comparative time point 1.8 s (NBI only). Comparing the $k_\perp$ fluctuation levels shows a decrease in the turbulence at low $k_\perp$ but a significant increase at high $k_\perp$ with radius accompanied by the consequent reduction of α. The "flattening" of the spectra towards the edge is definitely linked to the formation of a pronounced bump in the spectra at $2 \lesssim k_\perp \rho_s \lesssim 2.4$ shifting slightly with the probed radial position. This bump seems to gradually strengthen towards the edge and the observed high $k_\perp$ fluctuation level reaches a large value at $\rho_{pol} = 0.97$ (figure 8.5). Especially this extremely

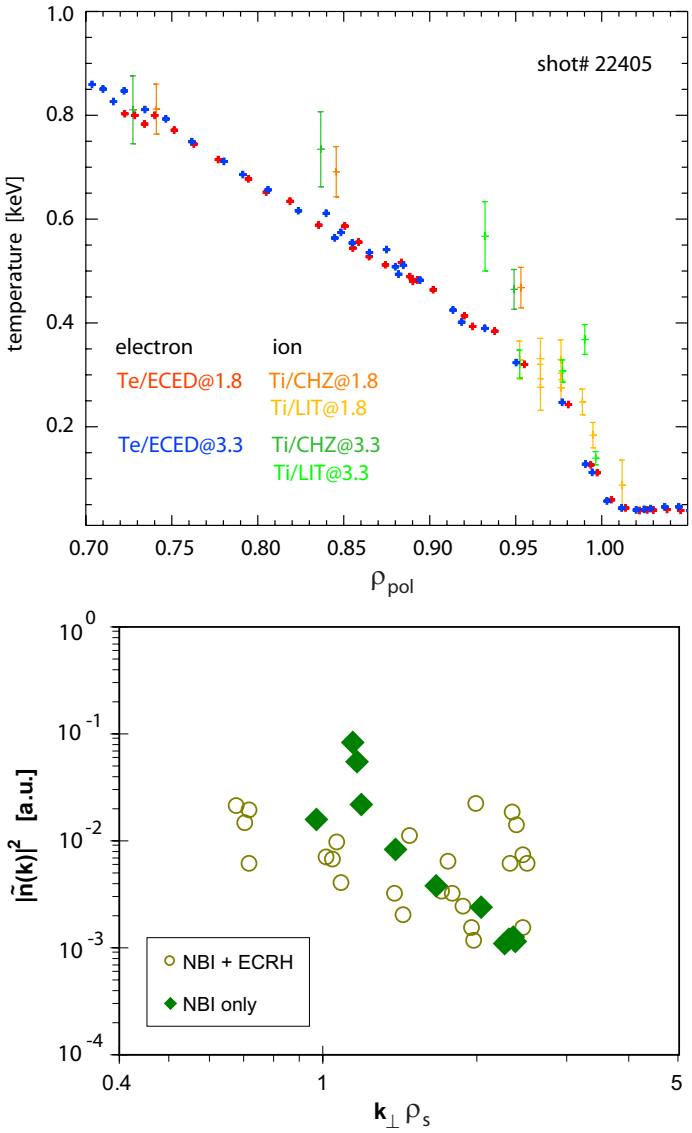

Figure 8.5: Comparison of $k_\perp$ spectra measured for different heating conditions at radial position $\rho_{pol} \sim 0.97$ (pedestal region). 2^{nd} series at 1.8 s (NBI only) and at 3.3 s (NBI + ECRH). The corresponding temperature profiles are also shown.

high fluctuation level at $k_\perp \rho_s = 2.4$ needs to be examined carefully. As mentioned at the beginning of this chapter there exist various potential disturbing factors which could cause distortion in the measured wavenumber spectrum. In general, the strong scatter in the measured pedestal fluctuation levels makes the data interpretation more difficult. The most probable explanation for this large scatter is that the quality of the raw data is degraded by ELM events distorting the measured Doppler signal and thus leading to a variation of up to one order of

magnitude in the detected turbulence amplitude at fixed $k_\perp \rho_s$. Compared to time point 1.8 s the observed ELM frequency at 3.3 s has roughly doubled, hence the raw signal has experienced more distortion and the corresponding $k_\perp$ spectra show an enhanced scatter. However, the observed fluctuation level at $k_\perp \rho_s = 2.4$ is likely due to another effect. It could in principle originate from higher Bragg order scattering at $\frac{1}{2}k$ (point ii). The occurrence of higher order signals requires high turbulence levels at low $k_\perp$.The turbulence amplitude in the low $k_\perp$ range is however significantly decreased relative to the comparative time point (figure 7.8 a). Since, the corresponding $k_\perp$ spectrum seems to be not affected by higher order signals (figure 8.5), their appearance in the considered spectrum seems unlikely. Another diagnostic effect causing the observed anomalous high turbulence level, might be a false Doppler signal originating from an antenna side lobe associated with a significantly smaller $k_\perp$ (point iii). However, this is only likely under the assumption that the "true" level of turbulence at $k_\perp \rho_s = 2.4$ drops substantially (at least below the level measured for the comparative time point) such that the true Doppler signal is lost (turbulence threshold effect). A possible physical interpretation for the bump in the $k_\perp$ spectra is based on previous results by Brower reporting the observation of a large-amplitude, narrow-band modes in the wavenumber spectra of the typical broad-band turbulence measured on the TEXT tokamak [91]. These narrow-band fluctuations appeared in the $k_\perp$ spectra as a distinctly pronounced bump at $5.5 - 7.5\,\mathrm{cm}^{-1}$ depending on the radial measurement position. However, Brower observed these large-amplitude, narrow-band modes to be localized towards the torus high field side. At the plasma edge the $k_\perp$ spectra showed the usual monotonic decrease. A comparison of the results shows that the appearance of the wavenumber spectra (with bump) is very similar, but there are also strong inconsistencies regarding the spectral position of the bump ($5.5 - 7.5\,\mathrm{cm}^{-1}$ versus $14 - 19\,\mathrm{cm}^{-1}$, ρ_s not specified by Brower), the radial localization (torus inside versus torus outside, edge) and plasma conditions (ohmic versus H-mode). Unfortunately, the spectral coverage at $\rho_{pol} = 0.97$ is not sufficient to show the further trend of the $k_\perp$ spectrum to see if the spectral shape substantiates or contradicts this potential interpretation. Gyrokinetic multi-scale ITG/TEM/ETG turbulence simulations by Görler and Jenko show a flattening of the density $k_\perp$ spectra in the wavenumber range accessible with Doppler measurements with a very small spectral index for pure TEM/ETG turbulence [98, 103]. In general, the typical steep decay of the measured $k_\perp$ spectra at high wavenumbers (i.e. large α) suggest no dominant TEM/ETG turbulence. However, the enhanced fluctuation levels at high $k_\perp \rho_s$ in the pedestal region may be possibly explained by an increased ETG contribution. In principle, the amount by which the experimental temperature gradient exceeds the critical gradient increases with increasing ρ_{pol} (figure 8.5). This may imply a higher level of ETG turbulence towards the edge (especially in the pedestal region where ∇T_e is large) due to the potentially stronger ETG drive. However, dedicated linear gyrokinetic simulations using the GENE code [8] with experimental T_e, T_i, n_e profiles (temperature gradients extracted from $0.95 < \rho_{pol} < 0.98$) and realistic tokamak geometry (geometry coefficients extracted from CLISTE equilibrium) show no ETG turbulence activity at the edge of the plasma around $\rho_{pol} = 0.97$ [98].

Recently, similar measurement by Rhodes on DIII-D comparing turbulence levels measured in ohmic plasmas with and without electron cyclotron heating showed also an increase in high k turbulence at $\rho_{pol} = 0.6$ and $\rho_{pol} = 1.0$ when applying ECH [104]. However, the corresponding linear turbulence simulations predicted the contrary behavior, a decrease. The author concluded that this discrepancy might be due to nonlinear or non-local effects. For the measurements presented in this thesis the important stability parameters (i.e. ∇T_e, ∇T_i, T_e/T_i, ∇n_e) show only small variations between the different heating schemes, i.e. with and without ECRH. Also other relevant parameters (i.e. magnetic shear $\hat{s}$, Z_{eff}, plasma shape) stay roughly constant. Thus, it remains arguable, if the enhanced turbulence amplitude at high wavenumbers in the pedestal region could be interpreted as an ETG signature.

Conclusions

Compared to L-mode confinement the measured turbulence wavenumber spectra clearly show a reduction of the turbulence level in H-mode, that occurs predominantly at low $k_\perp \rho_s$ (i.e. reduced large wavelength turbulence). The position of the spectral knee point appears at very high $k_\perp \rho_s$ values, that are not consistent with previous turbulence measurements and numerical turbulence simulation reporting the knee point at significantly lower $k_\perp \rho_s$. The observed flatness of the spectrum in the range $0.6 \lesssim k_\perp \rho_s \lesssim 1.3$ would require unstable modes acting as a source for driving the turbulence in that range. Hence, one can not exclude a diagnostic effect (point iv) causing the low fluctuation levels obtained for low tilt angle setting, which are observed to deviate systematically from the power law decay, especially regarding that the measurement technique and the corresponding diagnostic setup (hardware) are employed just newly for performing this measurements. Concerning the technique - Doppler reflectometry - it is known from full wave simulation studies that the Bragg backscattering efficiency and hence the backscattered power level (interpreted as $S(k_\perp)$) depends nonlinearly on the antenna tilt angle. Currently, complex and computationally expensive full wave studies are in progress to research and quantify this diagnostic effect and its impact on the measurement. Although the progresses made in this field are encouraging [83], there will be no reliable calibration available in the near future, applicable to the data. Nevertheless, the obtained L-mode spectral indexes agree very well with previous measurements performed on other tokamak experiments. The spectral indexes detected in H-mode however show an unexpected behavior, i.e. they are generally very high plus show a variation with radius. This result is obtained consistently for all analyzed H-mode data, thus validating the observations. However, according to numerical turbulence simulations, $\alpha > 4$ in the core region and a dependence on radius is not expected in general. The measurements reveal a change in the shapes of the turbulence $k_\perp$ spectra when applying ECRH in addition to NBI heating suggestive of a change in the turbulence characteristics with the heating scenario. However, the heating conditions seem to have a complicated influence on the underlying turbulence displayed by the unusual appearance of the corresponding spectra. Generally, the fluctuation levels at low $k_\perp \rho_s$ are reduced, while they increase at high $k_\perp \rho_s$ towards the edge accompanied by a substantial flattening of the spectra (i.e. decrease

in α) across the edge region. Diagnostic effects (point ii and iii) do not seem to be plausible explanations for the observations in the high wavenumber region. A potential interpretation is drawn upon an enhanced ETG turbulence level becoming noticeable at high $k_\perp \rho_s$, i.e. giving raise to the anomalously high fluctuation levels. Clearly, more dedicated measurements and (nonlinear) simulations are needed to examine if these high fluctuation amplitudes are indeed a sign of ETG turbulence.

Chapter 9

Summary and outlook

Plasma turbulence is believed to be the main cause of the anomalous high radial transport recorded in tokamaks. For this reason the study of plasma turbulence is an important part of present fusion plasma research. Measurements of the turbulence properties (i.e. amplitude, frequency and wavenumber spectra) are required to gain better understanding of the turbulence behavior. Although a turbulent plasma has fluctuations in all its main parameters (i.e. density $\tilde{n}$, temperature $\tilde{T}$, potential $\tilde{\Phi}$ and magnetic field $\tilde{B}$) contributing to the anomalous transport, the most important fluctuations are density fluctuations, since $\tilde{n}$ is orders of magnitudes larger than the other types of fluctuations.
A diagnostic technique that is sensitive to density fluctuations at a specific turbulence wavenumber is microwave Doppler reflectometry, a powerful radar technique based on the localized Bragg backscattering of microwaves by the density turbulence at the plasma cutoff layer. The local perpendicular plasma rotation velocity, $u_\perp = v_{E\times B} + v_{turb}$, corresponding to the velocity perpendicular to B of the density fluctuations moving with the bulk plasma is obtained from the received Doppler signal. The backscattered power is indicative of the turbulence amplitude and the probed turbulence wavenumber $k_\perp$ is determined by the incident angle θ of the beam via the Bragg condition $k_\perp \sim 2k_0 sin\theta$. Hence, scanning the antenna tilt angle yields a localized measurement of the turbulence $k_\perp$ spectrum, which provides valuable information on the turbulence behavior under varying plasma conditions.
In order to be able to vary the antenna tilt angle the existing V-band Doppler reflectometry system ($50 - 75\,\mathrm{GHz}$) of the ASDEX Upgrade tokamak has been upgraded with the addition of a new channel especially suited for the $k_\perp$ spectrum measurement. The new diagnostic system is composed of a new steerable antenna with a variable line of sight and a new W-band reflectometer ($75 - 110\,\mathrm{GHz}$) employing a 'phase locked loop' stabilized transmitter source, which provides the essential precise determination of the instrument frequency response. In addition, the higher probing microwave frequencies allow for a wider radial measurement range by penetrating deeper into the core region of the plasma. The development and implementation of the reflectometer hardware plus the commissioning of the new channel were important parts of this thesis project. The functionality of the new diagnostic system was clearly validated by comprehensive laboratory tests and

successful benchmarking against the existing V-band Doppler system during plasma operation, which consistently yielded excellent agreement in results.

This thesis work presents a survey of experimental radial $u_\perp$ profile and turbulence $k_\perp$ spectrum measurements obtained with the new W-band Doppler channel for a variety of plasma scenarios. The new antenna configuration allows for measuring $u_\perp$ profiles at different turbulence wavenumbers ranging from 4 to $25\,\mathrm{cm}^{-1}$. Two dedicated discharge series (tilt scans) were performed yielding similarities and contrasts with respect to the $u_\perp$ measurement. The measurements of the first discharge series, which was dedicated to the comparison of low and high confinement regime (L- and H-mode), show a dependence of $u_\perp$ on the probed $k_\perp$, i.e. a decrease of $u_\perp$ with increasing $k_\perp$. In contrast, the measurements of the second discharge series, which was dedicated to the comparison of different heating schemes, show little dependence of $u_\perp$ on the probed turbulence wavenumber. Various attempts to reconcile these results were presented, however none of the different factors could individually explain the complete set of measurements in a consistent way. Nevertheless, the results suggest that the contribution of the intrinsic phase velocity of the turbulence to the measured perpendicular velocity may in some cases not be negligible. There are also strong indications that the shape of the underlying turbulence wavenumber spectrum is a significant factor in the velocity measurement via Doppler reflectometry. The measurements of the first discharge series support recent full wave simulation results showing a relationship between the $k_\perp$ spectrum and a reliable measurement of $u_\perp$. At first view the results of the second discharge series may seem inconsistent with this interpretation, but this inconsistency may be explained by additional effects playing a significant role masking the predicted behavior (e.g. finite turbulence phase velocity, nonlinear backscattering effects or unstable plasma conditions). For both discharge series a disagreement between the measured perpendicular velocities and an estimate of the $E \times B$ velocity is found. Contrary to previous measurements the estimated $v_{E\times B}$ exceeds (substantially) the measured $u_\perp$, which may be indicative of a potential underestimation of the poloidal fluid velocity component of $v_{E\times B}$ by the neoclassical theory in these discharge conditions.

Scanning the antenna tilt angle allows for measuring the turbulence $k_\perp$ spectrum covering the spectral range $0.5 \lesssim k_\perp \rho_s \lesssim 3.5$, where ρ_s is the ion gyro radius evaluated with the electron temperature. Further, the high spatial resolution of Doppler reflectometry permits a localized measurement of the spectra - typically $\Delta\rho_{pol} \pm 0.015$ (ρ_{pol} is the normalized radius). The probed radial range was $0.78 > \rho_{pol} > 0.98$, thus covering the pedestal region inside the separatrix and part of the core plasma. The measured $k_\perp$ spectra show a reduction of the turbulence level with the transition from L-mode to H-mode confinement with a predominant decrease of the low $k_\perp$ turbulence. Generally, the spectra exhibit a monotonic decay at medium and high probed wavenumbers according to a power law $k_\perp^{-\alpha}$ with spectral index α, which is generic for turbulence wavenumber spectra. The spectral indexes measured for L-mode plasmas ($\alpha \sim 4$) agree very well with previous results reported from other tokamak experiments. While in L-mode α is found to be constant in the probed radial region, the spectral index increases towards the core

for H-mode plasmas reaching comparatively high values ($\alpha \sim 6 - 9$) suggesting a change in the character of the turbulence with radius. Regarding the $k_\perp$ spectrum measurement, the two different discharge sequences yield consistent results, provided that the heating scenario is similar, i.e. pure neutral beam (NBI) heating is applied. Applying localized additional electron heating via ECRH results in a change of the turbulence $k_\perp$ spectra, which is probably linked with changing properties of the underlying turbulence. The shape of the corresponding spectra suggests that the influence of the altered heating conditions on the turbulence is complex. Towards the plasma edge the turbulence level at low $k_\perp \rho_s$ reduces, while it increases at high $k_\perp \rho_s$, i.e. α decreases substantially with radius. The extremely high fluctuation levels observed at high $k_\perp \rho_s \sim 2.4$ in the pedestal region might be interpreted as evidence of an ETG (electron temperature gradient) turbulence signature, but clearly more dedicated investigations are required to substantiate this interpretation.

The presented results come from the very first systematic investigations using the new W-band channel exploring the extended diagnostic capabilities of the ASDEX Upgrade Doppler reflectometry system. Further detailed studies and benchmarking of the results against other diagnostics are required in order to gain more insight into the plasma conditions and turbulent processes and to learn more about the diagnostic response. This requires much more work and will hence be the subject of follow-up projects. Nevertheless, the presented measurements provide important baseline results with new findings especially in the area of turbulence $k_\perp$ spectrum studies in H-mode thereby contributing to fill this gap in plasma turbulence research. Overall, this thesis work has generated a database of new results motivating a continuance of studies in this research area.

In order to substantially enhance the measurement efficiency of the diagnostic an important hardware upgrade would be a remote controlled antenna steering mechanism using a stepper motor. This would allow for varying the tilt angle during individual discharges hence providing a complete $k_\perp$ spectrum in a single discharge. This in turn eliminates the discharge reproducibly as an error source and the amount of data points in the spectrum could be greatly increased yielding a high-resolved spectrum. A further hardware upgrade would be a revised antenna design specifically optimized for the W-band frequency range and X-mode polarization (in contrast to the current broad-band, multi polarization concept, i.e. V- and W-band and O- and X-mode) in order to enhance the spectral resolution of the diagnostic and thus improve the measurement. With these antenna upgrades the new system should be perfectly suited for detailed turbulence studies. The initial results on the influence of ECRH and other heating scenarios on the turbulence are very promising and a continuation here is expected to yield important results. Particularly, further controlled attempts to destabilize ETG modes should be made to examine their impact on the measured $k_\perp$ spectrum at scales ($k_\perp \rho_s \gtrsim 2$) accessible to Doppler measurements. Also, further measurements to investigate the turbulence behavior in H-mode with a focus on spatial variations are highly desirable. Due to its high spatial resolution, Doppler reflectometry is particularly suitable for this kind of investigation.

Bibliography

[1] OECD/International-Energy-Agency, *World Energy Outlook 2006*.

[2] JET Team, *Fusion energy production from a deuterium-tritium plasma in the JET tokamak*, Nuclear Fusion **32**, 187 (1992).

[3] J. Strachan et al., *Fusion power production from TFTR plasmas fueled with deuterium and tritium*, Physical Review Letters **72**, 3526 (1994).

[4] M. Van Dyke, *An Album of Fluid Motion*, Parabolic Press, 1982.

[5] B. Scott, *Lecture Notes in Physics, LNP670*, chapter 8: *Introduction to Turbulence in Magnetised Plasmas*, pages 173–212, Springer Berlin, 2007.

[6] M. Beer, *Gyrofluid models of turbulent transport in tokamaks*, PhD thesis, Princeton University, 1995.

[7] J. Connor and H. Wilson, *Survey of theories of anomalous transport*, Plasma Physics and Controlled Fusion **36**, 719 (1994).

[8] F. Jenko et al., *Electron temperature gradient driven turbulence*, Physics of Plasmas **7**, 1904 (2000).

[9] F. Jenko et al., *Prediction of Significant Tokamak Turbulence at Electron Gyroradius Scales*, Physical Review Letters **89**, 225001 (2002).

[10] T. Dannert et al., *Gyrokinetic simulation of collisionless trapped-electron mode turbulence*, Physics of Plasmas **12**, 072309 (2005).

[11] T. Dannert, *Gyrokinetische Simulation von Plasmaturbulenz mit gefangenen Teilchen und elektromagnetischen Effekten*, PhD thesis, TU München, 2005.

[12] B. Scott, *Computation of electromagnetic turbulence and anomalous transport mechanisms in tokamak plasmas*, Plasma Physics and Controlled Fusion **45**, A385 (2003).

[13] F. Chen, *Introduction to plasma physics and contolled fusion*, Plenum Press, New York, second edition, 1984.

[14] X. Garbet et al., *Physics of transport in tokamaks*, Plasma Physics and Controlled Fusion **46**, B557 (2004).

[15] H. Zohm, Vorlesungsskript Plasmaphysik I, LMU München, WS 2001-2002.

[16] H. Weisen et al., *Turbulent density fluctuations in the TCA Tokamak*, Plasma Physics and Controlled Fusion **30**, 293 (1988).

[17] P. Devynck et al., *Localized measurements of turbulence in the TORE SUPRA tokamak*, Plasma Physics and Controlled Fusion **35**, 63 (1993).

[18] E. Mazzucato et al., *Turbulent fluctuations in TFTR configurations with reversed magnetic shear*, Physical Review Letters **77**, 3145 (1996).

[19] C. Rettig et al., *Microturbulence reduction during negative central shear tokamak discharges*, Physics of Plasmas **4**, 4009 (1997).

[20] G. D. Conway et al., *Suppression of Plasma Turbulence During Optimized Shear Configurations in JET*, Physical Review Letters **84**, 1463 (2000).

[21] G. D. Conway et al., *Turbulence reduction in internal transport barriers on ASDEX Upgrade*, Plasma Physics and Controlled Fusion **43**, 1239 (2001).

[22] P. Diamond et al., *Zonal flows in plasma - a review*, Plasma Physics and Controlled Fusion **47**, R35 (2005).

[23] F. Jenko et al., *Critical gradient formula for toroidal electron temperature gradient modes*, Physics of Plasmas **8**, 4096 (2001).

[24] F. Ryter et al., *Experimental Evidence for Gradient Length-Driven Electron Transport in Tokama*, Physical Review Letters **87**, 2325 (2001).

[25] F. Merz and F. Jenko, *Nonlinear Saturation of Trapped Electron Modes via Perpendicular Particle Diffusion*, Physical Review Letters **100**, 035005 (2008).

[26] K. Burrell, *Effects of ExB velocity shear and magnetic shear on turbulence and transport in magnetic confinement devices*, Physics of Plasmas **4**, 1499 (1997).

[27] X. Garbet, *Introduction to turbulent transport in fusion plasmas*, C.R. Physique **7**, 573 (2006).

[28] J. Wesson, *Tokamaks*, Clarendon press - Oxford, third edition, 2004.

[29] I. Hutchinson, *Principles of plasma diagnostics*, Cambridge University Press, 1987.

[30] E. Mazzucato et al., *Microwave reflectometry for magnetically confined plasmas*, Review of Scientific Instruments **69**(6), 2201 (1998).

[31] G. D. Conway et al., *Plasma rotation profile measurements using Doppler reflectometry*, Plasma Physics and Controlled Fusion **46**, 951–970 (2004).

[32] R. Durst et al., *Density fluctuation measurements via beam emission spectroscopy*, Review of Scientific Instruments **63**, 4907 (1992).

[33] C. Ritz et al., *Characterization of tokamak edge turbulence by far-infrared laser scattering and Langmuir probes*, Nuclear Fusion **27**, 1125 (1987).

[34] D. Brower et al., *The spectrum, spatial distribution and scaling of microturbulence in the TEXT tokamak*, Nuclear Fusion **27**, 2055 (1987).

[35] P. Hennequin et al., *Fluctuation spectra and velocity profile from Doppler backscattering on Tore Supra*, Nuclear Fusion **46**, S771 (2006).

[36] The ASDEX Upgrade Team, *Special issue on ASDEX Upgrade*, Fusion Science and Technology **44**(3), 569–592 (2003).

[37] R. Aymar et al., *Overview of ITER-FEAT – The future international burning plasma experiment*, Nuclear Fusion **41**, 1301 (2001).

[38] G. Federici et al., *Key ITER plasma edge and plasma-material interaction issues*, Journal of Nuclear Materials **313-316**, 11–22 (2003).

[39] R. Neu et al., *Final steps to an all tungsten divertor tokamak*, Journal of Nuclear Materials **363-365**, 52–59 (2007).

[40] R. Neu et al., *Operational conditions in a W-clad tokamak*, Journal of Nuclear Materials **367-370**(2), 1497–1502 (2007).

[41] J.-M. Noterdaeme et al., *The ASDEX Upgrade ICRH Experiment*, Europhys. Conf. Abstr. , page 61 (1992).

[42] F. Braun et al., *ICRF system enhancements at ASDEX Upgrade*, Fusion Engineering and Design **56**, 551 (2001).

[43] F. Leuterer et al., *The ECRH system of ASDEX Upgrade*, Fusion Engineering and Design **56-57**, 615 (2001).

[44] A. Stäbler et al., *Performance of the first ASDEX Upgrade neutral beam injector*, Proc. 18th Symp. Fusion Technology, Karlsruhe, Germany , page 593 (1995).

[45] O. Vollmer et al., *Commissioning and performance of the new ASDEX Upgrade neutral beam injector*, Proc. 20th Symp. Fusion Technology, Marseille, France , page 449 (1999).

[46] Weblink, http://www.aug.ipp.mpg.de/cgibin/local_or_pass/diags_description ?diag=DCN.

[47] H. Murmann et al., *The Thomson scattering systems of the ASDEX Upgrade tokamak*, Review of Scientific Instruments **63**, 4941 (1992).

[48] J. Schweinzer et al., *Reconstruction of plasma edge density profiles from Li I (2s-2p) emission profiles*, Plasma Physics and Controlled Fusion **34**, 1173 (1992).

[49] A. Silva et al., *Ultrafast broadband frequency modulation of a continuous wave reflectometry system to measure density profiles on ASDEX Upgrade*, Review of Scientific Instruments **67**, 4138 (1996).

[50] H. Meister et al., *Measurement of poloidal flow, radial electric field and ExB shearing rates at ASDEX Upgrade*, Nuclear Fusion **41**, 1633 (2001).

[51] Weblink, http://www.aug.ipp.mpg.de/aug/local/diagnostik4/ece/ecediags.html.

[52] F. Wagner et al., *Regime of improved confinement and high beta in neutral-beam-heated divertor discharges of the ASDEX tokamak*, Physical Review Letters **49**(19), 1408 (1982).

[53] W. Suttrop, *Physics of edge operational limits and their effect on tokamak confinement*, Habilitationsschrift, IPP Garching, 2000.

[54] W. Suttrop, *The physics of large and small edge localized modes*, Plasma Physics and Controlled Fusion **42**(5A), A1–A14 (2000).

[55] H. Zohm, *Edge Localized Modes (ELMs)*, Plasma Physics and Controlled Fusion **38**(2), 105 (1996).

[56] M. Hirsch et al., *Doppler reflectometry for the investigation of propagating density perturbations*, Plasma Physics and Controlled Fusion **43**, 1641 (2001).

[57] P. Liewer et al., *Measurements of microturbulence in tokamaks and comparisons with theories of turbulence and anomalous transport*, Nuclear Fusion **25**, 543 (1985).

[58] Data provided by G.D. Conway, Max-Planck-Institut für Plasma Physik.

[59] E. Poli et al., *TORBEAM, a beam tracing code for electron-cyclotron waves in tokamak plasmas*, Computer Physics Communications **136**, 90 (2001).

[60] V. Ginzburg, *Propagation of electromagnetic waves in plasma*, NY: G&B, 1961.

[61] G. D. Conway et al., *Observations on core turbulence transitions in ASDEX Upgrade using Doppler reflectometry*, Nuclear Fusion **46**, S799 (2006).

[62] G. D. Conway et al., *Direct measurement of zonal flows and geodesic acoustic mode oscillations in ASDEX Upgrade using Doppler reflectometry*, Plasma Physics and Controlled Fusion **47**, 1165 (2005).

[63] J. Schirmer et al., *Radial correlation length measurements on ASDEX Upgrade using correlation Doppler reflectometry*, Plasma Physics and Controlled Fusion **49**, 1019 (2007).

[64] J. Schirmer et al., *The radial electric field and its associated shear in the ASDEX Upgrade tokamak*, Nuclear Fusion **46**, S780 (2006).

[65] P. Hennequin et al., *Scaling laws of density fluctuations ar high-k on Tore Supra*, Plasma Physics and Controlled Fusion **46**, B121 (2004).

[66] Analog Devices, *RF PLL Frequency Synthesizers (ADF4110/ ADF4111/ ADF4112/ ADF4113)*, 2004, data sheet Rev. C.

[67] M. Curtin and P. O'Brien, *Phase-Locked Loops for High-Frequency Receivers and Transmitters - Part 1-3*, Technical report, Analog Devices, 1999.

[68] S. Klenge, *Dynamik magnetisch eingeschlossener Plasmen am L-H Übergang*, PhD thesis, Universität Stuttgart, 2005.

[69] O. Boyle, R. McLaren, and E. van der Bij, *The S-LINK Interface Specification*, Technical report, CERN, 1997, http://www.cern.ch/HSI/s-link/.

[70] W. Suttrop et al., *Fast economical data acquisition systems based on the CERN S-LINK interface standard*, Fusion Engineering and Design **60**, 297 (2002).

[71] D. Huffmann, *A methode for the construction of minimum-redundancy codes*, Proceedings of the Institute of Radio Engineers **40**, 1098 (1952).

[72] K. Behler et al., *Review of the ASDEX Upgrade data acquisition environment - present operation and future requirements*, Fusion Engineering and Design **43**, 247 (1999).

[73] Weblink, http://www.mdsplus.org.

[74] F. Monaco, Max-Planck-Institut für Plasma Physik Garching, private communications, 2007.

[75] J. Schirmer, *Plasma Turbulence Studies Using Correlation Doppler Reflectometry on the ASDEX Upgrade Tokamak*, PhD thesis, LMU München, 2005.

[76] T. Stix, *Waves in plasmas*, Springer, 1992.

[77] R. White and F. Chen, *Amplification and absorption of electromagnetic waves in overdense plasmas*, Plasma Physics **16**, 565 (1973).

[78] G. D. Conway et al., *Doppler reflectometry on ASDEX Upgrade: Foundations and latest results*, page 30, Proc. 8th International Reflectometry Workshop (St. Petersburg), May 2007.

[79] C. Lechte et al., *Full wave Doppler reflectometry simulations in 2D*, page 67, Proc. 8th International Reflectometry Workshop (St. Petersburg), May 2007.

[80] E. Blanco et al., *Doppler reflectometry studies using a two-dimensional full-wave code*, Plasma Physics and Controlled Fusion **48**, 699 (2006).

[81] F. da Silva et al., *Global full-wave simulation of the Tore-Supra Doppler reflectometer*, Review of Scientific Instruments **75**, 3810 (2004).

[82] C. Lechte, Institut für Plasmaforschung Stuttgart, private communications, 2008.

[83] C. Lechte, *Fusion oriented plasma physics, Doppler reflectometry simulations*, annual report IPF Stuttgart, 2007.

[84] P. McCarthy, *Analytical solutions to the Grad-Shafranov equation for tokamak equilibrium with dissimilar source functions*, Physics of Plasmas **6**, 3554 (1999).

[85] A. Peeters, *Analytical solutions to the Grad-Shafranov equation for tokamak equilibrium with dissimilar source function*, Physics of Plasmas **7**, 268 (2000).

[86] F. Jenko, Max-Planck-Institut für Plasma Physik Garching, private communications, 2007.

[87] B. Scott, *Low frequency fluid drift turbulence in magnetised plasmas*, Report IPP 5/92 (2001), Max-Planck-Institut für Plasmaphysik, Garching.

[88] D. Brower et al., *Multichannel scattering studies of the spectra and spatial distribution of tokamak microturbulence*, Physical Review Letters **54**, 689 (1985).

[89] W. Solomon et al., *Experimental test of neoclassical theory of poloidal rotation in tokamaks*, pages CN–116/EX/P4–10, Vilamoura, Portugal, November 2004, 20th IAEA Fusion Energy Conference.

[90] K. Crombé et al., *Poloidal rotation dynamics, radial electric fields, and neoclassical theory in the Jet internal-transport-barrier region*, Physical Review Letters **95**, 155003 (2005).

[91] D. Brower et al., *Observations of large-amplitude, narrow-band density fluctuations in the interior region of an ohmic tokamak plasma*, Physical Review Letters **55**, 2579 (1985).

[92] G. Remkes et al., *Density fluctuations in the TORTUR tokamak*, Plasma Physics and Controlled Fusion **34**, 1379 (1992).

[93] E. Mazzucato et al., *Spectrum of small-scale density fluctuations in tokamaks*, Physical Review Letters **48**, 1828 (1982).

[94] G. D. Conway et al., *Effects of reflectometer asymmetries on fluctuation measurements*, Plasma Physics and Controlled Fusion **41**, 65 (1999).

[95] Y. Lin et al., *Plasma curvature effects on microwave reflectometry fluctuation measurements*, Plasma Physics and Controlled Fusion **43**, L1–8 (2001).

[96] V. Bulanin et al., *Broadening of scattering spectra in reflectometry experiment*, pages 27A, P–2.55, St. Petersburg, Russia, July 2003, 30th EPS Conference on Controlled Fusion and Plasma Physics.

[97] F. da Silva et al., *Evaluation of the forward scattering contribution to the Doppler signal using a FDTD code*, Proc. 8th International Reflectometry Workshop (St. Petersburg), May 2007.

[98] T. Görler, Max-Planck-Institut für Plasma Physik Garching, private communications, 2008.

[99] B. Langer, *Bestimmung des radialen elektrischen Feldes am Plasmarand durch linienintegrierte Messungen an He^+*, Diploma Thesis, TU München, October 2007.

[100] S. Kaye et al., *Confinement and local transport in the National Spherical Torus Experiment (NSTX)*, Nuclear Fusion **47**, 499 (2007).

[101] R. Waltz et al., *Coupled ion temperature gradient and trapped electron mode to electron temperature gradient mode gyrokinetic simulations*, Physics of Plasmas **14**, 056116 (2007).

[102] C. Honor et al., *Small scale density fluctuations in Tore Supra: rupture in the scaling law*, pages B103PR, 0647, Praha, Czech Republic, June/July 1998, 25th EPS Conference on Controlled Fusion and Plasma Physics.

[103] T. Görler and F. Jenko, *Scale separation between electron and ion thermal transportt*, preprint (to be submitted to Physical Review Letters), March 2008.

[104] T. Rhodes et al., *Broad wavenumber turbulence and transport during ohmic and electron cyclotron heating in the DIII-D tokamak*, Plasma Physics and Controlled Fusion **49**, B183 (2007).